Investigation on the integrated approach to design and ultraprecision machining of freeform surfaced optics and its implementation perspectives

A thesis submitted for the degree of Doctor of Philosophy

by

Shangkuan Liu

Department of Mechanical and Aerospace Engineering

Brunel University London

June 2025

Abstract

Over the last two decades or so, high precision freeform surfaced components and devices have been drawing the increasing attention by the industry due to their potentials in fulfilling demands for various engineering and consumers applications, such as consumer electronics, biomedical engineering, ophthalmic optics, automotive, electro-optics, aerospace engineering and mobile communications. Meanwhile, ultraprecision manufacturing technology is becoming one of the most effective methods for manufacturing high precision freeform surfaced components with functional features. Therefore, scientific understanding of ultraprecision manufacturing for freeform surfaces is essential and much needed, particularly for robustly fulfilling the gaps between fundamentals, technological innovations and their industrial scale applications. This doctoral thesis is focused on investigating a NURBS (Non-Uniform Rational B-Splines) based integrated approach to design, manufacturing and assessment of freeform surfaced optics and its implementation and application perspectives. Therefore, this doctoral research objectively covers NURBS based modeling and analysis of freeform lenses combining with e-portal development for customization, virtual lens conception and ray tracing simulation assessment, NURBS based toolpath generation and analysis considering design for manufacturing, micro cutting mechanics and the ultraprecision process, dynamic cutting forces modelling, and freeform surface topography generation and characterization, further supported by simulations and experimental trials.

The research reveals the integral process of design and manufacturing of freeform surfaced optics involves meticulous steps, including optic surface modeling and analysis, optic surface design, ultraprecision machining toolpath generation, simulation in both optical performance and machining cutting force on design for high precision manufacturing aspect, optic surface assessment in the digital mode, ultraprecision manufacturing physically, and quality assessment. Throughout the process, NURBS based modelling and analysis are the kernel, on which high precision is pursued and assured by the modelling/algorithms and the associated ultraprecision technology protocol. An integrated approach is developed and implemented through the web-based e-portal, for customized precision design and manufacturing of freeform surfaced varifocal lenses. The e-portal is specifically designed to meet the stringent demands of personalized mass customization, and to technically render a highly interactive and transparent experience of the lens design and manufacture for the lens users. By using Shiny and R-script programming for the e-portal development and combining COMSOL Multiphysics for the ray tracing simulation, the e-portal leverages open-source programming to provide the design responsiveness, manufacturing agility and accessibility. Furthermore, the integration of R-script and Shiny programming allows for advanced interactive information processing online, which also enables the e-portal driven ultraprecision manufacturing system for personalized freeform surface lenses.

Cutting force is a pivotal parameter in the ultraprecision machining process. However, scant emphasis is placed on elucidating the nuances of cutting forces and the associated cutting dynamics in ultraprecision diamond turning of freeform surfaces particularly using fast and/or slow tool servo modes. Theoretical analysis on the cutting force and its modelling are carried out in the ultraprecision diamond turning of freeform surfaces, particularly considering constant variations of cutting forces along the freeform surface curvature and the increasingly stringent requirement on high precision optical surface finishing. The cutting forces modelling is based on further developing the improved Aktins model while taking account of the influence of shear angles varying constantly along the freeform surface machining. Based on the toolpath data of the cutting process at the freeform surface, the depth-of-cut of the surface, curvature variations, and shear angle variations throughout the process are meticulously analyzed. Subsequently, the

cutting force modelling is developed to discern the nuances of the cutting motion by analyzing the cutting toolpath, and thus enabling the prediction of cutting forces variation during the cutting motions with a diamond cutting tool. Finally, an approach for examining the correlations between cutting forces and the surface texture, and surface texture aspect ratio is developed and further investigated, particularly against the functional performance of a freeform surface and its generation in ultraprecision machining. The investigation is also evaluated and validated by industrial application data.

The analysis and characterization of the freeform surface is essentially mandatory for the ultraprecision manufacturing process due to its high-precision 'deterministic manufacturing' nature and the ability to producing the manufacturing outcome without any additional process. The machine tool trajectory is remained on the surface and can be observed with high-accuracy metrology equipment, which makes the surface topography characteristics containing more valuable information as required for optics surface performance. The above-mentioned surface assessment protocol is developed as a part of the integrated approach, in which the surface texture aspect ratio is investigated particularly the relationships between the surface texture height variation and lateral feature, the underlying micro cutting mechanics affecting their formation and generation in the process, and the resultant optical performance of the freeform surface. Nanometric surface measurement techniques and 3D surface parameters are further explored to quantify the surface texture aspect ratio and assess its correlation with the surface optical performance. Experimental results demonstrate there is a significant correlation between the higher surface texture aspect ratios and increased aberrations, leading to decreased optical quality. Controlling the surface texture aspect ratio during the machining process is crucial for achieving the optimal surface functional performance. The research results above contribute well to the understanding of how the surface texture aspect ratio affecting the performance of freeform surfaced optic components, and provide insights for design and manufacturing of high-performance optical components, although optimization work is further needed in optics surface functionality and optical system design.

Acknowledgements

First and foremost, I would like to thank my supervisor Professor Kai Cheng. His precious advices, instructions, encouragement and invaluable support throughout my PhD study have led me go through the most difficult stages during the research process. Without his help and support, the completion of this research study would not have been possible. His professional, passion and commitment have definitely influenced and motivated my life not only in engineering research.

Personal appreciation is given to my colleagues, Dr Yohan Nor, Negin Dianat, Joe Armstrong, and Dr Guanhong Pan for their invaluable discussion, support, and their assistance in machining trials and metrology assessment in particular.

Special thanks also go to Liang Zhao and his team at GDJK Ltd in providing the varifocal lens samples and the white light interferometer for freeform surfaces analysis and characterization, the ultraprecision machine for machining trials, and interesting and helpful discussion on the freeform surface optics design and manufacturing.

Last, but not least, I would like to send my heartful gratitude to my parents; their unconditional love, patience, encouragement and tremendous support have been a powerful source, inspiration and motivation for all I have achieved so far in my life.

Declaration

I declare that, to the best of my knowledge, no portion of the work referred to in this thesis has been submitted in support of an application for another degree or qualification at this or any other university, or other institution of learning.

Table of Contents

List of Figures

List of Tables

Nomenclature

Symbols

L	Far-zone distance;
h	Lens corridor's length;
n	Refractive Index;
$r(u)$	Radius of Curvature;
Str	Surface Texture aspect Ratio;
rR	Lens near power;
rD	Lens distant power;
P_n	Spherical Power of near-view zone;
P_d	Spherical Power of far-view zone;
ADD	Addition power for varifocal lens;
SPH	Sphere power for varifocal lens;
CYL	Cylinder power for varifocal lens;
n	Refractive Index;
PSM	Prism, customer prism position;
AXS	Axis of the optics;
CT	Calculated center thickness;
D	Diopter of the optics;
ET	Estimated edge thickness;
h	Lens blank radius;
λ	Standard radiation wavelength;
N_{ring}	Standard number of rings;
P_{nom}	Standard entrance pupil diameter;

θ_x Standard X direction angle;

θ_y Standard Y direction angle;

v_x Ray direction vector, X component;

v_y Ray direction vector, Y component;

v_z Ray direction vector, Z component;

Vr Spindle rotation speed;

τ_y Shear yield stress;

μ The coefficient of friction;

r Tool radius;

D Objective diameter;

α Tool rake angle;

Abbreviations

AR	Augmented reality
CAD	Computer-aided design
CAM	Computer-Aided Manufacturing
CLPs	Cutter location points
CNC	Computer Numerical Control
CT	Center thickness
DoC	Depth of cut
ET	Edge thickness
FOV	Fields of view
FSO	Freeform surface optics
FTS	Fast tool servo
GPS	Standardized geometrical product specification and verification

HUD	Head-up display
LiDar	Light detection and ranging
MEMS	Micro-Electromechanical Systems
MSF	Middle spatial frequency
NA	numerical aperture
NURBS	Non-Uniform Rational B-Splines
OAP	Off-Axis Parabolic
PC	Polycarbonate
RBF	Radial basis functions
SEM	Scanning electron microscopy
SPDT	Single point diamond turning
STS	Slow tool servo
UPM	Ultraprecision machining
VR	Virtual reality

Chapter 1

Introduction

1.1 Background of the research

In the last two decades or so, UPM (Ultraprecision Machining) has been receiving the increasing attention from the industry, since the UPM technology has the ability to fulfill the industrial demands for high-accuracy complex components and devices in a range of engineering materials. Substantial progress in developing the machine accuracy has been achieved as shown in Fig.1.1. the diagram given by Taniguchi is to address the increasing requirement for precision machining and to provide a road map for predicting the exponential improvement in machining accuracy [1]. Micro cutting as an emerging subject area in its own right has attracted growing attention from both researchers and industry in the last two decades [2]. With the increasing demands for high precision components and products being considered in numerous industrial fields especially for aerospace, optics, energy, automotive, medical, and defence, ultraprecision and microfabrication facilities are becoming very important. The precision machining process is distinct from conventional techniques such as turning, milling, and drilling. UPM is essential to obtain the highest dimensional and form accuracy with the finest surface roughness, which typically does not need any additional finishing [7].

UPM is often using single point diamond turning (SPDT) processes, where single crystal diamond tools are employed, and by which the nanometric surface finish can be obtained. Fig.1.2 illustrates the most characteristic elements maintaining the dynamic specifications in a typical ultraprecision diamond turning system. Since the late half of 1990s, there has been a large amount of research and development on industrial UPM, which has been emerging as a promising technology used for optics manufacturing, including high value optical components

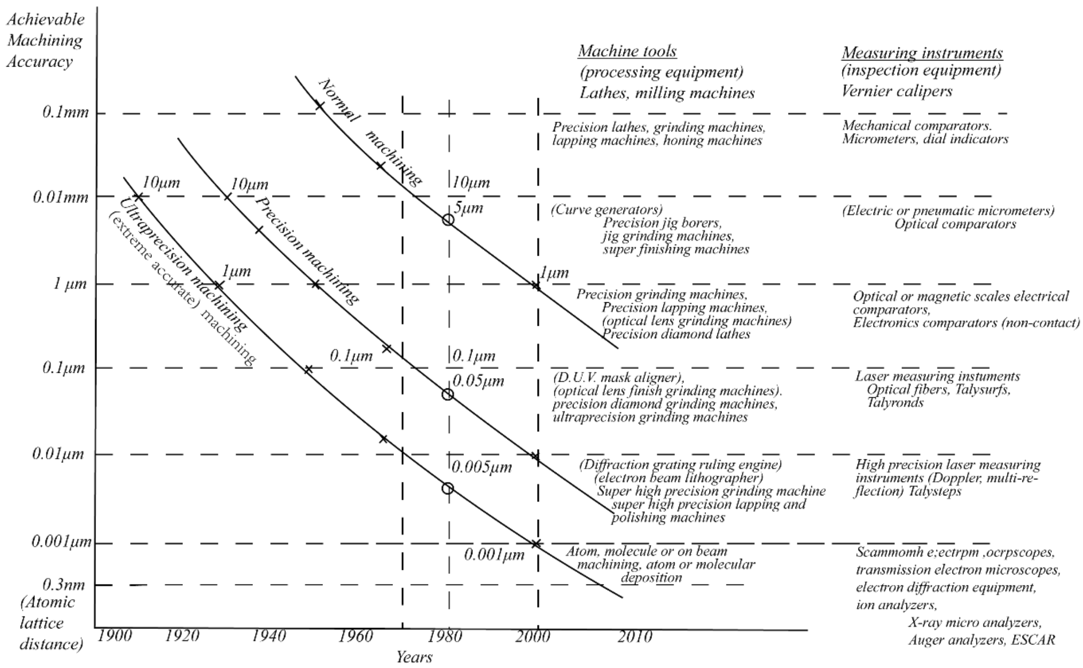

Figure 1.1 The development and importance of achievable machining accuracy [7].

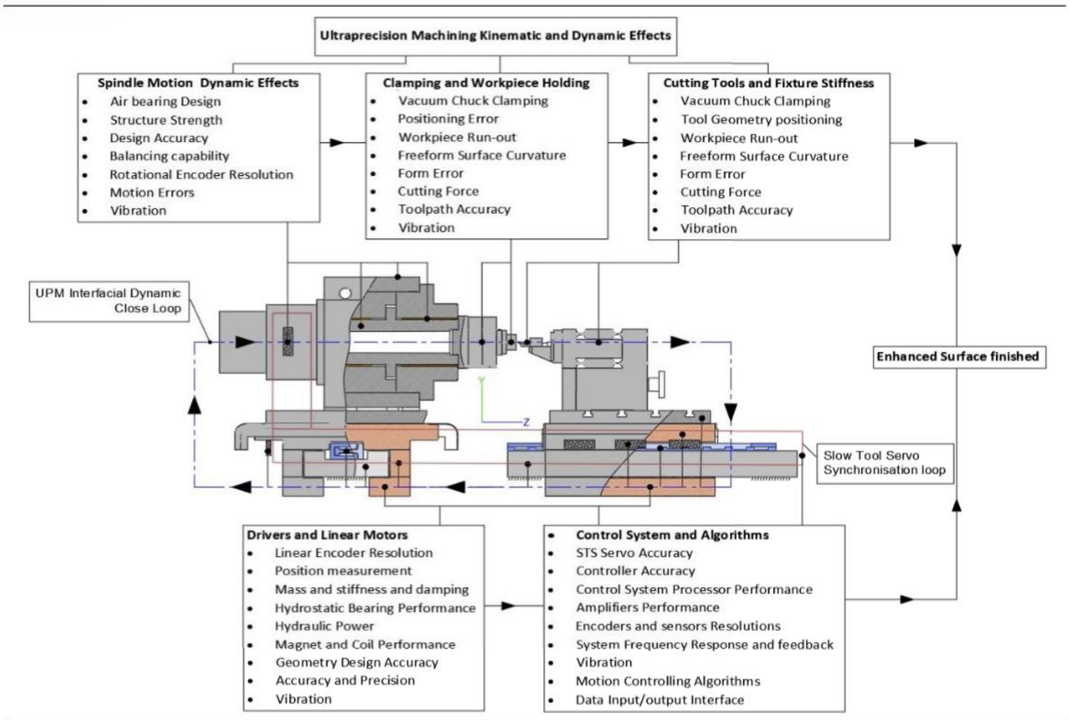

Figure 1.2 Components and their features of a SPDT diamond turning machine and its machining system [1] [7]. such as aluminum mirrors [3], aspheric optics.

such as aluminum mirrors [3], aspheric optics [4], head-up display devices [5], and freeform surfaced ophthalmic optics [6].

Freeform surfaces can be defined as surfaces with no axis of rotational invariance (within or beyond the optical part) [9]. This surface type requires and leverages three or more independent axes (e.g., the C -axis in diamond machining) to create an optical surface with as-designed asymmetrical features. In practical terms, in the context of design, a freeform surface may be identified by a comatic-shape component or higher-order rotationally variant terms of the orthogonal polynomial pyramids, themselves independent so they can be “dialed-in” at will. These components often come together with an astigmatic surface component. In simple terms, in design, freeform surfaces go beyond spheres, rotationally symmetric aspheres, off-axis conics, and toroids. Let us note that an off-axis conic is not a freeform surface because two axes are sufficient to fabricate and measure it. However, in some cases, making the conic with three axes is more practical. A toroid is a freeform in fabrication and metrology and may serve as a freeform base surface in design.

Fig.1.3 above illustrates the opportunity for a wide range of applications associated with imaging and non-imaging optics alike. In lighting and illumination, freeform surfaces tailor the light from a specified light source to a prescribed illumination pattern at high efficiency. [10], [11], [12], [13]. Similarly, optical transformations leverage freeform surfaces for high-efficiency quantum cryptography [14]. In both applications with a common theme of illumination or sorting, the optics’ precise shape is not as strictly defined as in imaging, where nanometer-scale precision is most often needed for aberration correction. Today, the emergence of freeform optics has permeated remote sensing and military instruments [15], [16], [17], [18], energy research [19], transportation [20], manufacturing [21], and medical and biosensing technologies [22]. Freeform optics have promise in both refractive and all-reflective unobscured systems. They both benefit from high performance and compactness, while all-reflective approaches provide the advantage of lightweight and achromatic solutions.

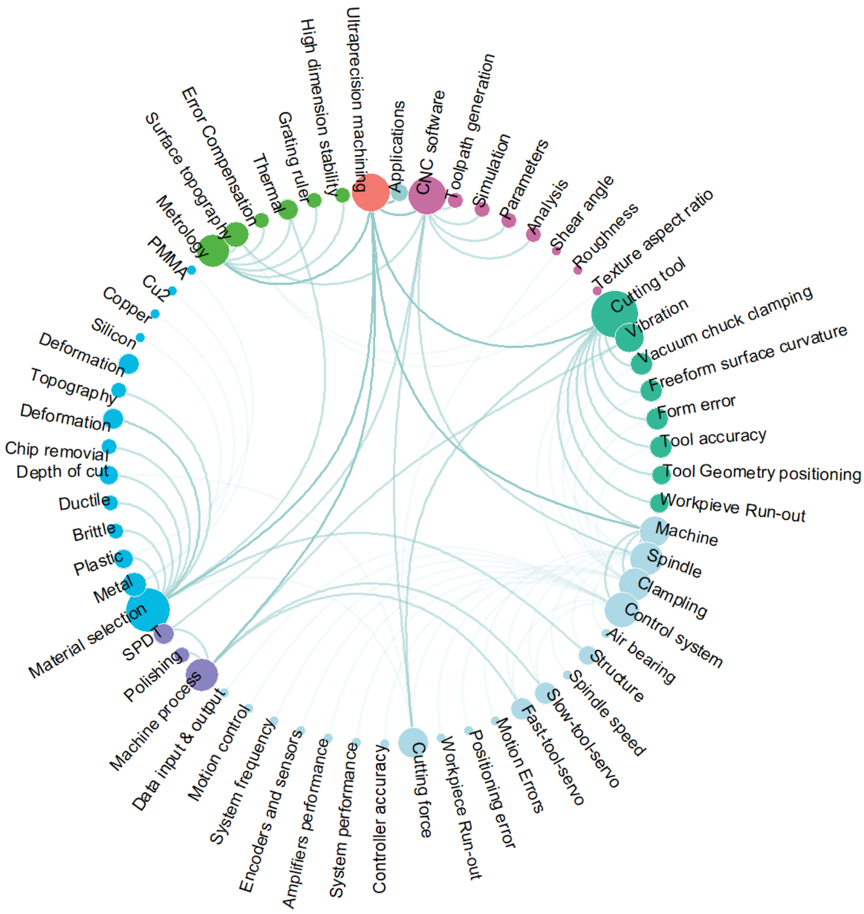

Figure 1.3 The thematic network of UPM process technology [8].

On the other hand, the rapid development of UPM technology also drives the development of the application of complex freeform surfaced components. Freeform surfaced components and devices have emerged as a vital and sought-after applied technology particularly for contemporary and future high-tech products and the industries, and been revolutionizing the field of optics. These components and devices are characterized by their non-traditional asymmetric shapes, enabling enhanced optical performance, and design flexibility. From a geometrical perspective [24], an optical freeform surface exhibits non-rotationally symmetric features, deviating from traditional symmetric shapes. In terms of fabrication and design [25], an optical freeform surface is further characterized as utilizing a third independent axis during the manufacturing process to synchronize creating precisely designed non-symmetric features on the optical surface. This unique approach allows for greater flexibility in shaping the surface to meet specific optical requirements and achieve desired performance. As it been illustrated in Fig.1.4, the demand for freeform surfaced optics has been substantially increasing due to their ability of improving the integral performance of optical systems and reducing their size, weight, and the unit cost. In the last decade or so, significant advancements have been made in the technologies of multi-axis fast/slow tool servo (FTS/STS) diamond turning applied to high precision manufacturing of freeform surfaced components and products including vari-focal lenses [141], HUD (Head-up display) [142] and LiDar (Light detection and ranging) devices, AR (Augmented reality) / VR (Virtual reality) optics, metalenses [143], and space optics in an industrial scale. These advancements have resulted in enhanced manufacturing capabilities for non-rotationally symmetric optical surfaces and challenges on efficient and effective assessment of the components and products at production floors. As a result, the applications of non-rotationally symmetric optical surfaces have expanded considerably, which have also opened new possibilities and increased the feasibility of incorporating such surfaces in various precision engineering related applications [26].

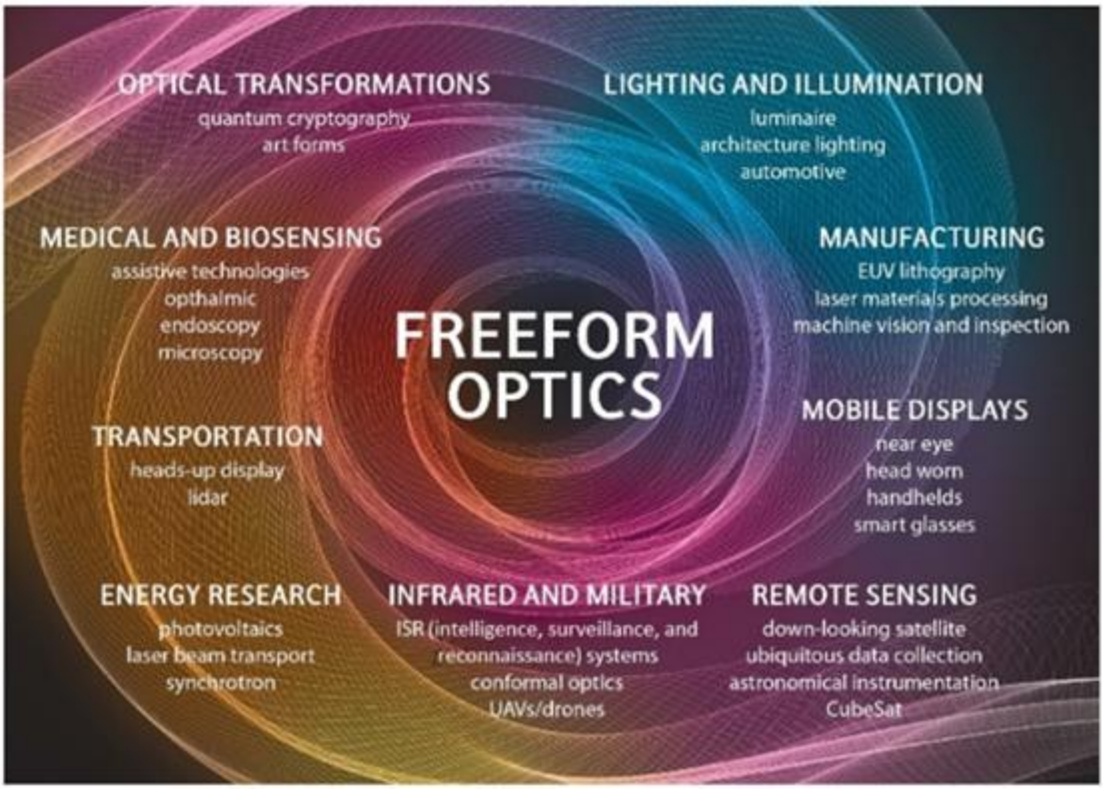

Figure 1.4 Schematic of freeform surface applications [23].

1.2 Scientific and technological challenges in design and manufacturing of freeform surfaced optics

Since freeform surfaces lack an axis of rotational invariance, their fabrication requires more than two degrees of freedom typical for conventional methods, with material removal via a sub-aperture mechanism [27]. These two common characteristics of freeform fabrication introduce challenges. Each additional degree of freedom adds error sources and increases the complexity of motion control [28]. Sub-aperture removal increases the fabrication time and introduces mid-spatial frequency (MSF) errors. Thus, error sources occur across a wide range of spatial wavelengths from figure to surface roughness, with processes applied to a wide range of materials, ductile and brittle, reflective and transmissive. The sub-aperture interaction zone affects the mechanisms of material removal. The main freeform fabrication processes are UPM, loose abrasive or bound abrasive finishing, molding/replication, and novel processes.

The community has long recognized the disadvantages of a serial design process in optical system development. In the state of art design process for optical system, the surface design is often specified by the customer and the functionality of the surface will be defined accordingly, while the manufacturing process is guided by the geometric constraints of the optical system. Such discrepancies between design specifications and manufacturing may mislead to the manufacturing process and lead to defects in the final product, resulting in surface quality degradation. Yoder (1986) quotes Johnson's conviction (in 1943) that "in the design of any optical instrument, optical and mechanical considerations are not separate entities, to be dealt with by different individuals" [29]. Kasunic (2015) documents that there can still be a chasm between optical and mechanical design tasks [30]. He states that "the lens designer's deliverable to the optomechanical engineer is a toleranced prescription with alignment and fabrication analyses developed in coordination with the optomechanical engineer; in practice, this is not always done." Johnson's and Kasunic's comments reflect a potential problem area and, indeed, a common challenge in developing state of the art on-axis systems. Experience with off-axis, freeform techniques demonstrates that more than "coordination" between optical and optomechanical design is needed. The entire engineering process must be concurrent.

The UPM process is often referred to as deterministic machining due to its high precision and accuracy, with surface roughness generated reaching up to the nanometric level. In the industrial of freeform surface optical components, high customization is the one of the most notable characteristics of UPM process. However, high customization often highlights the challenges in aligning optical design with manufacturing realities. The surface design is typically based on the unique specifications provided by the customer, while the manufacturing process is guided by the geometric constraints of the optical system. Discrepancies between design specifications and manufacturing constraints can lead to defects in the final product, resulting in surface quality degradation. Meanwhile, the fabrication of freeform surfaces presents a notable challenge due to the continuous changes in surface curvature. These dynamic alterations correspondingly lead to variations in cutting angles during the machining process. The inherent changes in curvature directly influence both the cutting angles and the depth of cutting (DoC) of the cutter, consequently affecting the cutting forces throughout the machining operation. Nevertheless, the cost of quality loss is becoming prohibitive for any manufacturing industry. Identification of specific corrective actions during or after the machining operation is quite tricky. Therefore, prediction and simulation in the early stage of UPM process are very helpful in quality controlling and characterization.

1.3 Aim and objectives of the research

This doctoral research aims to investigate the NURBS based integrated approach for freeform surfaced optics UPM, from its design modelling to the micro cutting mechanics in the ultraprecision manufacturing process, and further the surface functionality assessment and control, and its implementation perspectives, so to achieve the scientific understanding of the freeform optic ultraprecision manufacturing process and its optimization. With the research background, motivations, and the exploration and analysis above in mind, the following distinct objectives of the doctoral research are formulated, including:

(i) To continuously undertake the critical review on the state-of-the-art of the research field and **to identify the research and knowledge gaps**, particularly against the stringent industrial needs and the underling **scientific and technological challenges**.

(ii) To investigate **the NURBS based integrated approach to design, ultraprecision manufacturing and functional assessment of freeform surfaced optics,** for pursuing the customized high precision manufacturing of freeform lenses in the industrial-scale ultraprecision production manner.

(iii) To develop the **NURBS based design modelling and analysis** of freeform surfaced optics by combining **with web-based e-portal development in open sourced Shiny and R programming**.

(iv) To investigate the **modelling and simulations of cutting forces and toolpaths generation in ultraprecision diamond turning of freeform surfaces** based on improved Atkins model, while further supported by MATLAB/Simulink programming and NANOCAM3 and NANOCAM4 environment.

(v) To develop the **conception of virtual lens and its assessment protocol** by combing ISO standard) and 3D surface parameters for a freeform surfaced lens, and furthermore to investigate the **intrinsic relationship between the surface texture aspect ratio and the optics functional performance** broadly.

(vi) To further **evaluate and validate the NURBS based integrated approach through a series of simulations, experimental results and industrial data combined** in a holistic manner while mostly supported by the digital environment.

1.4 The structure of the thesis

Fig.1.5 provides an illustration of the scope and structure of the thesis, and the research logic flow throughout this doctoral research process as envisaged and the underlying integrated methods involved.

Table 1.1 further lists and briefly describes each chapter in the PhD thesis context.

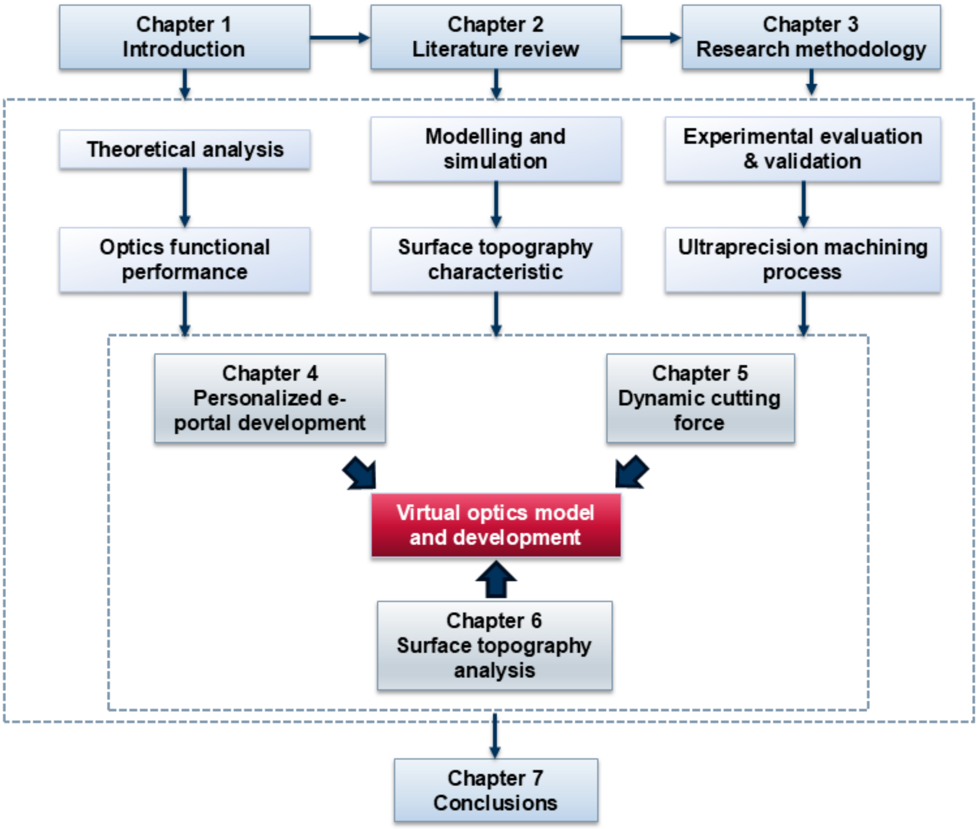

Figure 1.5 The scope and architecture of the thesis.

Table 1.1 A list of chapters in the thesis and their brief descriptions.

Chapter	**Description**
Chapter 1: Introduction	Chapter 1 introduces the research background of UPM and briefly history of freeform surface. The scientific and technological challenges are involved in this chapter. The scope

	of the full thesis is presented after the aim and objectives of this research
Chapter 2: Literature review	Chapter 2 reviews peer research on freeform surface optics, including applications of FSO, fabrication techniques, and material selection strategies to enhance the comprehensiveness of the FSO industry. Furthermore, it examines personalized design and modeling principles critical for freeform surface design development. After that, this chapter also evaluates assessment methods for surface topography, optical performance, and machine mechanics in FSO applications. Finally, Chapter 2 concludes by focusing on defining e-Manufacturing frameworks specific to FSO.
Chapter 3: Development of the NURBS-based integrated approach for design and ultraprecision manufacturing of freeform surfaces	Chapter 3 firstly presents the framework of the research, then a NURBS-based approach of design modelling and manufacturing of FSO has been presented. Research methodology, assessment principle, and the developed cutting force method, utilized in this research and experimental set-up are further elaborated
Chapter 4: A web-based e-portal for integrated design, manufacturing and assessment of lenses and its implementation	In this chapter, an integrated system of FSO from design, modelling and analysis has been proposed, a web-based portal for freeform surface optics has been proposed based on the purposed of high responsiveness manufacturing of FSO. The portal integrated surface design, surface topography analysis, raytracing simulation for surface optical performance assessment and 3D surface model construction based on the NURBS method.
Chapter 5: Dynamic cutting forces modelling and analysis	In this chapter, a dynamic cutting force modelling for ultraprecision machining process has been proposed. With the idea of exploring the cutting force variation in different curvature radius of freeform surface during the machining processing. The date been used on the model is the toolpath for machining directly extracted from ultraprecision CNC machining software to maximum matching the simulation to the real scenario of machining process. The mathematic function of the method and an experiment of validation have been launched with a comprehensively analysis with multiple parameters.
Chapter 6: Assessment of FSO surface texture characteristics using 3D surface parameters and	Explores the correlation between 3D surface parameters and the functional performance of ultra-precision machined freeform optics surface. With the Observation with an electronic microscope, the regions exhibiting different phenomena display different characteristics in 3D surface parameters' value. A

the virtual optics model	correlation analysis of these data has been developed.
Chapter 7: Conclusions and recommendations for future work	The conclusion gives an overview of the project with respect to how the objectives have been achieved in the chapters of the project. This is followed by a recommendation for future work.

Chapter 2

Literature review

High-precision freeform surface components and devices are in increasing demand across various engineering industries, including consumer electronics, automotive, biomedical engineering, MEMS, electro-optics, aerospace, and communications. Over the past decade, ultra-precision manufacturing technology has been increasingly applied to the production of mobile phones, security monitoring systems, head-up displays, personalized ophthalmic lenses, and AR/VR/smart glasses on an industrial scale. The potential drawbacks of UPM significantly hinder its widespread applications. The scientific and technical challenges mentioned in Chapter 1 are urgently need to be solved in order to obtain the industrial demands on machining efficiency, cost-effective, reliable, accuracy and consistency. This chapter surveys the research background and the previous research achievements in UPM area particularly for the freeform surface manufacturing from design, modelling, to surface assessment and the state of art machining technology. In addition, the knowledge gaps for the previous investigations are identified subsequently.

2.1 Freeform surfaced optics (FSO)

2.1.1 FSO and their applications

Anamorphic lens, as the earliest optical surface shape without rotational symmetry, using toroidal surface with circular profiles and two radii along two orthogonal axes, was first used in periscopes during World War I to obtain an extended outside vision for tanks. The Hypergonar lens, designed by Henri Chretien in 1927 for photography and motion capture, revolutionized cinema in the 1950s [31]. In imaging applications, anamorphic surfaces defined as toroidal aspheres first took on the freeform denomination in a 2004 publication on all-reflective optical systems [32], heralding the emergence of more complex surface shapes than the conventional rotationally symmetric aspheres. Progressive ophthalmic lenses pioneered the emergence of freeform optics in the marketplace and mass production[33]. another early invention in ophthalmics is the Alvarez lens, which creates a variable focus using two cubic-shaped lenses displaced laterally relative to each other. The Alvarez is still commonly used today to enable variable focus in visual instruments [34], [35].

In recent decades, freeform surfaces have been widely used in aerospace, automobile, consumer products and the die/mold industry. Freeform surfaces are usually designed to meet or improve an aesthetic and/or functional requirement. FSO applications are often been used in optical system. With the development of technology, the requirement of people to optical system has been drastically greater: 1). The optical system is required to develop in the direction of large field of view, large aperture, wide band, etc. while achieving good image quality to meet the needs of different tasks; 2) Less components, smaller size, and lighter weight; 3) For some applications, the optical system needs to realize special imaging functions, such as environmental zoom, image plane translation and rotation, etc.; 4) In order to eliminate light obstruction in the system or to achieve a special, compact system structure, the system often uses eccentric tilting elements [36]. While the traditional surface components might not meet such upgraded design requirement due to its low freedom and inflexibility structure. Thus, the design of imaging optical systems urgently requires to find a new type of complex freeform surfaces.

Today, the emergence of freeform optics has permeated remote sensing and military instruments, energy research, transportation, manufacturing, and medical and biosensing technologies. Freeform optics have promise in both refractive and all-reflective unobscured systems. They both benefit from high performance and compactness, while all-reflective approaches provide the advantage of lightweight and achromatic solutions. In the following contents, some of the FSO applications has been listed and illustrates.

(1) Vari-focal lens

Loss of accommodation of the eye owing to the increase of ages can cause the loss of the ability of the eye to focus on nearby objects [37]. This symptom is called presbyopia. Presbyopia is a natural, often part of aging, which usually becomes noticeable in early mid-40s and continues to worsen until around age 65 [38]. In response to minimize the influence of presbyopia, elderly people who are diagnosed with presbyopia always prepare two pairs of single-vision spectacles to have both clear visions of near and distant range. Therefore, the invention of multifocal lenses such as bifocal lens and trifocal lens is inevitable and brings multiple vision into one glasses for elder people to compensate presbyopia. However, the design methodology of the multifocal optics induced the default in sudden change in optical power happening at the contour of the segment, such as jump images, ghost reflections at the segment line, and an unsightly segment, especially when the line is clearly visible [39]. The limitation of multifocal lenses is the lack of intermediate addition values needed for advanced hyperopes [40]. Nowadays, with the flexibility brought by freeform technology, varifocal lens has not only facing to elder people, but also become an increasingly popular to all age paper as a common approach to controlling and adjusting presbyopia [41].

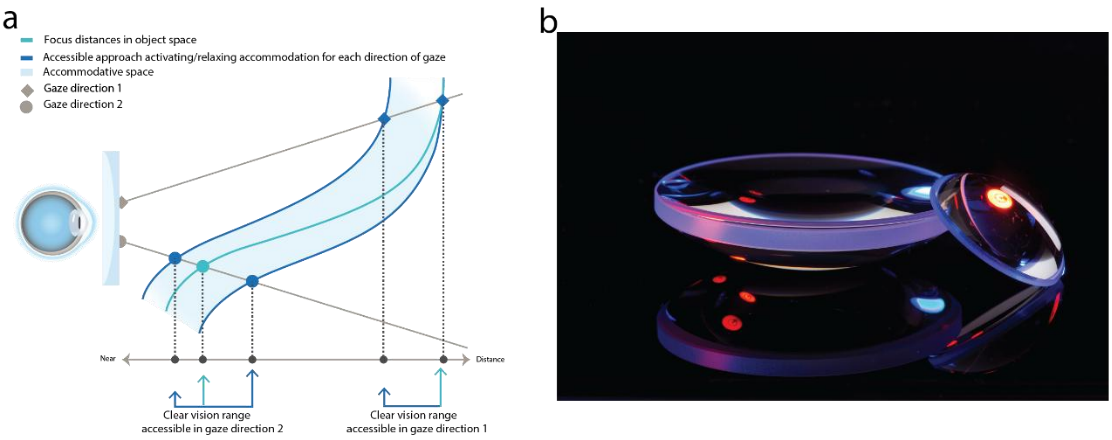

Figure 2.1 a) schematic of the functionality of varifocal lens; b) Photo of lens blank and produced varifocal lens.

The schematic illustrates in Fig.2.1(a) interpreted the fundamental functional logic of varifocal lens with a photo of a produced varifocal lens shows in Fig.2.1(b), the design of a varifocal lens often focus with the one surface (convex or concave surface) and leave another surface of the lens as a spherical surface with zero power [39]. As it illustrated in the Fig.2.2, a varifocal lens consist with three main zones, the far view zone, intermediate corridor and near view zones, where the far zone is located in the upper part of the lens and the near zone is located in the lower part of the surface, and intermediate corridor in the middle of the lens connected near view zone and far view zone with a smooth and progressive transition between the power of the near and far view zones [39] and a peripheral area that flanks the three zones where there is a presence of geometric distortion and blur [38]. The curvature on the surface has a gradual increment from a minimum value in the far view zone to a maximum value on the near view zone and therefore producing the desired effect of the addition power [38]. This change produces a corridor where the power changes progressively in the intermediate zone [38]. The method of varifocal lens design has been detailly interpreted in section 2.4

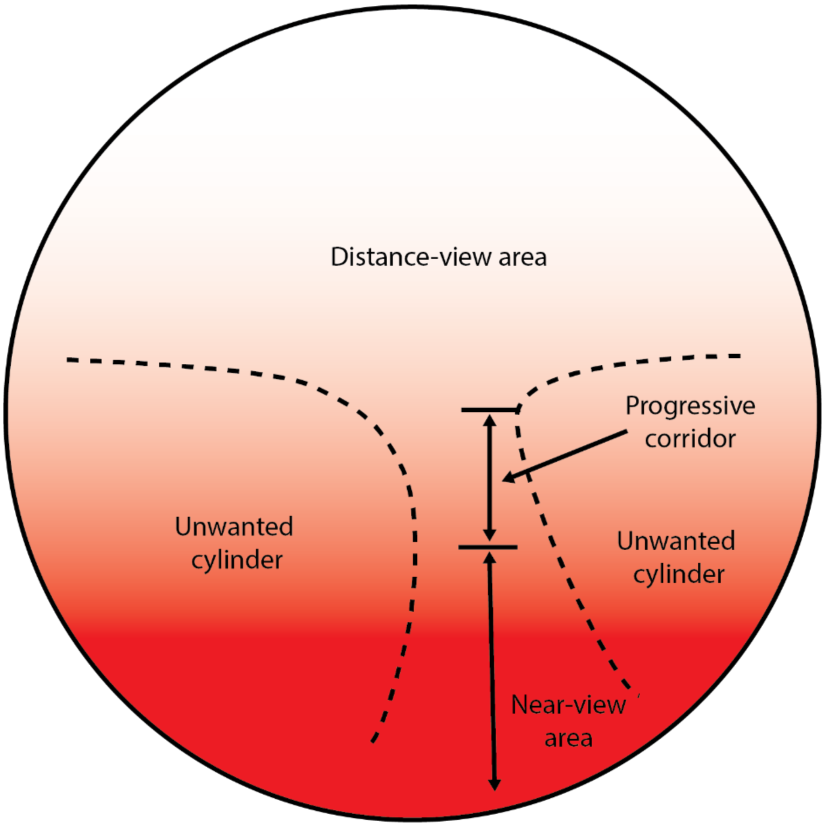

Figure 2.2, The basic construction of a varifocal lens consists of a distance view area in the upper position of the lens and a near view area in the lower central position of the lens, and a progressive corridor between the distance and near areas.

(2) Off-axis parabolic mirrors and their applications

An Off-Axis Parabolic (OAP) mirror have the ability to direct and focus incident parallel light at a specific angle, which can transfer plane waves into spherical waves and spherical waves into plane waves. It has been widely application in modern ophthalmic optics area, and optical interaction investigations, i.e. spectrometers [42], interferometers [43], astronomical optical instruments [44], spectrum analyzers [45], and in beam expanders and beam collimators [46]. The manufacturing of an off-axis parabolic mirror presents high requirements of nano-level's surface roughness and high accuracy alignment of the mirror design,

Fig.2.3 illustrates the alignment of an OPA mirror and the design method of the mirror surface. Three main elements are used to define the mirror, as illustrated in Fig. 2.3. In the plot, D indicates the distance of the parallel incident light spot, while F defines the focal length of the mirror. The parameters L1 and L2 represent the length of the top light spot and the width of the non-flat top light spot, respectively. Additionally, Df denotes the distance between the rotational machining axis and the principal axis of the lens.

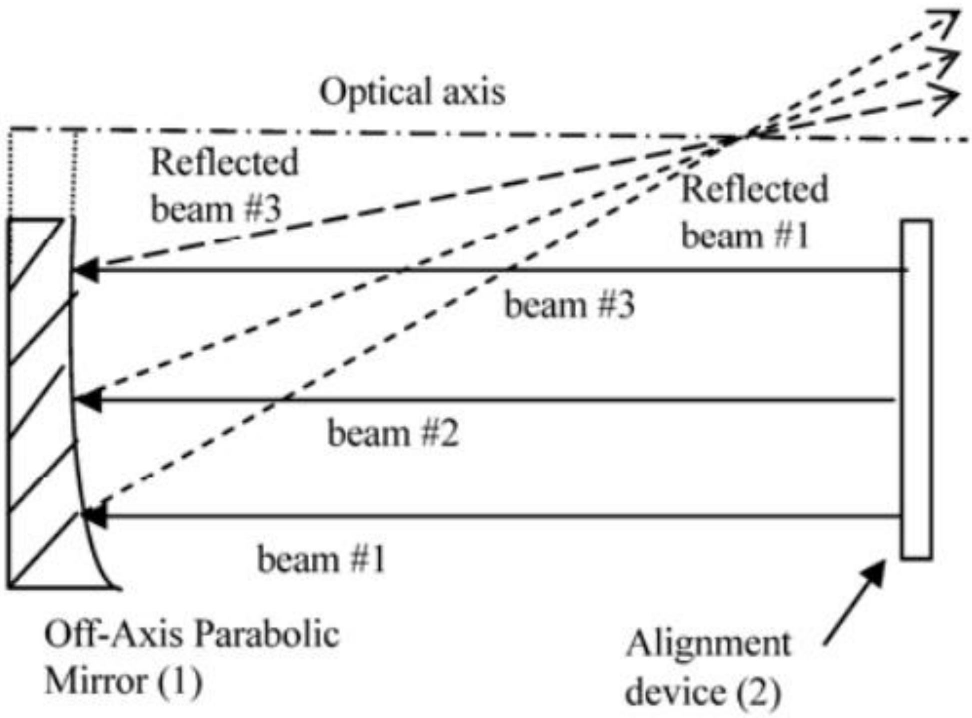

Figure 2.3 Alignment of an off-axis parabolic mirror [148].

(3) F-theta lens

F-theta lenses are widely used in remote laser processing, and a large variety of scanning systems utilizing these lenses are now commercially available [47]. In traditional optical imaging, the image height H and the scanning angle θ have a nonlinear relationship ($H = f \times tan\theta$), which does not satisfy the requirements for linear imaging. To achieve a linear imaging relationship ($H = f \times \theta$), the lens surface intentionally designed the freeform surface with "negative distortion," resulting in the creation of F-theta freeform lenses.

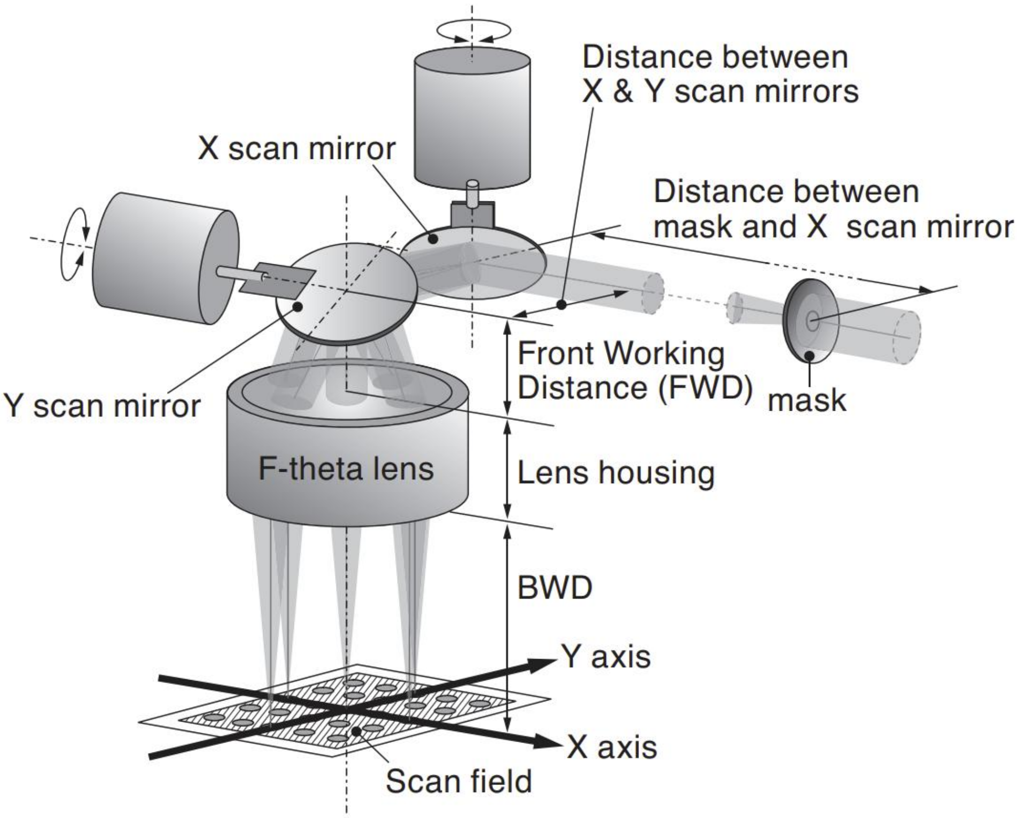

Figure 2.4 Application of f-theta lens using on laser drilling [48].

Figure 2.4 outlines a case of study of f-theta lens using on a laser drilling machine. The oscillator emits a laser beam, which is directed toward a target spot on a PWB via scan mirrors high-speed controlled by a two axis Galvano-scanner and via an f-theta lens that converges the beam for processing [48].

(4) Microlens arrays

Microlens arrays are a key component in the development of 3D imaging systems due to their exceptional optical properties, including extremely large field-of-view angles, low aberration and distortion, high temporal resolution, and infinite depth of field [49]. Since the 1980s, various methods have been used to fabricate microlens arrays, such as Micro-Electromechanical Systems (MEMS)-based technologies [50], [51], [52], [53], [54], [55], [56], [57] and ultra-precision machining technologies [58], [59], [60]. One of the primary challenges in microlens array fabrication is achieving high fabrication and assembly accuracy over a large area [59], [60], [61]. The image resolution of a compound eye optical system increases with the number of microlenses and the radius of each microlens unit. While enlarging the overall size of the microlens array can address deficiencies in resolution, ensuring uniformity over a large area remains a significant challenge [59]. Furthermore, to create more compatible systems with larger fields of view (FOV), fabricating microlens arrays on flexible layers or curved surfaces, similar to the compound eyes of fruit flies (Drosophila), introduces additional complexities to the manufacturing process [62].

In the design of the microlens array using in most artificial compound eye optical systems, the microlens array—acting as the counterpart to ommatidia—is arranged on a planar surface, as illustrated in Fig.2.5, to align with Charge-Coupled Device and Complementary Metal-Oxide-Semiconductor sensors. The fabrication process for planar microlens arrays is also significantly simpler compared to other configurations.

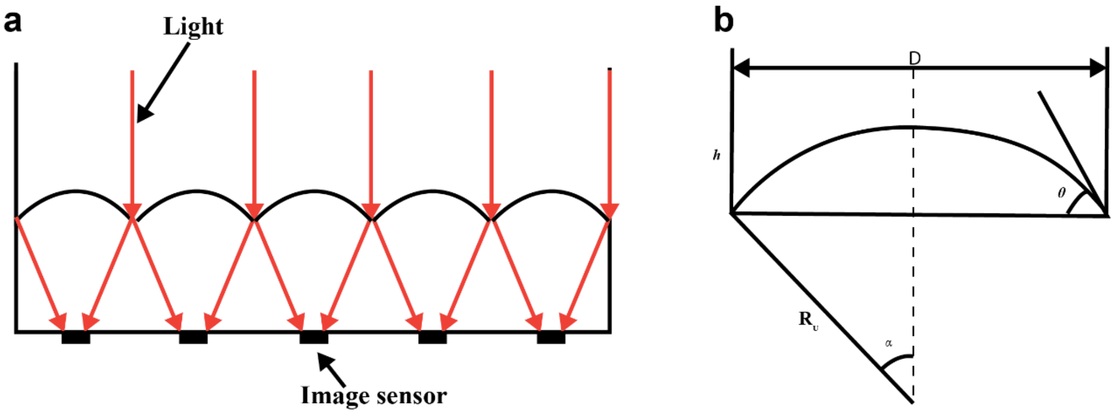

Figure 2.5 a) Artificial compound eye optical systems with planar structure; b) Geometry parameters setup in microlens surface design.

For each unit of the microlens array, the geometric dimensions are determined by the pitch (D), height (h), radius of curvature (Ru), and contact angle (θ), as shown in Fig.2.6. These parameters can be measured using optical microscopy, scanning electron microscopy (SEM), and contact profilometry. The quality assessment of the microlens array is typically characterized by its numerical aperture (NA), surface roughness, and array uniformity.

The numerical aperture of the micro lens is been calculated by using equation (2.1) [63]:

$$NA = n \cdot \sin\alpha \tag{2.1}$$

Where n is the refractive index of the medium between the object and the microlens. The half aperture angle α can be obtained by height (h) and the radius of the curvature (Ru):

$$\alpha = \arccos\left(\frac{R_u - h}{R_u}\right). \tag{2.2}$$

The increase of the value of NA leads to the increase of the resolution and magnification of the microlens. The contact angle θ is equal to half aperture angle α and the F-number is defined by the equation (2.3) [64]:

$$F^{\#} = \frac{1}{2n \cdot \sin\alpha} \tag{2.3}$$

2.1.2 Fabrication of FSO

Conventional and advanced fabrication methods for the ultra-precision machining of freeform surface optics have been extensively reviewed in numerous research studies. Among these, 3-axis and 5-axis CNC machines are the most commonly used for machining freeform surfaces [65]. The development of Single Point Diamond Turning (ultra-precision machining can be traced back to the 1950s, when the process was initially applied to non-ferrous metals such as aluminum and copper [66], [67], [68], [69]. By the 1970s, significant advancements in materials, tools, and processing techniques had transformed ultra-precision machining into a powerful tool for fabricating precise optical components. In the 1980s, the technology found successful applications in manufacturing optical drums for copiers, reflectors for scanners, and memory disks for computers. These advancements achieved sub-micron form precision, with surface roughness reaching nano-scale levels.

Ultra-precision machining represents the pinnacle of precision machining technology. With rapid advancements in machining techniques, the capabilities of machines have significantly improved over each decade. Processes that were once considered "precision machining" are now regarded as ordinary machining. Consequently, there is no fixed or universally accepted definition to clearly distinguish between precision machining and ordinary machining. In the current state-of-the-art ultra-precision machining technology, resulting surfaces can achieve nano-scale precision. Fig. 2.6 illustrates the trend of increasing accuracy magnitudes achieved by various machining methods over time[70].

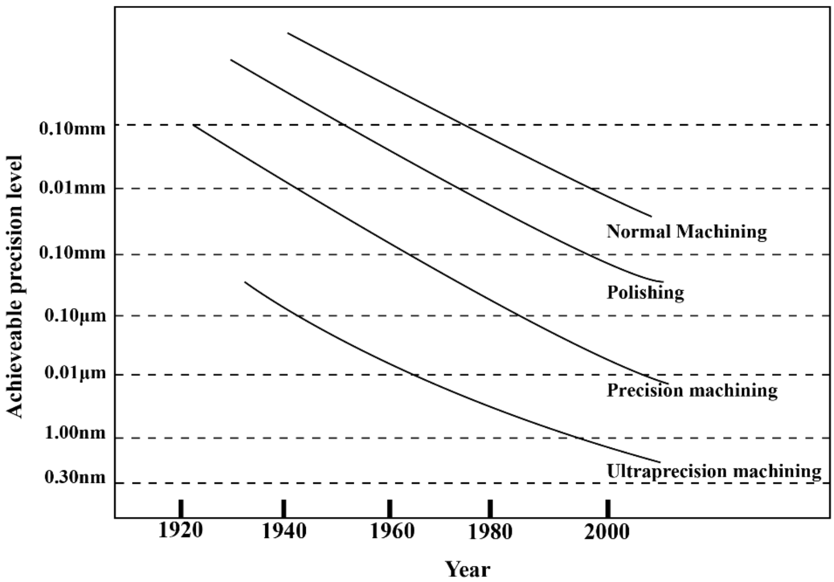

Figure 2.6 The achieved machining precision levels and its development trends.

There are numerous industrial ultra-precision turning and milling machines available for manufacturing precision components, with most targeting the optical components market. Fig.2.7 illustrates examples of industrial ultra-precision machines with micro-cutting capabilities, which can be categorized into two types [2].

Figure 2.7 Industrial precision machine tools with micro cutting capability[2]: a) Kern micro; b) Sodick AZ15; c) Fraunhofer IPT Minimill; d) Makino Hyper 2J; e) Kuglar MicroMaster MM2; f) Fanuc ROBOnano; g) Precitech freeform 700 Ultra; h) Moore Nanotech 350FG.

The first category includes conventional ultra-precision machine tools designed as diamond turning machines, often equipped with additional Z-axis capabilities, rotary tables, and secondary high-speed milling or grinding spindles. Notable examples are the Moore Nanotechnology Nanotech 350FG and the Precitech Freeform 700 Ultra. These machines typically require 5–7 m² of floor space. However, their high cost and limited flexibility restrict their application to micro-components with simple geometries and high added value, such as optical components. The second category consists of industrial precision micro-milling machines, which have emerged in the last decade. A representative example is the Kern Micro machine, which supports diverse applications but faces challenges in achieving the machining accuracy required for precision micro-machining due to positioning limitations. The key requirements for ultra-precision machining applications are: high dimensional precision, typically better than a few microns; accurate geometrical form, typically within 100 nm deviation from flatness or roundness; and excellent surface finish, in the range 10–100 nm of Ra value.

2.2 Material selection for FSO

The physical, chemical, and optical properties of an FSO are determined by the combination of three key elements: the material of the lens, the geometry of its surfaces, and any coatings applied to these surfaces [40]. Therefore, understanding the primary properties and characteristics of ophthalmic materials is crucial for selecting the material that best meets the design requirements. This step forms the foundation of the surface design process, ensuring optimal performance and quality in the final product.

The material influence, in other words, the refractive index of the lens is the first challenge needed to be considered for a designer to design a freeform surface. There are three main parameters that affect the properties of lenses are the surface geometry, the coatings applied to them and the material, the two main families of materials used in the ophthalmic industry are glasses and plastic (polymers) and the understanding the effect that they have on the lens important for designers to select the correct material for each application [40]. One of the main property of the materials used in ophthalmic design is the refractive index (n) which for a wavelength is the ratio between the speed of light in a vacuum and the speed of light in the material, this value is always greater than 1 because the speed of light will in the vacuum is always faster than in the material, the refractive index has a relation with the curvature and thickness of the lens [40].

Material specification and selection play a crucial role in optical surface design. It not only affects the resulting optical performance, refractive index, and radius distribution, but also influences the thickness ----center thickness (CT) and edge thickness (ET) of the lens product. Edge configuration constitutes critical consideration due to the pronounced "edge effect" phenomenon [130]. Experimental characterizations reveal that higher levels stress at the edge of the optic induce birefringence and surface irregularities. Consequently, to allow injection of molten plastic into the lens cavity, industry specifications mandate that the effective aperture extend 1-2 mm beyond the nominal clear aperture, establishing a stress dissipation buffer zone that concurrently addresses edge diffraction artifacts through Fresnel number optimization [130].

The optical power of an optics surface is indicating the ability of the lens to bend or refract light is generally expressed by its vertex power. The vertex power is the inverse of the lens's focal length measured in meters. Its unit is called Dioptre, represented by the symbol "D". According to the formula (2.4), CT and ET of a lens based on its optical power (D), Refractive Index (n), and Diameter (d), can be calculated.

$$CT - ET = \frac{D \times h^2}{2000 \times n} \tag{2.4}$$

One of the primary properties of materials used in ophthalmic design is the refractive index (n), defined as the ratio between the speed of light in a vacuum and the speed of light in the material for a given wavelength. This value is always greater than 1, as light travels faster in a vacuum than in any material. The refractive index is directly related to the curvature and thickness of the lens [40]. In ophthalmic optics, the refractive index plays a crucial role because it connects the optical properties of a lens—namely, refractive and prismatic power—with the lens geometry, particularly curvature and optics thickness (the distance between concave surface and convex surface).

$$P = (n-1)\left(\frac{1}{R_1} - \frac{1}{R_2}\right) = (n-1)K \tag{2.5}$$

Equation (2) represents the example of this relation, which links the power of a thin lens P with the radii of curvature R_1 and R_2 of the two lens surfaces through the refractive index n. By combining these geometric factors into a single parameter K, it becomes evident that the same lens optical power can be achieved with different combinations of materials and curvatures. Refractive indices for glass materials range from 1.5 to 2, while those for plastics vary from 1.498 to 1.74 for high-index polymers [40]. Table 2.1 summarizes the properties of the most common materials in the ophthalmic industry [71].

Table 2.1 Summary of the main specifications of a selection of ophthalmic materials.

Material	Refractive Index(n)	Abbe Number	Density (kg/m^3)	Type
Crown	1.523	58.6	2.54	Glass
1.6/41	1.601	41.5	2.63	Glass
1.7/42	1.7	41.6	3.21	Glass
1.8/35	1.802	34.6	3.65	Glass
1.9/32	1.885	31.9	3.99	Glass
PMMA	1.49	58	1.18	Plastic
CR-39	1.498	58	1.3	Plastic
Trivex	1.527	44	1.11	Plastic
Polycarbonate	1.586	34	1.22	Plastic
MR-8	1.592	51	1.3	Plastic
Tribrid	1.607	41	1.23	Plastic
Mr-10	1.661	32	1.37	Plastic
Mr-174	1.732	33	1.47	Plastic

In this study, a commercial injected PMMA and PC ophthalmic lens blank has been selected for investigating varifocal lens manufacturing.

2.3 Personalized design and modelling of FSO

The design of optical imaging systems originated in the United Kingdom. Before Abbe's pioneering work in 1868, the field lacked a rigorous theoretical foundation, relying instead on accumulated experience. Optical systems were predominantly crafted by mechanical artisans and glassmakers. Abbe's introduction of a systematic design theory in 1868 was revolutionary, defining key concepts such as distortion and aberration. This framework laid the foundation for modern optical design and continues to influence the development of various optical imaging systems today [40]. Freeform surfaces, integral to many modern optical systems, are defined by three distinct characteristics: non-planarity, non-rotational symmetry, and non-quadratic geometry [23]. Nowadays, there are two different methodologies for freeform surface design, as it has been illustrated on Fig.2.8 [72], first is selection from existing design method from patents or other existing systems, this method has been widely adopted and applied on the mass production of FSO manufacturing; another approach is designing a surface based on aberration theory followed by the optics requirement with the optimization of novel technologies such as machining learning, this approach are more suitable on the design of optical system.

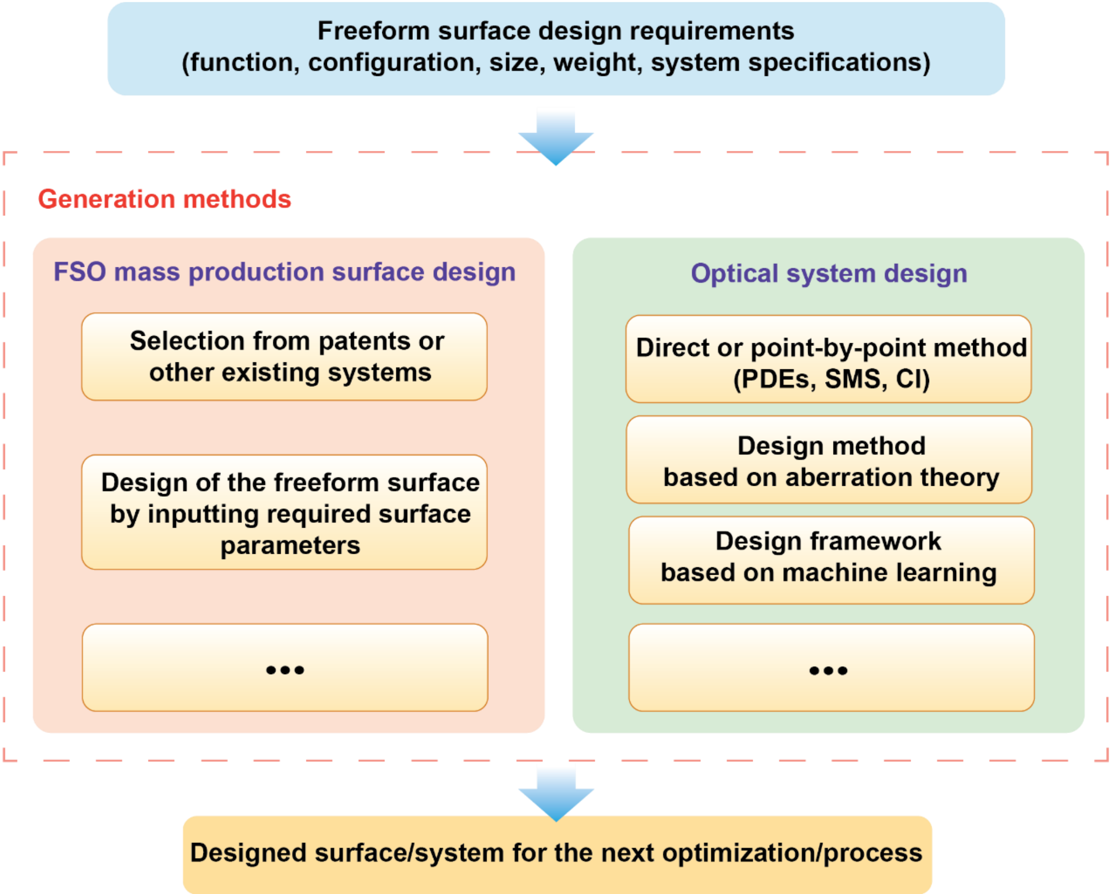

Figure 2.8 Flowchart of the methodologies of freeform surface design method.

With the diversification of optical components, the design of optical systems has evolved from traditional single-axis symmetrical designs to more versatile three-dimensional spatial configurations. These new designs are more flexible and complex in both form and structure. Moreover, with the advancement and widespread use of computer-aided design (CAD) software, optical design has expanded in multiple directions [135]. Optical components in various imaging and illumination systems—such as digital camera lenses, laser printer lenses, scanner lenses, projection lenses, diffractive optical elements, progressive lenses for presbyopia, head-mounted displays, rear reflectors in projection TVs, automotive headlight reflectors, polygonal mirrors, lampshades, light guides in flat-panel display backlight modules, and LED lighting systems—have all been extensively studied for freeform optical surface design.

The following section is primarily focused on the design method applicable to varifocal lenses.

2.3.1 Varifocal lens surface design

The development of varifocal optics aimed to address the issues associated with bifocal lenses, particularly the abrupt power change at the segment contour. Problems such as image jump, ghost reflections along the segment line, and the unaesthetic appearance of a visible line made bifocal lenses less desirable. From an optical perspective, the primary limitation of bifocal optics was the absence of intermediate addition values required for advanced hyperopes. This created an urgent need among opticians, optometrists, and optical designers to develop a multifocal lens where power could transition smoothly from the distance to the near vision areas. The first documented proposal for a varifocal lens design was presented by Briton Owen Aves in a UK patent filed in 1907 [73]. Aves described a lens with a progressive cylindrical front surface that curved along the vertical meridian, and a back surface shaped as a conical patch with a vertical cone axis, providing progressive curvature along the horizontal direction. However, this design generated significant amounts of astigmatism and could not easily incorporate astigmatic prescriptions into either surface.

In 1962, Vold and Weinberg [74] proposed splitting a lens into three distinct parts: upper and lower regions with constant surface power, connected by a horizontal "cylinder" with progressive power. In their research, they assumed a progressive cylinder with a horizontal axis, as shown in Fig. 2.9. The curvature of this cylinder could be freely defined from top to bottom. For example, as illustrated in Fig. 2.9, the upper region of the surface has a constant curvature $C_f = \frac{1}{R_f}$, the lower region has a constant curvature $C_n = \frac{1}{R_n}$, and the middle third is the progressive section, where curvature transitions from the upper to the lower value. The total curvature change is represented as $\Delta C = C_n - C_f$. To construct the lens, Vold and Weinberg created a second surface with opposite sign curvature. They rotated the first surface by 45°and the second by −45°, then combined them as shown in Fig. 2.10. These surfaces became the front and back sides of the lens, contributing progressive cylindrical power with the same sign. As depicted in Fig. 2.10(a), the oblique lines inside the rotated cylinders represent the power meridian, with lengths proportional to the local curvature. Fig. 2.11(b) shows the combination of the two cylinders, where their axes are perpendicular to each other everywhere when the cylinders are progressive. The resulting lens power can be read as a cross-cylinder prescription, with ellipses in the figure indicating the local power of the lens. Using this method, Vold and Weinberg developed a varifocal lens capable of arbitrary continuous power increases along the vertical axis, free from astigmatism in the upper and lower regions, with cylinders combining to maintain stable curvature. However, the technique has limitations: the curvatures of the cylinders align only along the vertical meridian or in regions where both cylinders have stable curvature. Elsewhere, an imbalance occurs between the cylinders, rendering the local power astigmatic. In this construction, the maximum unwanted astigmatism equals the total addition of the curvatures.

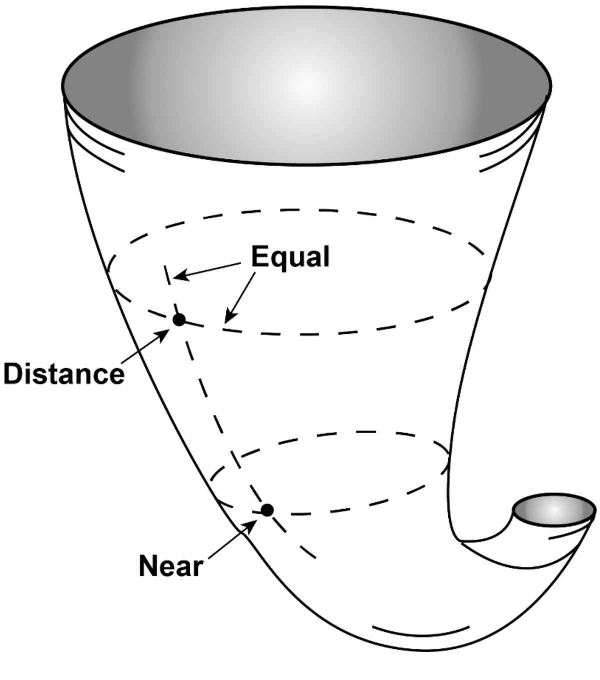

Figure 2.9 The net optical effect of several early progressive lenses, including the original dual-surface

design of Owen Aves and the first commercially successful progressive lens [75].

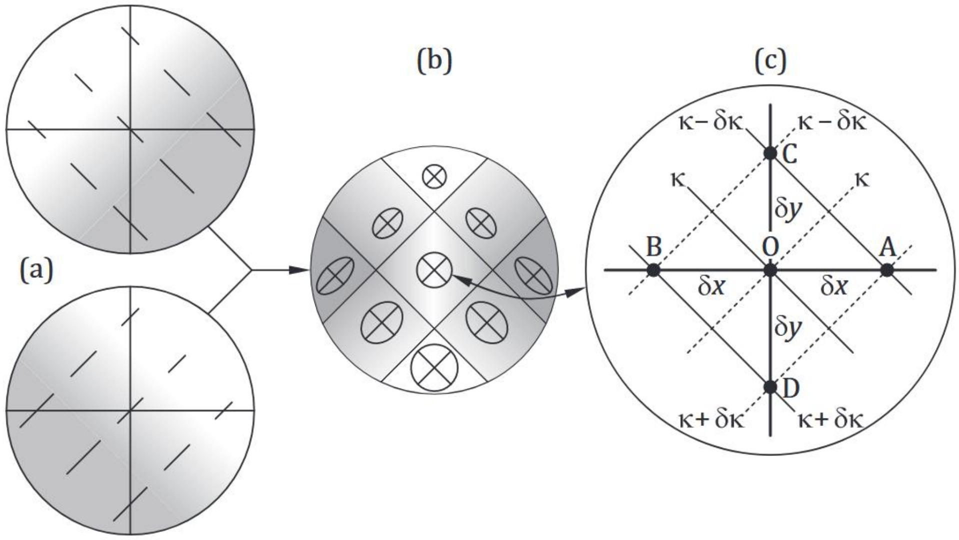

Figure 2.10 Progressive lens composed of two progressive cylinders with axis at 45° and 135°.

Winthrop in 1977 [76] described a lens design featuring a spherical distance portion occupying the entire upper half of the lens and a large spherical reading portion in the lower half. This design resulted in highly compressed astigmatism within the intermediate area, which was significant and non-negligible. While the design provided corrections for orthoscopy in the peripheral regions of the intermediate area, this introduced an undesirable concentration of aberration at the boundary between the corrected and uncorrected zones. The layout of this design resembled that of a trifocal lens, lacking visual continuity. In 1989 [77], Winthrop proposed a lens design incorporating a bipolar system of isopower contours. The progressive surface was generated by the curve of intersection between a sphere of variable radius and a corresponding circular cylinder of variable diameter. The relative dimensions and positions of the intersecting sphere and cylinder were carefully chosen to produce a gently curving surface, delivering a smooth optical effect. This innovative design approach is illustrated in Fig. 2.11. Such design technique minimizes the value of unwanted surface astigmatism by distributing it evenly over the entire lens area. The property of smoothness is achieved by ensuring that the mean square gradient of a specific auxiliary function, related to the mean surface power, remains within acceptable limits.

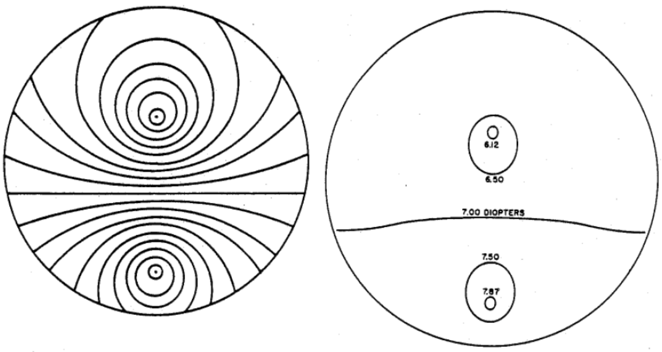

Figure 2.11 Designed surface by using bipolar design method proposed by Whinthrop [77].

In state-of-the-art freeform surface design techniques, the development of numerical methods for mathematical representation has been extensively researched, with B-splines and NURBS being commonly used for designing and modeling varifocal lenses [71] [78] [79]. Wei [39], in 2019, proposed a varifocal lens design method based on mathematical principles, which differs from traditional spline interpolation models by providing more accurate calculation data. Similar to previous methods, the designed surface is divided into three regions: the far-view zone at the upper area of the surface for user's distant vision, the near-view zone at the lower part for reading and near-sighted tasks, and a progressive corridor in the middle that smoothly connects the far and near zones, providing continuous vision. This design also includes a blending zone with inevitable astigmatism.

Wei's design technique involves first defining a meridian line to determine the vertex power distribution, then constructing the surface distribution accordingly. His method integrates toolpath generation for FTS and STS SPDT technology, providing a more stable tool nose radius compensation. This approach helps maintain a uniform federate along the X-axis, avoiding unnecessary acceleration and improving surface quality. Fig. 2.12 show the varifocal lens produced using Wei's method, along with its corresponding power distribution and astigmatism, respectively.

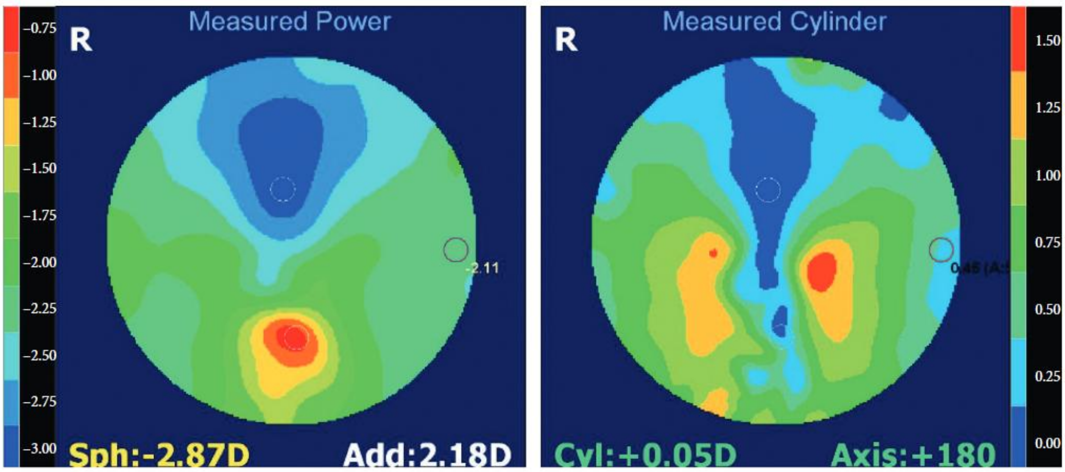

Figure 2.12 Power and astigmatism distribution of the lens [39].

Moreover, in the field of freeform surface optics, varifocal lenses have been extensively developed [131] [132] [133] [134]. The surface definition and design are recognized as critical steps, as they determine the optical surface's form based on the customer's prescription. To ensure the lens precisely fit for the customer, manufacturers use a fitting cross. The fitting cross is typically positioned 4 mm above the start of the progressive corridor and is intended to align directly in front of the wearer's pupil center, facilitating the measurement of prescription parameters. While the presentation of the fitting chart may vary slightly between manufacturers, the underlying measurement techniques are universally applicable to all designers or manufacturers of varifocal optics. This process is outlined in the flowchart shown in Fig. 2.14.

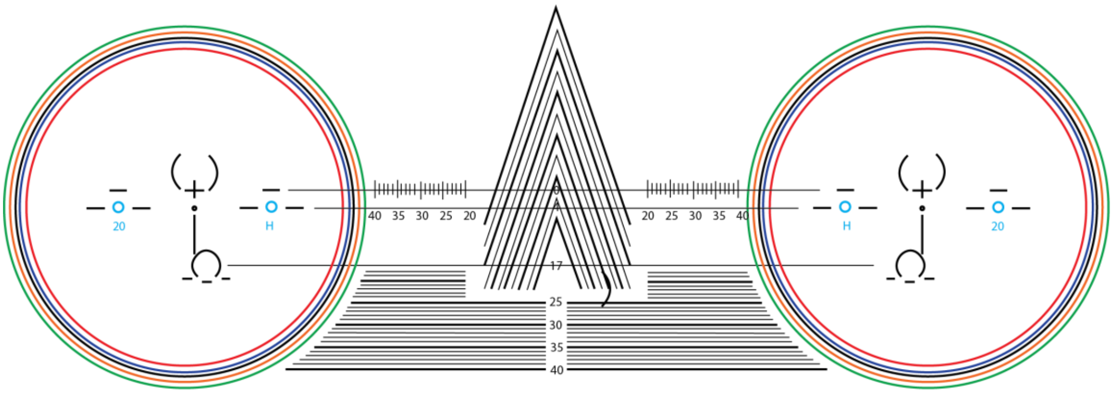

Figure 2.13 The manufacturer's centration chart allows for easy reading of the fitting cross height. When monocular interpupillary distance has not been previously measured with a pupillometer but were marked on the lenses, their distances maybe easily determined with the help of the horizontal cale on the chart.

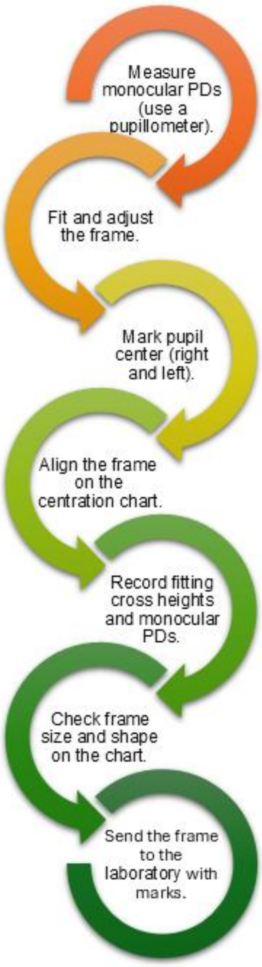

Figure 2.14 Flowchart of using the center chart and collecting the lens size and shape parameters of customer.

2.3.2 Lens surface modelling and representation

In terms of UPM manufacturing, similar to other CNC machines, two primary types of discrete representation can be used for freeform surfaces: the basic point cloud, which lacks surface connectivity information between points, and a faceted polygon mesh, constructed from the point cloud. Continuous models for freeform surfaces include techniques such as radial basis functions (RBF), B-splines, and NURBS. For “gentle” freeform geometries, particularly those used in optics, orthogonal polynomials or geometries modified by orthogonal polynomials are often employed [136]. These techniques accurately describe freeform surfaces using mathematical equations, enabling advanced mathematical operations on the surface. For UPM applications, continuous representation methods are generally the preferred choice for representing freeform surfaces in optical applications. However, deriving a mathematical description using B-splines, NURBS, or other methods is a non-trivial task. These methods are typically best suited for computer-generated surfaces with high symmetry and are less ideal for surfaces where metrological data is required for detailed analysis.

In some cases of freeform surfaced optics, the surface is defined by a series of calculation equations. By solving these equations, a basic point cloud can be generated. However, the basic point cloud provides limited information beyond serving as input for subsequent surface generation models [144]. As an alternative to polygon mesh representation, several methods are available to extract geometric information from a basic point cloud, with triangular meshes being the most widely used [145]. Delaunay triangulation is a common approach for creating a simple triangulated representation of points in a plane or a tetrahedral mesh for a 3D point cloud [146]. However, to generate a sheet or skin-like surface of triangles over a 3D point cloud, more advanced algorithms, such as alpha hulls or alpha shapes, are often required. Table 2.2 highlights the key advantages and disadvantages of point cloud and mesh representation models.

Table 2.2 The method of model representation and its advantages disadvantages respectively.

Representation models	Advantages	Disadvantages
Point cloud	Very simple	Provides no quantitaive desvription of the surface.
	Aquired by provided equations	Its is not possible to derive geometrical properties or quantities from a basic point set
	Low storage size compared with mesh	
Polygon mesh	Provides a topology	Requires complex algorithms to generate a mesh from the basic point set
	Mesh information can be used to calculate approximate geometeric quantites	When calculating certain geometric quantities, the mesh may also require
	Provides a pievewise linear interpolation of the surface as each polygon in the mesh is planar	Far higher storage size required to store the connectivity information between data points

Two main structures are commonly used to store facet information in face-based methods. The first structure represents facets by their vertex positions. However, this approach results in redundant vertices being repeated multiple times, as many facets share the same vertices. To address this inefficiency, the indexed face structure is used, where facets are represented by indices of vertices rather than by the vertices themselves. This structure is both simple and efficient, making it widely used in file formats such as STL, OFF, OBJ, and VRML. The STL file format, in particular, offers a straightforward data structure that stores not only vertices and facets but also facet normal vectors. The point cloud and mesh methods are easy to generate and have been extensively applied in the manufacturing of highly customized and complex freeform surfaces. However, due to the stringent quality requirements for freeform surface optics in terms of accurate shape representation and precise ray tracing performance, directly using point cloud or mesh models for surface description and machine toolpath generation may lead to surface defects during the material removal process.

To overcome these limitations, a reconstruction model is necessary for ultra-precision machining to ensure the adaptability and accuracy of freeform surface applications. In current state-of-the-art research on reconstruction methodologies, the most commonly used techniques include Bezier surfaces, B-splines, and Non-Uniform Rational B-Spline (NURBS) surfaces [137] [138] [139] [140]. Table 2.3 summarizes and compares the commonly used mathematical representation methods and their corresponding expressions as applied in the freeform surface industry.

Table 2.3 Mathematical expressions of common freeform surface shape types.

Surface shape	**Mathematical expression**
Toroid	$z = \frac{c_y y^2 + S(2 - c_y S)}{1 + \sqrt{(1 - c_y S)^2 - (c_y y)^2}}$, where $S = \frac{c_x x^2}{1 + \sqrt{1 - (1 + k_x) c_x^2 x^2}} + \sum_{i=-2}^{p} A_{2i} x^{2i}$
Anamorphic asphere	$z = \frac{c_x x^2 + c_y y^2}{1 + \sqrt{1 - (1 + k_x) c_x^2 x^2 - (1 + k_y) c_y^2 y^2}} + \sum_{i=-2}^{p} A_{2i} [(1 - B_{2i}) x^2 + (1 + B_{2i}) y^2]^i$.
XY polynomials surface	$z = \frac{c(x^2 + y^2)}{1 + \sqrt{1 - (1 + k) c^2 (x^2 + y^2)}} + \sum_{i=0}^{p} \sum_{j=0}^{p} A_{i,j} x^i y^j$, $1 \le i + j \le p$.
Q polynomials surface	$z = \frac{c(x^2 + y^2)}{1 + \sqrt{1 - (1 + k) c^2 (x^2 + y^2)}} + \sum_{j=1}^{p} C_j Z_j$, where Z_j is the j th Zernike term $z(\rho, \theta) = \frac{c\rho^2}{1 + \sqrt{1 - c^2 \rho^2}} + \frac{1}{\sqrt{1 - c^2 \rho^2}} \{u^2 (1 - u^2) \sum_{n=0}^{N} a_n Q_n^0 (u^2)\} + \sum_{m=1}^{M} u^m \sum_{m=1}^{M} [a_n^m \cos(m\theta) + b_n^m \sin(m\theta)] Q_n^m (u^2)$.
Radial basis function freeform surface	$z = \frac{c(x^2 + y^2)}{1 + \sqrt{1 - (1 + k) c^2 (x^2 + y^2)}} + \sum_{i=1}^{N} w_i \varphi(\lvert x - C_i \rvert)$
NURBS	$S(u, v) = \frac{\sum_{i=0}^{n} \sum_{j=0}^{m} N_{i,p}(u) N_{j,q}(v) w_{i,j} P_{i,j}}{\sum_{i=0}^{n} \sum_{j=0}^{m} N_{i,p}(u) N_{j,q}(v) w_{i,j}}$

(1) Bezier surface

The Bezier surface is one of the earliest methods to use a set of discrete control points to define a smooth, continuous curve through mathematical formulas. This method was introduced by Paul de Casteljau in 1959[80]. The Bezier surface is associated with several equations that describe its parametric properties:

$$\boldsymbol{B}(t) = \sum_{i=0}^{n} b_{i,n}(t)\boldsymbol{P_i}, \quad 0 \leq t \leq 1 \tag{2.6}$$

Where the polynomials b is Bernstein basis of degree n:

$$b_{i,n}(t) = \binom{n}{i} t^i (1-t)^{n-i}, \quad i = 0, \dots, n \tag{2.7}$$

$t^0 = 1, (1-t)^0 = 1,$ and the binomial coefficient, $\binom{n}{i}$ is:

$$\binom{n}{i} = \frac{n!}{i!\,(n-i)!}. \tag{2.8}$$

In this context, the points Pi represent the control points, and n denotes the total number of control points. The polygon formed by connecting the Bezier points with lines, starting from P0 and ending with Pn is known as the control polygon. The shape of the curve is influenced collectively by all the control points, including Pn. This means that any movement of a control point necessitates recalculation of the entire curve, resulting in global changes to its shape. Consequently, the Bezier curve lacks the ability for local control of the curve.

(2) B-spline surface

B-spline surfaces have proven to be highly effective for data fitting applications. Unlike Bezier curves, B-splines introduce additional parameters in their basis formula, allowing partial modifications to the surface without affecting the entire calculation of the curve. This flexibility makes B-splines particularly advantageous for complex surface modeling. The function for B-spline surface reconstruction is illustrated in the equations below, which share similarities with the Bezier curve:

$$S_{n,t}(x) = \sum_{i} \alpha_i B_{i,n}(x). \tag{2.9}$$

In which α_i is the vector of $(n+1)^{th}$, the control point is from 1 to n+1. $B_{i,n}$ is the basis function and can be derived by means of the Cox-de Boor recursion formula:

$$B_{i,0}(x) := \begin{cases} 1 \; if \; t_i \leq x \leq t_{i+1} \\ 0 \; otherwise \end{cases} \tag{2.10}$$

$$B_{i,k}(x) := \frac{x - t_i}{t_{i+k} - t_i} B_{i,k-1}(x) + \frac{t_{i+k+1} - x}{t_{i+k+1} - t_{i+1}} B_{i+1,k-1}(x). \tag{2.11}$$

The basis function $B_{i,0}(x)$ is piecewise constant, taking a value of either one or zero, depending on the knot span in which x lies. The primary advantage of B-splines, compared to Bezier curves discussed earlier, is their ability to modify only a localized section of the curve without requiring the recalculation of the entire curve.

(3) NURBS surface

NURBS were initially exclusive to proprietary CAD packages developed by car companies but later became a standard feature in computer graphics packages [81]. The use of NURBS surfaces offers greater flexibility in approximating complex forms. However, their highly nonlinear nature makes the fitting process significantly more complicated compared to B-spline surfaces, requiring the insertion of additional knots and control points until a satisfactory error norm is achieved. These operations become particularly challenging for complex surfaces. By reconstructing a NURBS surface, a computable and analyzable representation of a freeform surface is obtained, enhancing precision and performance in the machining process. Freeform surfaces can be reconstructed by applying NURBS global interpolation to $(n+1) \times (m+1)$ discrete data points, $\{Q_{k,l}\}$. The NURBS surface of $(p,q) - th$ order is expressed by the following equation:

$$Q_{k,l} = S(u,v) = \frac{\sum_{k=0}^{n} \sum_{l=0}^{m} N_{k,p}(u) N_{l,q}(v) w_{k,l} Q_{k,l}}{\sum_{k=0}^{n} \sum_{l=0}^{m} N_{k,p}(u) N_{l,q}(v) w_{k,l}} \tag{2.12}$$

NURBS is referred to as a rational curve because its equation includes a fraction. It shares the same basis equation as B-splines but introduces an additional parameter, W_{kl}, which controls the **local taper** of the curve, adding flexibility to the surface. In the NURBS surface equation, W_{kl} represents the weight of each control point. The parameters u and v correspond to the parameter values of the discrete data points $Q_{k,l}$. The terms $N_{k,p}(u)$ and $N_{l,q}(v)$ represent the p-order and q-order B-spline basis functions, respectively, which are defined over the non-uniform knot vectors U and V.

2.4 Assessment of FSO

2.4.1 Investigation of FSO surface topography characteristics

In the process of UPM, surface topography is formed through the interaction between the tool profile and the workpiece. It is primarily influenced by the relative motion between the tool and the workpiece, as well as the material removal mechanisms, including material deformation and separation. As a result, surface topography serves as an accurate representation of the cutting process and material removal dynamics, reflecting the behavior of the material during cutting. Furthermore, it captures the imprint of all static and dynamic factors involved in the cutting process.

As it has been illustrated in Fig.2.15, a resulting surface topography produced by UPM is characterized by tool mark, material swelling and recovery, vibration induced wavy. Material pile-up, and material crack/surface wrinkle/fracture/defect/dimple [82]. In state-of-art research of surface characteristic has been conducted to study cutting mechanism. Since in 1964 Sata proposed the existence of material swelling [83], the research of material recovery and swelling in SPDT UPM process has been widely studied with depth [84], [85] The crystallographic orientation of the material induce the variation in elastic recovery and plastic deformation of the surface and furtherly leads to the formation of a wavy surface. Lee et al. in 1999 reported an observation of a wavy surface through straight cutting test as shown in Fig.2.16(a) [86]. Later, as shown in Fig.2.16(b), Cheung in 2002 [87] observed that the pits and cracks formed at the surface of AL661/15SiCp in UPM which were induced by the hard SiC reinforcement. In 2006, Simoneau et al.[88] proposed that surface micro-defects, illustrates dimples occurring at a hard-soft grain boundary, influenced surface roughness during micro-scale cutting. Liu and Melkote [89] presented that material pile-up was one key physical factor in influencing nanometric surface roughness formation. Zhang et al. in 2013 [90] investigated the influence of spindle vibration on surface topography in UPM. The researches referenced above illustrates the special surface topography characteristics are formed by the relative motion and material removal mechanism.

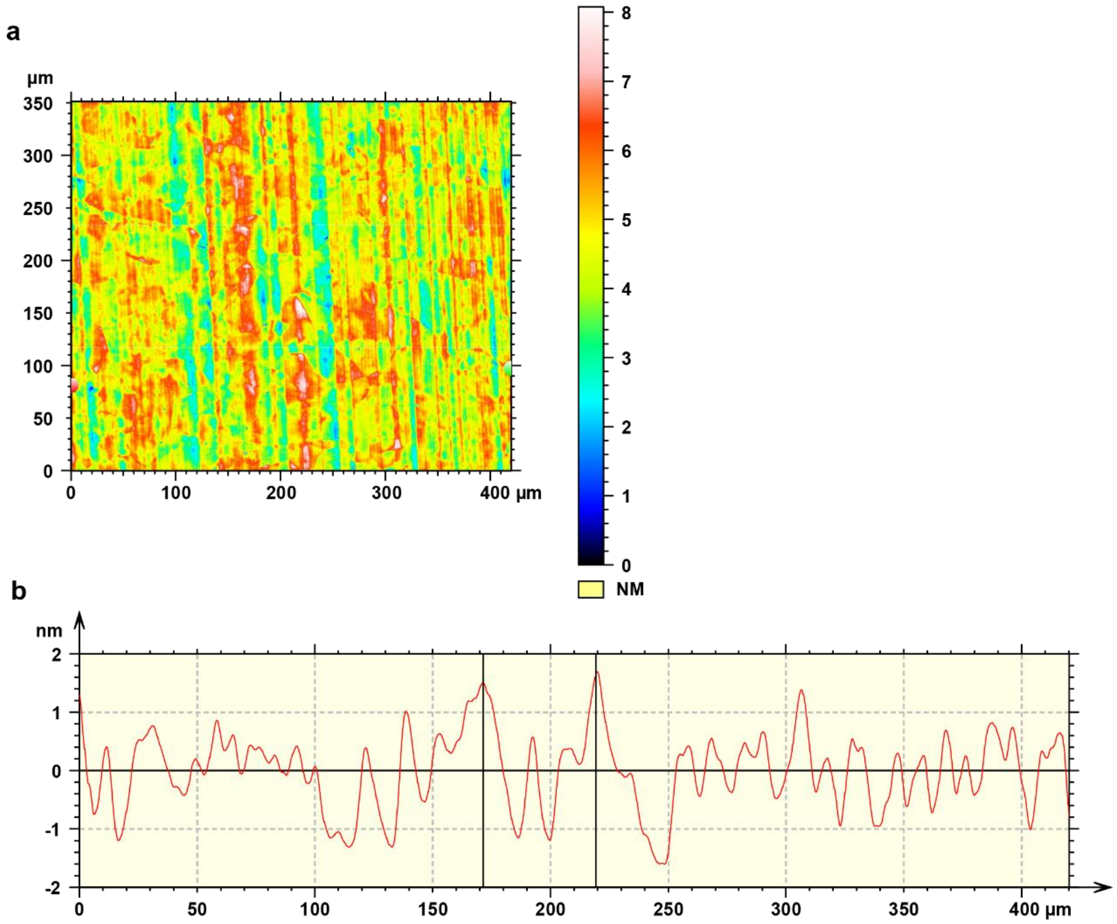

Figure 2.15 Ultraprecision machined surface observed by Polytec TopMap Micro.View white light interferometer (20x measurement): a) surface topography plot; b) horizontal profile data of the machined surface topography.

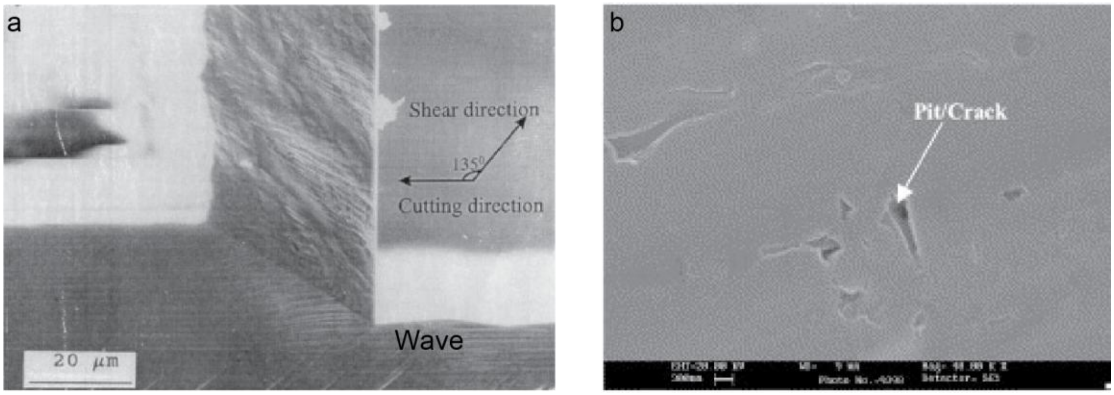

Figure 2.16 a) Micrograph (SEM) of straight cutting force single crystal copper [86]; b) SEM micrograph of the machined surface of Al/SiC metal matric composites [87].

Free-form analytics or characterization follows the spirit of the standardized GPS verification characterization as contained in the ISO GPS documents, in that the free-form surface is decomposed into form, shape, and texture parameters [91]. These parameters can then be compared with the freeform specification for conformance. The characterization of the form is carried out on the unaltered mesh. The characterization of the shape and texture parameters is carried out on the residual vector field after the form has been removed. The difference between shape and texture is that, for the shape vector field, the residual surface has only a lower limit in scale Lc, whereas the texture vector field has both upper and lower limits in scale Uc and Lc, respectively. Currently, it is very common that Lc and Uc have the same scale value. However, for some modern manufacturing processes such as additive manufacturing, further decomposition of the shape and texture vector fields can yield useful analytics for control of the manufacturing processes or functional prediction, with each individual decomposition having its own set of characterization parameters.

In this study, shape parameters have been used to analysis the surface. Shape parameters are associated with geometrical tolerance in that they characterize the deviation from nominal from through the shapes residual surface. Again, following the spirt of standardized GPS documents, there are four different type of shape parameters based on the following deviations:

a) peak-to-valley deviation: value of the largest positive local deviation added to the absolute value of the largest negative local deviation,
b) peak-to-reference surface deviation: value of the largest positive local deviation,
c) valley-to-reference surface deviation: value of the largest negative local deviation, and
d) root-mean-square deviation: square root of the sum of the squares of the local deviations from the least squares reference surface.

Where the reference surface is the associated freeform surface, the reference freeform surface is the surface from which deviations from free form are referred. The deviation is negative if from the reference surface the point lies in the direction of the material and is normal to the local reference surface. Mathematics for calculation is the same as for the surface texture field parameters given in the next section.

Moreover, surface texture feature parameters are derived from a segmented freeform surface. The choice of the scalar function of the segmentation algorithm depends on specific applications. Thay can be surface height normal to the local reference surface, surface gradient, surface curvature, or any other value of interest. Three dimensional parameters of the surface texture are calculated on the basis of autocorrelation analysis of the surface texture. Autocorrelation analysis allows regular surfaces to be distinguished from chaotic surfaces and permits evaluation of their properties.

Sal the one of the main 3D parameters of the surface texture which is the length corresponding to maximum decay of the autocorrelation function. Sal characterized the shortest horizontal distance for which decay of the autocorrelation function to 0.2 is observed over all possible directions:

$$Sal = \min\left(\sqrt{\tau_x^2 + \tau_y^2}\right)\backslash big|_{ACF(\tau_x,\tau_y)\le 0.2} \tag{2.13}$$

This minimum is observed perpendicular to the machining tracks. Higher Sal corresponds to a surface with a dominant long wave (low frequency) component, and small Sal to a surface with dominant short wave (high frequency) component. The parameter Surface Texture aspect Ratio (Str) of the surface texture indicates how isotropic the surface is. It is defined as the ratio of the characteristic length and characteristic width of the textural elements:

$$Str = \frac{min\left(\sqrt{\tau_x^2 + \tau_y^2}\right)\Big|_{ACF(\tau_x,\tau_y)\le 0.2}}{max\left(\sqrt{\tau_x^2 + \tau_y^2}\right)\Big|_{ACF(\tau_x,\tau_y)\le 0.2}} \tag{2.14}$$

When Str close to 1, the surface is isotropic. With decrease in Str, the surface becomes more anisotropic.

2.4.2 FSO optical performance assessment

In the 1980s, the rapid development of Computer-Aided Design (CAD), Computer-Aided Manufacturing (CAM), and computer graphics significantly advanced the study of ray tracing for freeform surfaces. The most complex aspect of ray tracing for freeform surfaces is solving the intersection points between rays and surfaces, which accounts for approximately 99% of the total computational workload in ray tracing. Whitted in 1980 proposed a surface subdivision method to intersect points between rays and parametric surfaces [92]. This method simplifies complex surfaces by recursively subdividing the parametric surface within the ray's orthogonal view coordinate system. The subdivision continues until each fragment becomes simple enough to efficiently compute the ray-surface intersection. By reducing the complexity of directly calculating intersections in object space, this approach significantly accelerates the ray tracing process. Kajiya in 1982 [93] proposed a method representing geometric surfaces as algebraic equations. By determining the interaction points between light and the surface, solving the intersection of light parameterization equations with these algebraic equations. This method offers high accuracy and versatility, making it suitable for complex implicit surfaces and global illumination calculations. Toth [94] presented a method in 1985 for ray tracing parametric surfaces using multivariate Newton iteration to solve the ray surface intersection. Which provides enough generality to render surfaces which could not be ray-traced using existing methods. In 1986, Kenneth and Murthy proposed an algorithm for ray tracing parametric surface patches. The algorithm is created based on the theory that during the calculation of ray/surface intersections, in most scenes, groups of rays follow nearly the same path from the eye, striking the same objects as it shown in Fig.2.18. the probability is high that two adjoining rays coming from the eyepoint will strike the same surface, and will intersect the surface in the same general area. The method employs quasi-Newton iteration to solve ray/surface intersections and leverages ray-to-ray coherence by using numerical information from adjacent rays as initial approximations for the quasi-Newton algorithm. To ensure convergence to the correct intersection point, object space subdivision techniques are applied [95].

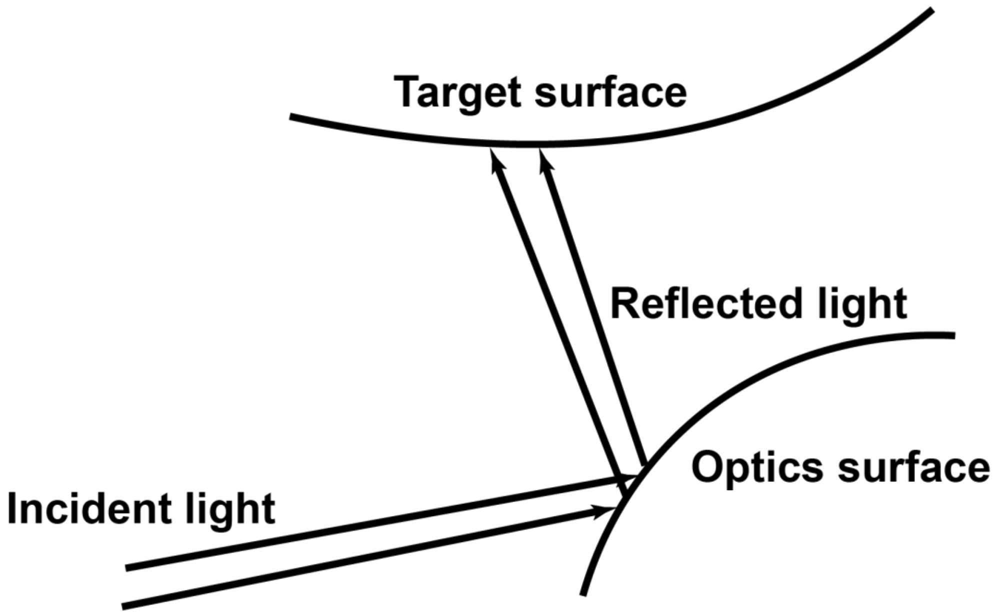

Figure 2.17 Method of ray coherence.

The Bezier clipping approach for curve intersection was introduced by Sederberg and Nishita in 1990 [96]. This technique underpins algorithms for determining the intersection points of two curves and for efficiently and robustly computing points of tangency between them. The method leverages the convex hull property of Bezier curves to identify regions of the curves that do not contain solutions. By iteratively clipping away these regions, the algorithm converges to the solution at a quadratic rate while ensuring robustness and reliability. In 1993, Barth and Sturzlinger proposed an algorithm that performs ray tracing calculation for Bezier and B-spline efficiently[97]. In 1994, and Buchanan proposed and demonstrated the use of Chebyshev basis functions to accelerate the computation of intersections between rays and parametric curves or surfaces [98]. The characteristics of Chebyshev polynomials enable the calculation of more accurate and tighter bounding boxes. These tighter bounds provide surfaces with an improved termination criterion for determining subdivision limits. Martin, Cohen, and Fish in 2000 proposed a system for ray tracing trimmed NURBS surfaces, combining various existing methods of the time [99]. Their approach involved creating a set of bounding boxes that encapsulated the surface over specific parametric ranges. Rays intersecting with these boxes were identified, and a parametric value within the intersected box was used to initialize root-finding algorithms. The proposed algorithm efficiently calculated the positions of intersection boxes and the corresponding root values. Subsequently, an evaluation algorithm has been employed to evaluate the geometry of the surface.

2.4.3 Cutting force model for FSO

Cutting force analysis is essential for improving and optimizing a certain machining process. It provides critical insights into tool design, optimal process parameters, and the machinability of various materials [100], [101]. As one of the most advanced machining technologies, UPM, which can exact components, significantly impacts solving the demand problem. UPM is defined as achieving machining form accuracy of less than 0.01 μm [82]. As the surface quality and machining cost can be improved via machining optimization process, cutting force modelling that close relate to the machining quality and efficiency is becoming critical [102]. Thus, cutting force generation, which highly depends on the microstructure of composite material, reinforcement properties and their interfacial reaction [103], plays a significant role. It is expected to reflect most of micro machining phenomenon collectively including size effect, chip formation, cutting temperature and tool wear status, and also has potential to optimize the machining conditions and cutting tool conditions.

The prediction of cutting force has been research in a wide range, the difficulty of the cutting force prediction is its requires comprehensively consideration of the numbers of factors that are involved in the machining process [104], in the case of UPM process, such factors including tool deflection, material, chip thickness, Depth of Cut, etc. Cutting force prediction should be highly related to the current machining process. Therefore, for the application of UPM on FSO, the dynamic cutting force models based on theoretical assumptions and experimental observations have been developed or improved. Table 2.4 lists a number of significance researches on SPDT cutting force modelling and its characteristics respectively.

Table 2.4 Cutting force models for diamond turning and micro cutting as developed in recent years.

Methodology	Author(s)	Cutting force modelling	Characteristics	Methodology analysis
Experiment-based model	Lee	Micro-plasticity model	Predicting the pattern of cyclic variations of cutting forces in diamond face turning	Power spectrum analysis
	Moriwaki	Cutting force model	Establishing the relationship between principal cutting force and thrust force, varied with a small depth of cuts	Experimental measurement data discussions
	Drescher and Dow	A quantitative model relationship between the tool cutting edge sharpness and cutting forces	Predicting the diamond tool cutting edge condition from cutting forces during a turning operation	
	Scheffer and Heyns	Time-series model coefficients (based on data collection of three directions' signals: X-feed force, Y-thrust force, and Z-acceleration signal)	TCM	Correlation coefficient approach (based on WPD analysis) and the SOM

	Fang et al.	Correlation of tool cutting edges wear with the cutting forces and vibration model	Detecting the tool wear on cutting edges	Wavelet packet transform
	Dornfeld	Multilayered perceptron-type neural network model (based on raw signal from the AE, force, and the current sensors)	Online tool wear monitoring system	Multichannel AR and artificial neural networks
Numerical based (finite element analysis) model	Lo-A-Foe et al.	The force relationship numerical model	Estimating the surface roughness of SPDT	Cutting experiments to evaluate the model
	Carroll and Strenkowskl	FE-based cutting process model	Determining the detailed stress and strain fields, chip formation and geometry, and cutting forces	Lagrangian model and Eulerian model (based on FEA)
	Ravindra et al.	Mathematical models, focusing on wear time and wear force relationships	Estimating the progressive tool wear and cutting force relationships	Multiple regression analysis and cutting experiment validation
Mechanics-based model	Kim and Kim	Two orthogonal micro cutting models and their comparison (based on cutting force and thrust force)	Determining two factors (elastic recovery and tool cutting edge radius) which have effect on micro cutting.	Comparison between the simulation results and experimental results, including cutting/thrust force per unit contact length (N/mm) and specific cutting/thrust force per unit cutting area (N/mm2)

2.4.4 Atkins cutting force model

The consideration of dissipation by the plastic deformation in the shear zone, friction on the chip-knife interface and crack propagation ahead of the knife. Based on these assumptions, the energy balance equation during sectioning was given by Atkins. As it has been illustrating in the Fig.2.18, the model of Atkins demonstrates that during the formation of the chip, metal cutting is from the class of ductile fracture problems where there is complete plastic collapse. This idea has been used in UPM for freeform surface. The cutting force model developed in this study is grounded in Atkins' model [105]. Simultaneously, we consider the direction of the cutting force and the practical DoC. In instances where surface work plays a substantial role in steady deformation, several internal works are identified: (i) plasticity along the practical shear plane; (ii) friction along the underside of the chip at the tool interface; and (iii) formation of a new cut surface [105]. All these work components are externally provided by the FC component of the tool force moving along the machined surface's toolpath file.

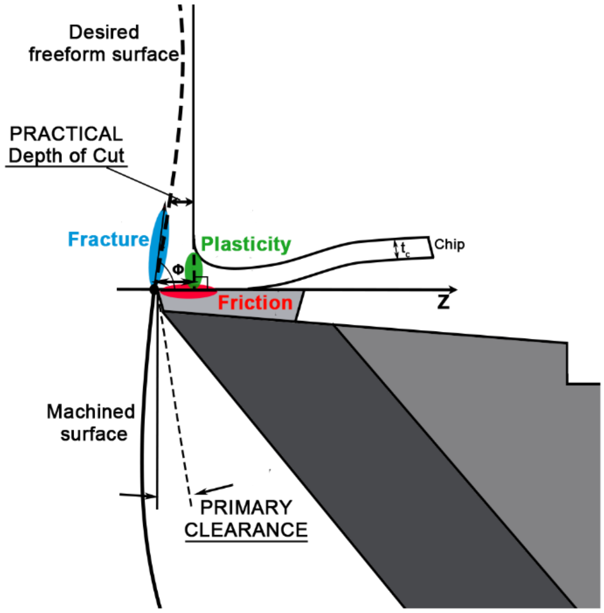

Figure 2.18 Schematic of the nano-sectioning by STS ultraprecision machining process.

With the help of Atkins' model, the overall main cutting force can be obtained as follows:

$$F_c V = (\tau_y \gamma)(t_0 w V) + [F_c \sec(\beta - \alpha) \sin \beta] \frac{V \sin \phi}{\cos(\phi - \alpha)} + RwV \tag{2.15}$$

where V is the cutting velocity, F_c is the horizontal component of the cutting force, τ_y is the (rigid-plastic) shear yield stress, γ is the shear strain along the shear plane, given by $\gamma = cot\varphi + \tan(\varphi - \alpha) = cos\alpha/\cos{(\varphi - \alpha)}sin\varphi$; t0 is the uncut chip thickness, w is the width of the orthogonal cut, φ is the orientation of the shear plane and R is the specific work of surface formation (fracture toughness). More details of the Akins model as its improvement method has been illustrates afterward in Chapter 3.

2.5 Summary

In this chapter, the state-of-the-art research on ultra-precision machining of freeform surface optics is critically reviewed, and the following research gaps are identified:

1. **Integration of Design, Modeling, and Machining**: While the design and modeling of FSOs have been extensively studied for decades, with methods diversifying significantly, advancements in micro-cutting and UPM have driven the widespread application of UPM for FSO manufacturing since the 2000s. However, very limited research has integrated freeform surface design and modeling with considerations for the machining process. Developing an integrated approach that incorporates FSO design and modeling with UPM considerations is crucial for advancing the freeform surface manufacturing industry.

2. **Dynamic Cutting Force Prediction**: Cutting force prediction models have evolved alongside advancements in CAD, CAM, and CNC machine manufacturing. Although cutting force modeling is well-established in traditional machining processes and SPDT

UPM, freeform surface manufacturing presents new challenges. The constant variation in surface curvature along the cutting toolpath influences practical cutting parameters such as cutting direction, shear angle, depth of cut, and cutting force. Investigating the dynamic cutting forces in UPM for FSO is essential to address these challenges.

3. **Analysis of Toolpath and Surface Residuals**: UPM is renowned for its high precision and accuracy, often referred to as "deterministic manufacturing." Unlike traditional machining, which typically requires additional polishing, the surfaces produced by UPM are the final surfaces. Consequently, the machining toolpath remains on the resulting surface and can be evaluated using advanced observation equipment. Investigating these residual toolpaths is critical for retracing and simulating the machining process, providing valuable insights for process optimization and validation.

Chapter 3

Development of the NURBS-based integrated approach for design and ultraprecision manufacturing of freeform surfaces

3.1 Introduction

In the previous chapter, the literature review discussed the current understanding of ultra-precision machining for freeform optical surfaces, which differs significantly from the machining of uniformly planar surfaces such as spherical optics or traditional lenses. Due to the complex geometry and high-quality requirements of freeform surfaces, their design and modeling are typically performed in a digital environment. The manufacturing of such surface is commonly executed using a multi-axis single-point diamond turning machining process, capable of achieving surface roughness of less than 1 nm. However, high costs, stringent quality assurance requirements, and long machining times are inevitable challenges in the SPDT machining process. Therefore, an innovative virtual lens model approach for ultra-precision production is being investigated to optimize efficiency, reduce costs, and improve overall process reliability.

In this chapter, an integrated approach for constructing a virtual lens model has been presented, aimed at achieving high responsiveness in freeform surface manufacturing, while considering surface design modeling and ultra-precision machining. The primary focus of this research is to develop a lens model within a digital environment, utilizing the NURBS modeling approach, ultra-precision machining processes, ray tracing simulation, dynamic cutting force modeling, and high-precision surface topography assessment. This integrated approach ensures that the lens model can accurately represent the quality of the resulting machined surface.

3.2 Framework of the integrated approach

The critical aspect of industrial scale challenges in ultraprecision machining of freeform surface is surface design and modelling. The design and modeling process constitutes a critical component of the freeform surfaced optics manufacturing process, owing to its requisite integration of two distinct design-driven methodologies: optical design-driven and enabled manufacturing-driven approaches. As it shown in Figure 3.1, the optical design-driven approach stands as the initial phase wherein a surface designer receives the requisite surface function specifications from the customer. Subsequently, the designer proceeds to generate an optical design surface tailored to meet the specific optical requirements delineated, customer requirement, surface optical performance, material selection and its reflective index are all consider in this part. Subsequently, the designed surface is translated into a surface Computer-Aided Design model following the approach of enabled manufacturing-driven, include considering, facilitating comprehension by Computer Numerical Control (CNC) machining systems for production purposes, the generated toolpath, tool wear set, machining process are considered in this step. After that, A digital assessment to the defined surface model is applied to have batter understanding and accuracy predict the result quality of the machined optics surface.

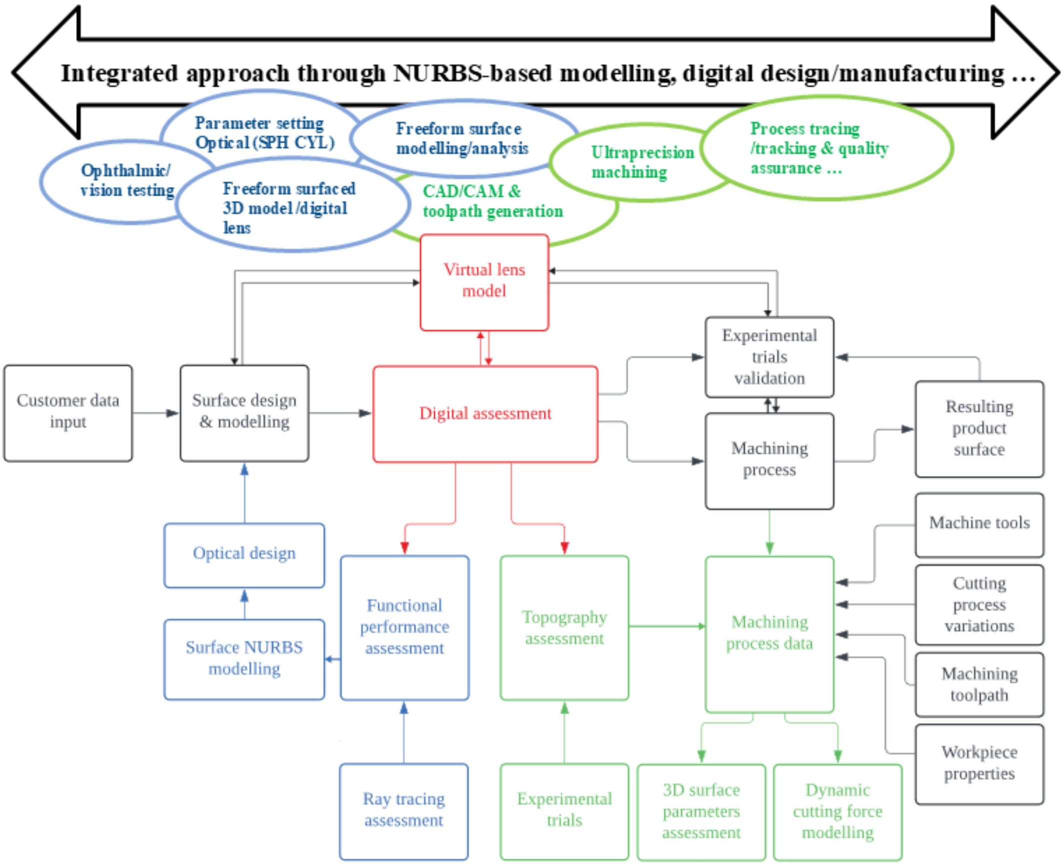

Figure 3.1 Framework of the integrated approach to design, manufacturing and virtual assessment of freeform lenses in industrial scale ultraprecision production.

The virtual lens model approach shown as red part in Figure 3.1 is applied right before the constructed model been carried out by the machining process and deduce the resulting surface. The reason of set virtual lens model between the surface design modelling and ultraprecision machining process is to enhance the understanding of defined freeform surface and accurate predict the geometry and the optical performance of the resulting surface. To makes the virtual lens model contains both optical and topography information of the machined freeform surface optics and can highly represent the quality result of the surface optics. To achieve that, digital assessment

3.3 Freeform surface design and its NURBS-based modelling

In state-of-the-art design methodologies for freeform surface applications, each type of optical application typically adopts one or more specialized design approaches tailored to achieve its specific functional objectives. To ensure that our method is broadly applicable across various optical applications while minimizing potential losses in surface form and curvature accuracy, a surface reconstruction approach has been adopted. Our process begins with designing a freeform surface using the appropriate method for the application optics. Next, a NURBS model is constructed based on the designed surface, enabling accurate and flexible surface representation for further assessment, simulation and toolpath generation.

In the case of designing a freeform surface of varifocal lenses, a varifocal lens can meet the need for clear vision at both far and near distances, providing a continuous field of view and offering a more comfortable wearing experience. In this regard, as shown in Fig.3.3, four different zones are considered, as follows: zone A is for distant vision; zone C is for near vision and reading; zone B is the progressive corridor connecting far and near zones, providing smooth continuous vision that is also the design's main focus; and zone D is the peripheral zone, where astigmatism is inevitable [147].

Any point at the meridian line is called $Q(u, 0, z)$. Additionally, any $q(\varepsilon, \eta, \zeta)$ point is known as the curvature centre of Q. In this regard, $r = Qq$ is the curvature radius of point Q. Equation (1) represents the Dirichlet integral, in which m and l are, respectively, the first-order terms, ensuring that $\frac{d^n D(x,0)}{dx^n}$ is not zero at the distant and near views.

$$\int_F^N \left| \frac{d^{m+l-1}\, D(x,0)}{dx^{m+l-1}} \right|^2 dx \tag{3.1}$$

To ensure that the transition is smooth at the far- and near-vision zones, the order of the first nonzero derivative should be high. Based on the Euler–Lagrange equation and boundary conditions, Equations (3.2) and (3.3) are obtained as follows:

$$D(x, 0) = DD + (DR - DD) \sum_{i=1}^{m+l-1} c_i (x + L)^i \tag{3.2}$$

$$\sum_{i=1}^{m+l-1} c_i h^i = 1 \tag{3.3}$$

The vertex power of the surface has been calculated by Equations (3.1) to (3.3), by entering the corresponding parameters for l, m, h, and L, and knowing the definitions of Q, q, and r, the curvature radius at any point on the front surface of the lens is calculated as shown in Equation (3.4):

$$\frac{1}{r(u)} = \frac{1}{rD} + \left(\frac{1}{rR} - \frac{1}{rD}\right) \sum_{i=m}^{m+l-1} c_i (u + L)^i \tag{3.4}$$

A freeform optical surface can be derived by selecting an appropriate contour function u(x, y) and substituting it into the relevant governing equations. In the next step, the designed freeform surface is converted into a NURBS model through a fitting approach.

In most applications of ultra-precision machining, SPDT is commonly used to process simple optical mirrors. However, for complex freeform surfaces, especially those with non-rotational symmetries, effective spiral toolpath generation methods have yet to be fully developed.

Freeform surface technology is becoming increasingly popular in advanced production, particularly in optical applications such as HUD systems, varifocal lenses, and parabolic mirrors used in optical systems. These applications drive the need for extensive use of computer-aided design technology in ultra-precision machining. In many cases, pre-defined freeform surfaces are initially provided by customers, and these surfaces must be transferred between various CNC software systems for design, modeling, toolpath generation, and final manufacturing. This process can result in quality loss, particularly in the shape and curvature of the surface. To address this, a toolpath planning method based on the curvature of NURBS surfaces is proposed for ultra-precision slow tool servo SPDT machining. A detailed examination of the differential geometric characteristics of freeform surfaces is crucial in this context.

NURBS has emerged as the standard for representing surfaces in CAD due to its ability to model both analytical and organic surfaces while maintaining numerical stability. In this research, the NURBS approach is the fundamental method that integrated all the process of freeform surface manufacturing, from design modelling, digital assessment, and toolpath generation. By reconstructing a NURBS surface, a computable and analyzable expression of the freeform surface is obtained, enhancing precision and performance in the machining process. Freeform surfaces can be reconstructed by applying NURBS global interpolation to $(n+1)\times(m+1)$ discrete data points $\{Q_{i,j}\}$. The NURBS surface of (p,q)-th order is expressed by the following equation:

$$Q_{i,j} = S(u,v) = \frac{\sum_{i=0}^{n}\sum_{j=0}^{m} N_{i,p}(u)N_{j,q}(v)w_{i,j}B_{i,j}}{\sum_{i=0}^{n}\sum_{j=0}^{m} N_{i,p}(u)N_{j,q}(v)w_{i,j}} \tag{3.5}$$

Where $w_{k,l}$ represents the control point. U and v denote the parameter values of the discrete data point $\{Q_{k,l}\}$ respectively. Furthermore, to determine the value of the non-zero basis functions $N_{i,p}(u)$ and $N_{j,q}(v)$ in diverse node intervals, the calue of $N_{i,p}$ can be obtained through the interative calculation of Equations (3.8) and (3.9). Similarly, the solution process for $N_{j,q}$ can be completed using a comparable method.

$$U = \{0,\dots,0,u_{p+1},\dots,u_{n-p-1},1,\dots,1\} \tag{3.6}$$

$$V = \{0,\dots,0,v_{q+1},\dots,v_{m-q-1},1,\dots,1\} \tag{3.7}$$

$$N_{i,p}(u) = \begin{cases} 1, u_i \le u \le u_{i+1} \\ 0, other \end{cases} \tag{3.8}$$

$$N_{i,p}(u) = \frac{u-u_i}{u_{i+p}-u_i}N_{i,p-1}(u) + \frac{u_{i+p+1}-u}{u_{i+p+1}-u_{i+1}}N_{i+p+1,p-1}(u) \tag{3.9}$$

3.4 Freeform surface assessment in digital environment

The digital assessment of freeform surfaces is divided into two parts: functional performance prediction and surface topography evaluation, both aimed at understanding the correlation between surface manufacturing and customer utility. To predict the optical performance of the surface, we propose a ray tracing simulation method, which simulates the designed surface in a pre-defined environment that closely matches customer requirements, providing an intuitive illustration of the surface's optical performance.

In addition to ray tracing assessment, the freeform surface is reconstructed to obtain its mathematical expression. This allows for the analysis of differential geometric properties using 3D surface parameters and the prediction of cutting forces in a digital environment. Once both the surface geometric properties and optical performance have been evaluated and verified, we can confidently conclude that the surface quality has been demonstrated in a digital setting. We refer to the model that contains all the information from these assessments as the "virtual optics”.

3.4.1 Ray tracing and its simulations

The optical performance of the designed freeform surface can be analyzed using the ray tracing method in COMSOL Multiphysics. Ray tracing models are a computational tool for modeling the propagation of light and other electromagnetic radiation with a ray tracing approach. The rays can propagate through the model geometry while being reflected, refracted, or absorbed at boundaries which have been widely applied across various designs, particularly in complex optical systems. These models help optimize the design of freeform surfaces using a range of different methods. To simulate ray propagate it is crucial to establish the relationship between the surface design and its intended customer use. The simulation not only calculates the focal length of the optics but also generates a scatter plot, providing an intuitive visualization of the refractive power as rays pass through the designed surface. Once the design and material selection of the surface have been finalized and inputted, various position-of-wear parameters must be considered during ray tracing simulation. These parameters include vertex distance, pantoscopic tilt, face-form wrap, and the customer’s preferred viewing distance. Often, these parameters are pre-defined and can be traced back to the optics design process. By assuming a "position of use" which represents the intended position of the fitted optics relative to the user's visual system the surface design can be further optimized based on the simulation results. Fig.3.2 illustrates the process of generating a freeform varifocal lens surface in COMSOL Multiphysics. The initial imported dataset comprises a point cloud containing only curvature distribution and surface topography information. By integrating this data into a concave surface structure and combining it with a lens model that features a convex side with no optical power and together with the definition of the material selection, a fully designed freeform optical surface is constructed. This surface is then prepared for subsequent raytracing assessment.

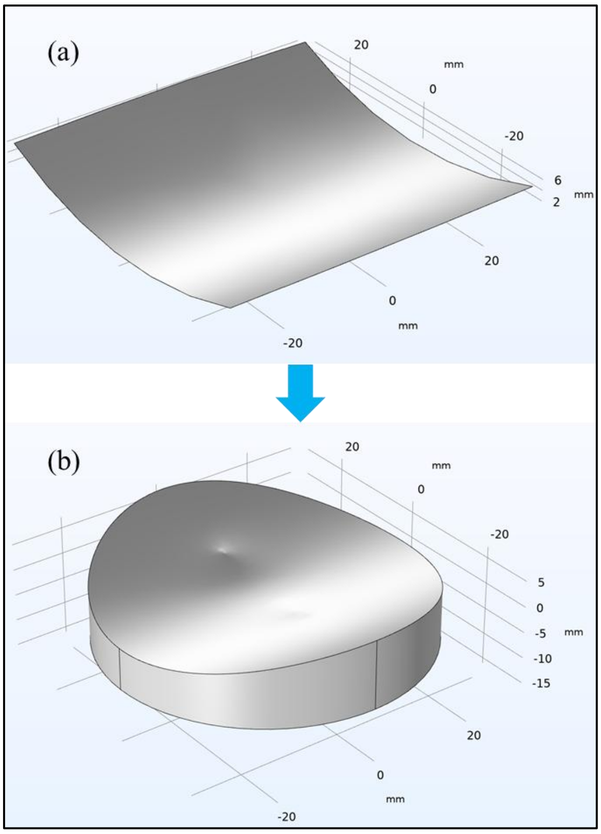

Figure 3.2 a) Lens's 3D freeform surface created in COMSOL Multiphysics 6.2, with a .xlsx format of the data point cloud exported from the Shiny web portal, b) 3D design of the varifocal lens.

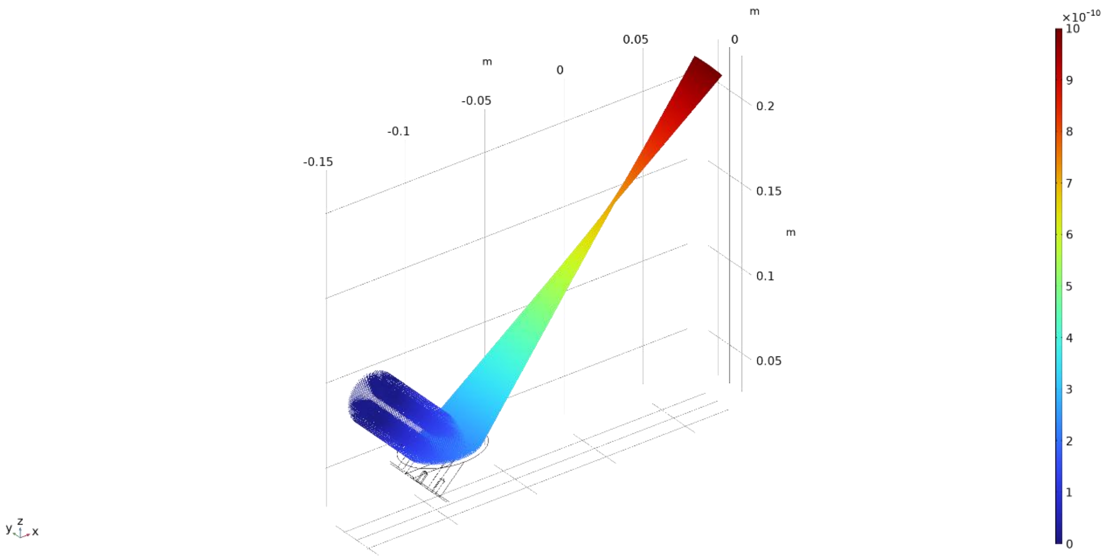

Figure 3.3 Simulation of an off-axis parabolic mirror raytracing simulation.

(1) Ray-surface intersection calculations

As it illustrates in Fig.3.2, the released and direction of ray can be defined in the simulation, and different boundary conditions to every surface in the geometry can be assigned according to application of the designed surface. Ray propagation is controlled by the refractive index of the medium. This affects the speed at which rays propagate through the domain,

$$\text{Speed of light} = \frac{\text{Speed of light in vacuum}}{\text{Refractive index}} = \frac{299{,}792{,}458\ \mathrm{m/s}}{n} \tag{3.10}$$

Whenever a ray reaches a boundary between two media with different refractive indices, the deterministic ray splitting algorithm generates a refracted ray and a specularly reflected ray. The direction of the refracted ray is computed using Snell's law,

$$n_1 \sin\theta_i = n_2 \sin\theta_t \tag{3.11}$$

where n is the refractive index, θ_i is the angle of incidence with respect to the surface normal, θ_t is the angle of the refracted ray, and the subscripts 1 and 2 indicate the side of the incident and refracted ray, respectively. The ray splitting algorithm automatically also detects when rays undergo total internal reflection and suppresses the release of refracted rays accordingly. Moreover, ray polarization is vital even to the simplest model of reflection and refraction at a material discontinuity. The coefficients of reflection and refraction depend on whether the incident ray is polarized in the plane of incidence (p-polarized) or perpendicular to it (s-polarized). This dependence is shown explicitly in the Fresnel equations,

$$t_p = \frac{2n_1 \cos\theta_i}{n_2 \cos\theta_i + n_1 \cos\theta_t} \tag{3.12}$$

$$t_s = \frac{n_1 \cos\theta_i + n_2 \cos\theta_t}{n_1 \cos\theta_i + n_2 \cos\theta_t} \tag{3.13}$$

$$r_p = \frac{n_2 \cos\theta_i - n_1 \cos\theta_t}{n_2 \cos\theta_i + n_1 \cos\theta_t} \tag{3.14}$$

$$r_s = \frac{n_1 \cos\theta_i - n_2 \cos\theta_t}{n_1 \cos\theta_i + n_2 \cos\theta_t} \tag{3.15}$$

The subscripts p and s refer to polarization in the plane of incidence and orthogonal to it, respectively; that is, p- and s-polarization.

The above procedure explains the equations of ray trace simulation model in COMSOL. Also, besides the surface optical performance, it is also vital to analysis the topography of the surface. According to the theory of 'deterministic manufacturing' of ultraprecision machining, it is necessary to predict the surface quality based on the toolpath file of the surface. Therefore, the following sections will explain the conversions and the calculation of 3D surface parameters which provide a professional and intuitive view of the surface topography characteristic.

(2) Optical performance results and evaluation

When multiple rays are emitted from a point in the object's field of view and pass through the optical system, due to the existence of aberrations, their intersection with the image plane is no longer the same point, but forms a scattered diffuse spot, which is called a spot diagram. In the spot diagram, the size of these diffuse spots can be used to measure the image quality of the system. When the computer calculates the spot diagram, it divides the incident light pupil of the optical system into a large number of small facets of equal area and passes the light emitted from the point on the object through the center of each small facet. The light is traced along each curved surface of the system component. The light passing through each small facet in the entrance pupil will intersect on the image plane to form a point. The points on the image plane generated by all the light passing through these small facets are gathered together to form a spot diagram. According to the density of the spot diagrams generated by points in different object fields of view, the light intensity distribution of the system can be calculated. For example, the relative illumination distribution of the system can be calculated by combining the cosine theorem.

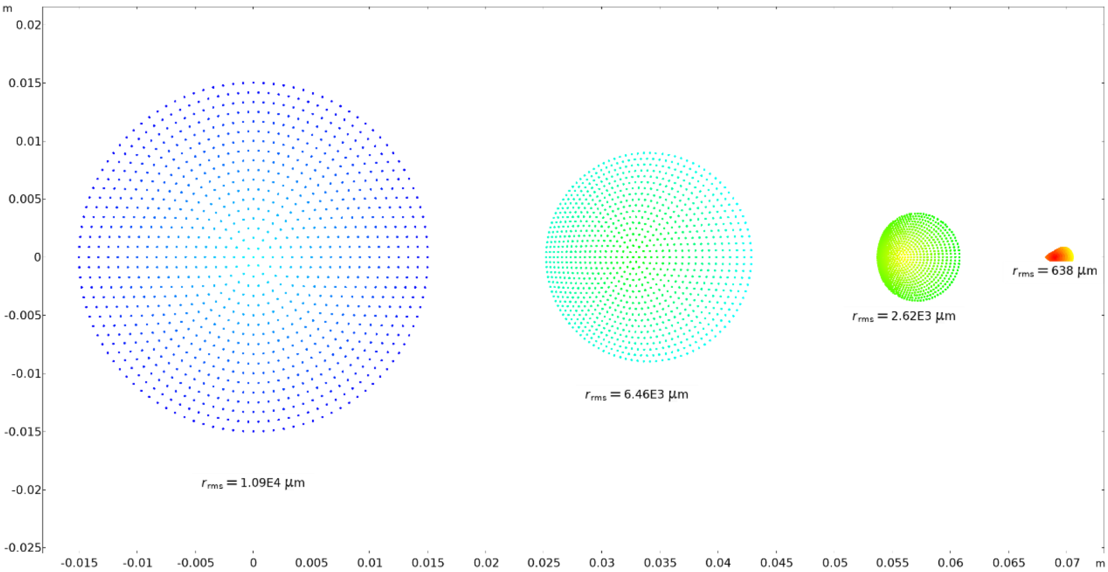

Figure 3.4 spot diagram from an off-axis parabolic mirror COMSOL raytracing simulation result.

Fig.3.3 shows the spot diagram of an off-axis parabolic mirror raytracing simulation, which includes the form of the ray differences by the time (ns) sequence. The sizes of the PSF diagrams formed by these four sequences of the times are as follows:

- 0 ns: 10.90 mm
- 0.42 ns: 6.46 mm
- 0.6 ns: 26.20 mm
- 0.72 ns: 0.0638 mm

The circle at the center of each PSF diagram represents the size of the diffraction-limited Airy disk. The smaller the diffuse spot in the PSF diagram, the closer it is to or smaller than the diffraction limit, indicating a better optical system. In general, the size of the PSF diagram in a qualified optical system should be within a few tens of micrometers, typically not exceeding 0.1 mm.

3.4.2 3D surface parameters and assessment

The upswing in the popularity and applications of freeform surfaced optics is due primarily to the advancements made in the ultraprecision manufacturing industry. Within the last 1-2 decades, ultraprecision technologies have evolved to point where they can reliably produce the complex shapes that freeform optical surfaces require, and most importantly, at an industrial scale with reasonable cost. One of the most common methods of machining freeform optics is single point diamond turning, where a blank is mounted to a spindle (C-axis) rotating at a few thousand of RPMs, while a stiff diamond-tipped tool (Z-axis) moves synchronized with the spindle rotation, to ultraprecision machining the surface as illustrated in Figure 1. To facilitate the manufacturing of freeform optics, the diamond turning machine is further outfitted with one of two ultraprecision machining modes, i.e. the slow tool servo mode and the fast tool servo mode [106], [107].

However, in the process of diamond turning of a freeform surface under either the STS or FTS mode, the normal and tangential cutting forces acting at the surface are constantly varied in light of the variation of freeform surface curvatures. Although the surface roughness of the freeform optics is uniformly obtained at a few nanometers level, the surface texture aspect ratios (S_{tr}) at the surface are varied substantially across the surface from one located point to another, because of the corresponding variations of the cutting forces across the surface locations. The variations of the surface texture aspect ratios on the optic surface have the obvious impact on the optical performance, one of which is the rainbow color phenomena reflected on the optic surfaces.

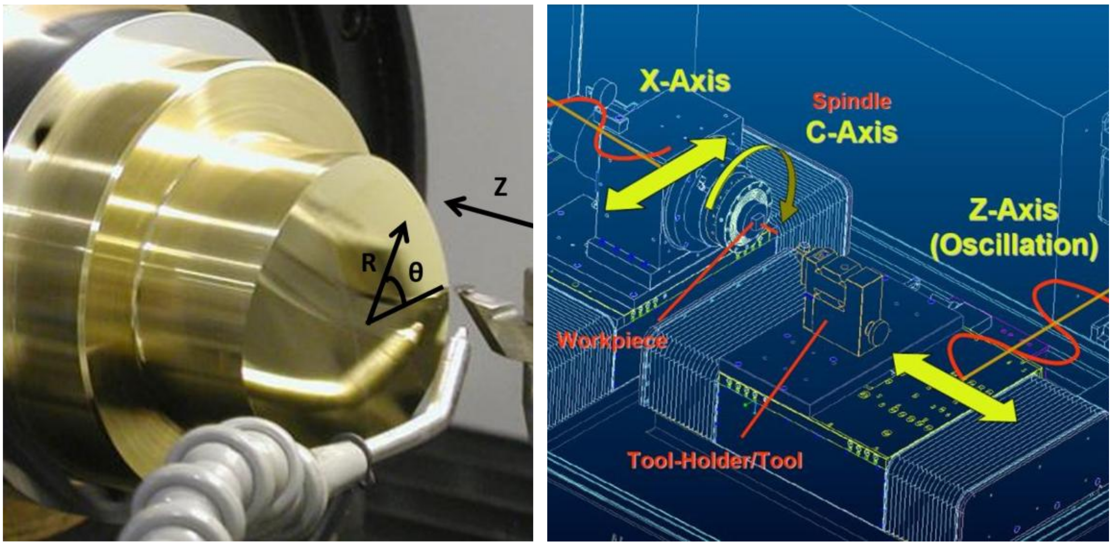

Figure 3.5 Typical diamond turning machine layout with application to ultraprecision machining of freeform optics.

Comparing with the traditional machining process, the difference of the diamond turning machine is that it does not need any additional process to the part such as polishing after the machining process. The surface finished by diamond turning machining process is already strictly imitating the designing form and contains nano-level's high quality surface roughness. While, in the method of nano-level optical surface measurement such as white light interference optics, the toolpath of the tool tip has been contained on the surface, which has significantly difference compared to the part which has been polished. As it illustrates on the Figure 3, Figure 3(A) presents an 3D surface measurement result of the center point of a freeform optical surface after machining, Figure 3(B) presents the result of the surface at the same position after polishing process. Based on this concept, we proposed a theory that the texture of the surface in diamond turning machining process may highly reflect the toolpath on the surface, which makes it contains more meaning than the surface produced by the traditional method.

To evaluate and characterize a freeform surface through the ultraprecision machined process, several surface parameters follow the standardized geometrical product specification and verification (GPS) characterization as contained in ISO GPS documents, in that a freeform surface is decomposed into form, shape and texture parameters [23]. Three specific parameters have been selected and used in the experiment: surface texture aspect ratio (Str), peak-and-valley value (PV value), and root-mean-square height of the surface (Sq) [108], and they are proposed as representations of the characteristics exhibited by the objective surface topography. The detailed analysis of these parameters serves to facilitate a comprehensive understanding of the functional attributes of the optic component surface concerning its intricate relationship with the machining process, which are further discussed below.

S_{tr} is the primary parameter considered in this context, due to its ability to evaluate the isotropic and/or anisotropic nature of the surface texture. For an ultraprecision machined surface, where the toolpath defines the surface texture, the S_{tr} value is crucial in assessing the quality of the machining process. Ideally, the S_{tr} value should remain within a small and consistent range across the entire surface, indicating a well-controlled and uniform machining process. The calculation of S_{tr} requires the ratio between the horizontal distance in the direction where the auto-correlation function decays to the value (typically 0.2 by default) most rapidly and the horizontal distance in the direction of the slowest decay of the auto-correlation function to the value(s). The auto-correlation function used for the calculation of S_{tr} is as follows:

$$S_{tr} = f_{ACF}(t_x, t_x) = \frac{\iint_A z(x,y)z(x - t_{x'}, y - t_y)dxdy}{\iint_A z(x,y)z(x,y)dxdy} \tag{3.16}$$

The result of S_{tr} normally between 0 to 1, when S_{tr} is close to 1 indicates the surface is isotropic. With decrease in S_{tr} the surface becomes more anisotropic. By quantifying the surface texture aspect ratio, we can assess the degree of surface roughness and the shape complexity of freeform surfaces.

RMS deviation of a surface is defined as the root-mean-square value of the departures relative to a reference plane, the leveled z plane, in units of length:

$$\mathrm{Sq} = \sqrt{\frac{1}{\mathrm{MN}}\sum_{i=1}^{M}\sum_{j=1}^{N} Z_{\mathrm{i,j}}^2} \tag{3.17}$$

As one of the most commonly used parameters in precision machined surface evaluation, Sq (root mean square roughness) is highly valued for its ability to quantify surface roughness. The choice to use Sq for evaluating the precision surface is based on its insensitivity to the sampling interval, which makes it reliable across various measurement resolutions. However, Sq is sensitive to the sampling area, meaning that larger or more diverse surface areas can lead to variations in Sq values. This sensitivity allows for a more comprehensive assessment of the overall surface texture and surface roughness at the component precision machined.

Shape parameters are closely related to geometrical tolerances, as they characterize deviations from the nominal form by analyzing the residual surface of the shape. The PV (Peak-to-Valley) value is a key shape parameter for a precision freeform surface, representing the total deviation across the surface. As it shown in equation (3.18), PV value is defined as the sum of the largest positive local deviation and the absolute value of the largest negative local deviation. This parameter provides a comprehensive measure of the surface overall deviation from the ideal or designed shape, making it crucial for evaluating the accuracy of freeform surfaces.

$$PV = Z_{pos} + |Z_{neg}| \tag{3.18}$$

3.4.3 Cutting forces modelling

In the SPDT machining process, the fabrication of freeform surfaces presents a notable challenge due to the continuous changes in surface curvature. These dynamic alterations correspondingly lead to variations in cutting angles during the machining process. The inherent changes in curvature directly influence both the cutting angles and the depth of cutting of the cutter, consequently affecting the cutting forces throughout the machining operation. Through an analysis of the toolpath file and the prediction of variations across the entire cutting loop, it becomes possible to examine the positional relationships among each cutter location point. This analysis aids in identifying problematic or challenging areas on the designed surface. From an industrial perspective, the utilization of toolpath analysis serves a dual purpose. Firstly, it provides the means to retrospectively trace the cutting process, enabling the identification of factors that may have contributed to the production of faulty parts. Secondly, this retrospective analysis serves as a valuable tool for preventing similar challenges in subsequent production cycles, contributing to enhanced efficiency and product quality.

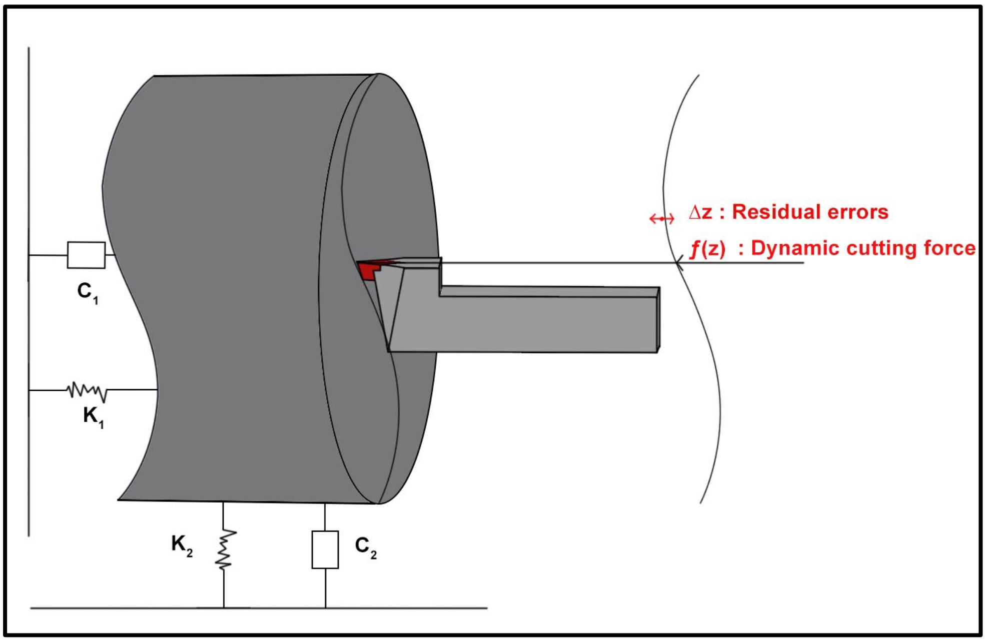

Figure 3.6 Schematic of the nano-sectioning by STS ultraprecision machining process.

As it has been shown in Fig.3.5, with the consideration of the direction of the cutting motion and the practical DoC. In instances where surface work plays a substantial role in steady deformation, several internal works are identified [109]:

i) Plasticity along the shear plane.
ii) Friction along the underside of the chip at the tool interface.
iii) Formation of a new cut surface.

Based on these assumptions, the cutting force equation during the cutting process was given by Atkins [105] as,

$$F_c V = (\tau_y \gamma)(t_u w V) + [F_c \sec(\beta - \alpha) \sin \beta] \frac{V \sin \phi}{\cos(\phi - \alpha)} + R w_u V \tag{3.19}$$

Where τ_y is the shear yield stress, γ is the plastic strain, R is the fracture energy or the specific work of surface formation divided by the area of the fracture surface, β is the Coulomb friction angle, α is the rake angle of the tool, ϕ is the shear plane angle, t_u is the uncut chip thickness, w_u is the width of cut, and V is the sectioning speed. The equation can be further written as:

$$\frac{F_c}{w_u} = \left(\frac{\tau_y \gamma}{Q}\right) t_u + \frac{R}{Q} \tag{3.20}$$

Where the friction parameter $Q = [1 - \sin \beta \sin \varphi \,/\, \cos(\beta - \alpha) \cos(\varphi - \alpha)]$. Williams et al. [49] derived the closed-form solution for ϕ as follows:

$$\cot \varphi = \tan(\beta - \alpha) + \sqrt{1 + \tan^2(\beta - \alpha) + Z[\tan(\beta - \alpha) + \tan \alpha]} \tag{3.21}$$

Where the dimensionless parameter $Z = \frac{R}{\tau_y t_u}$. And the values of τ_y and R can be obtained according to the value of ϕ.

3.5 Conclusions

In this chapter, the concept of virtual optics has been introduced, along with the underlying logic and methodological framework. Additionally, the method and calculation of ray tracing simulations for optical performance have been detailed. Furthermore, the principles for selecting 3D surface parameters, along with the corresponding calculation equations and assessment methods, have been discussed. Lastly, the cutting force model, including the method and approach for calculating cutting forces, has been explained. The methodology presented in this chapter will be fully adopted and applied in the subsequent chapters of this research.

Chapter 4

A web-based e-portal for integrated design, manufacturing and assessment of lenses and its implementation

4.1 Introduction

In contemporary freeform surfaced lens design and manufacturing, personalized mass customization is the primary feature, alongside maintaining high precision, standards of quality, the shortest delivery time, and cost efficiency. Varifocal lens manufacturing has been widely developed since the conception of freeform surface technology has freed many lens designers from the constraints of the traditional mass production of lenses by enabling a local prescription laboratory to deliver varifocal lenses designed and produced in a responsively mass-customized manner for a specific wearer [38]. A varifocal lens is composed of three main zones: a distant-vision zone, a near-vision zone, and a corridor zone that naturally bridges these two. Ensuring uniform optical power within the corridor zone is critical for providing clear near and distant vision, meeting specific clinical vision requirements. The manufacturing process of varifocal lenses typically involves the use of single-point diamond turning in the FTS mode, which is well suited to meet the high quality and controllable mass customization demands of the industry. Due to the stringent accuracy requirements in optics design and the high surface quality standards for the final product, a meticulous process is followed. This process encompasses surface modeling, design, toolpath generation with design for manufacturing, vision assessment, and the deterministic manufacturing of the lens.

However, such industrial processes often highlight the challenges in aligning optical design with manufacturing realities. The surface design is typically based on the unique specifications provided by the customer, while the manufacturing process is guided by the geometric constraints of the optical system. Discrepancies between design specifications and manufacturing constraints can lead to defects in the final product, resulting in surface quality degradation. This underscores the need for a platform that enables the integration between optical design and manufacturing seamlessly. Furthermore, such a platform would render a higher degree of responsiveness in the manufacturing process. In highly mass-customized production environments, effective communication among all the stakeholders and customers is crucial for ensuring that products meet all necessary specifications, particularly following the ultimate manufacturing goals in quality, costs, delivery time, and customer satisfaction. A web-based e-platform should facilitate real-time collaboration among design teams, manufacturers, and customers, ensuring smooth integration and communication throughout the entire production process chain and supply chain [110], [111].

This chapter presents a case study on the development of a web-based e-portal, and investigates the underlying associated holistic theoretical analysis, Multiphysics-based simulations, and their implementation and application perspectives. The framework of the e-portal has the ideology of enabling built-in information processing activities in a highly responsive mass-customized digital environment, which enables freeform surfaced optics design and manufacturing seamlessly while quality is assured in the 'earlier' stage in a virtual manner. The implementation of the e-portal developed enables users—such as optometrists, lens manufacturers, or patients—to input their prescriptions and visualize the resulting designed surface through 2D contour plots, 3D surface models, and functional performance in ray tracing simulations. Additionally, the resulting surface's point cloud file can be generated and shared with manufacturers to facilitate personalized 'mass production'. Therefore, the implementation and application perspectives are also discussed in depth in this paper.

4.2 Framework of the e-portal development

Efficient and effective varifocal lens production requires a manufacturing system that enables end-to-end personalized manufacturing capabilities. This involves initiating the lens design process by addressing each customer's specific requirements, planning and controlling customized production orders, and fulfilling and delivering products that meet both quality standards and customer satisfaction [112].

The responsive online platform primarily consists of three key functional modules, as illustrated in Fig.4.1: the prescription data import module, the simulation support module, and the embedded results and analysis module. In the varifocal lens design module, the varifocal lens freeform surface is designed according to the customer's personal pre-scription. Modeling and a series of assessments are conducted to ensure the designed freeform surface meets the lens quality requirements. The initial function of the online platform is to import data. Once all optical parameters have been correctly uploaded, the platform provides a visualized result of the designed surface and generates the calculated point cloud file in real time, supported by the results and analysis module and the simulation support module. The following subsections will describe these three modules in detail.

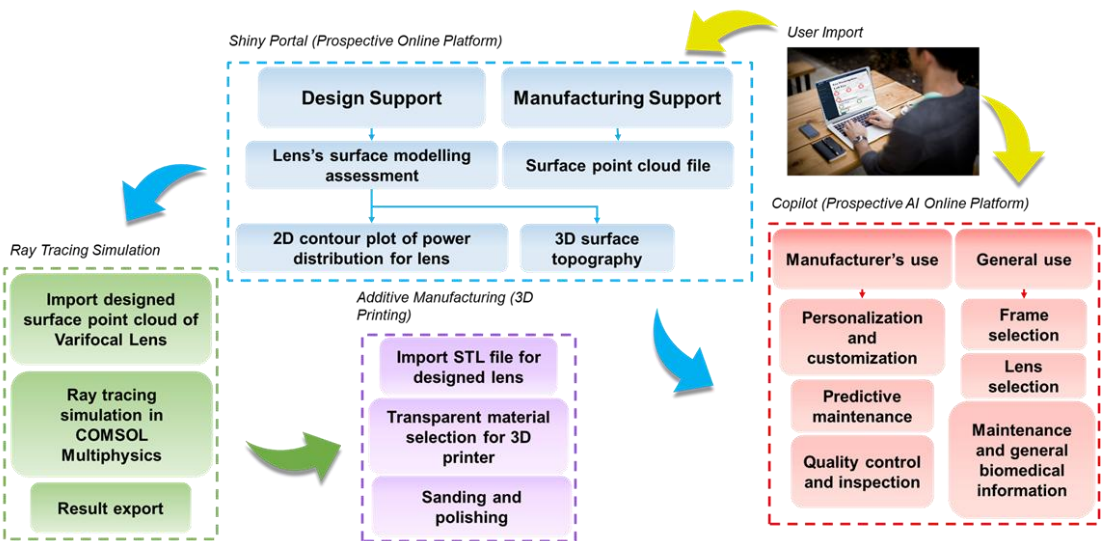

Figure 4.1 Manufacturing system of freeform surfaced optics and the built-in information processing activities.

4.3 Freeform Surfaced Lens: Prescription Data Input, Modelling and Analysis, and Material Specification and Selection

4.3.1 Surface data import

The e-portal system acts as a kernel of the manufacturing system, which can facilitate the customer's customized requirement either in prescriptions or prescript data, undertake modelling and design of the personalized freeform surfaces, design and manufacturing of the freeform surfaced lens, virtual assessment of the lens quality via ray tracing, and help track and trace the lens design and manufacturing processes for customers. To some extent, the e-portal reflects the advanced level of e-manufacturing for seamless integration of the lens design, manufacturing and services [113], [114]. Its essentials are to provide the interactive dynamics, the improved accuracy and productivity of the lens design and manufacturing by digitalization and data automation.

As illustrated in Table 4.1, the key optical and geometric parameters involved in the optical surface design have been listed. The optical parameters define the curvature radius of each lens zone, while the geometric parameters determine the positions of the near-vision and far-view zones, as well as the shape of the progressive corridor of the lens. In the industrial optics process, the geometric parameters are typically decided by the designer or manufacturer based on considerations of manufacturing and lens blank model selection. The optical parameters are provided by the customer according to their optometry results.

Table 4.1 The optical and geometric parameters for a varifocal lens.

Acronym	**Parameter's Description**
Geometric Parameter	
$\boldsymbol{L}$	Far-zone distance
$\boldsymbol{h}$	Lens corridor's length
$\boldsymbol{n}$	Refractive Index
$\boldsymbol{r(u)}$	Radius of Curvature
$\boldsymbol{rR}$	Lens near power
$\boldsymbol{rD}$	Lens distant power
Optical parameters	
$\boldsymbol{P_n}$	Spherical Power of near-view zone
$\boldsymbol{P_d}$	Spherical Power of far-view zone
$\boldsymbol{ADD}$	Addition power, spherical power difference between $\boldsymbol{P_n}$ and $\boldsymbol{P_d}$
$\boldsymbol{n}$	Refractive Index
$\boldsymbol{CYL}$	Cylinder, optical cylinder power
$\boldsymbol{PSM}$	Prism, customer prism position
$\boldsymbol{AXS}$	Axis of the optics

On the online platform, customers have two options for uploading their prescriptions. For manufacturers in order to handle a large number of prescriptions, the platform provides a file upload function that allows them to upload customer prescriptions in an Excel table format. The platform also presents initial data statistics, enabling the uploader to review and modify their data if necessary. Additionally, the platform allows customers to manually input both geometric and optical parameters of their prescriptions, as illustrated in Fig.4.2.

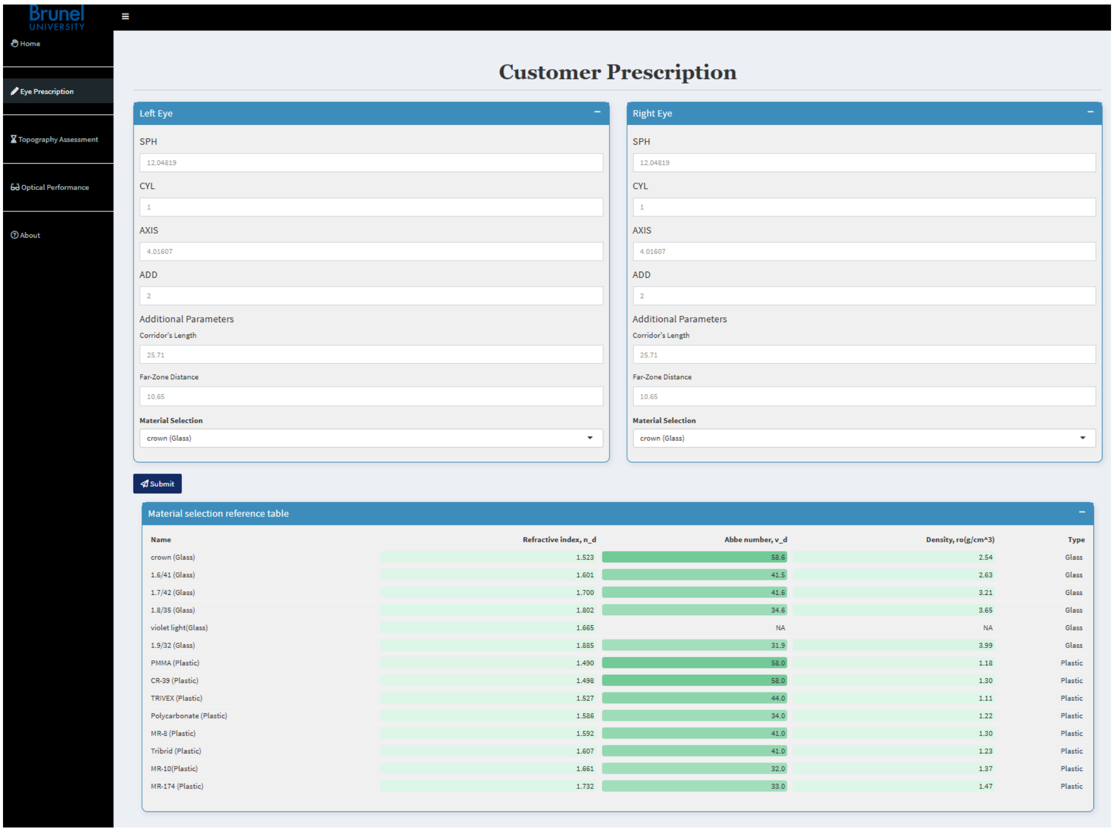

Figure 4.2 Prescription import page of the e-portal, enabling customers to responsively input their respective vision prescription and specification of their optics materials.

4.3.2 Lens Material Specification and Selection

Material selection plays a crucial role in optical surface design. It not only affects the resulting surface power, refractive index, and radius distribution, but also influences the thickness ---- center thickness (CT) and edge thickness (ET) of the lens product. Based on the (4.1) formula, CT and ET of a lens based on its Power (D), Refractive Index (n), and Diameter (d), can be calculated.

$$CT - ET = \frac{D \times h^2}{2000 \times n} \tag{4.1}$$

One of the primary properties of materials used in ophthalmic design is the refractive index (n), defined as the ratio between the speed of light in a vacuum and the speed of light in the material for a given wavelength. This value is always greater than 1, as light travels faster in a vacuum than in any material. The refractive index is directly related to the curvature and thickness of the lens[115]. In ophthalmic optics, the refractive index plays a crucial role because it connects the optical properties of a lens—namely, refractive and prismatic power—with the lens geometry, particularly curvature and thickness.

$$P = (n-1)\left(\frac{1}{R_1} - \frac{1}{R_2}\right) = (n-1)K \quad (4.2)$$

Equation (4.2) represents the example of this relation, which links the power of a thin lens P with the radii of curvature R_1 and R_2 of the two lens surfaces through the refractive index n. By combining these geometric factors into a single parameter K, it becomes evident that the same lens power can be achieved with different combinations of materials and curvatures. Refractive indices for glass materials range from 1.5 to 2, while those for plastics vary from 1.498 to 1.74 for high-index polymers [115]. Table 4.2 summarizes the properties of the most common materials in the ophthalmic industry. The platform includes dozens of widely used optical materials, compiled in Table 4.2, which provides a reference of essential parameters for each material, allowing users to select the appropriate options during data import.

Table 4.2 Summary of the main specifications of a selection of ophthalmic materials [6].

Material	**Refractive Index(n)**	**Abbe Number**	**Density (kg/m^3)**	**Type**
Crown	1.523	58.6	2.54	Glass
1.6/41	1.601	41.5	2.63	Glass
1.7/42	1.7	41.6	3.21	Glass
1.8/35	1.802	34.6	3.65	Glass
1.9/32	1.885	31.9	3.99	Glass
PMMA	1.49	58	1.18	Plastic
CR-39	1.498	58	1.3	Plastic
Trivex	1.527	44	1.11	Plastic
Polycarbonate	1.586	34	1.22	Plastic
MR-8	1.592	51	1.3	Plastic
Tribrid	1.607	41	1.23	Plastic
Mr-10	1.661	32	1.37	Plastic
Mr-174	1.732	33	1.47	Plastic

4.3.3 Calculation process

The characteristic of the varifocal lens optical power progressively change from top zone to the bottom zone of the lens, and its surface feature of no axis of rotational invariance, which could be identified as a freeform surface [116]. As shown in Fig.4.3. the upper part of the lens always is recognized as the distant-vision zone and the bottom part as the near-vision zone which both parts have relatively constant powers. The progressive corridor contains optic power varies between distant-vision zone to near-vision zone [117].

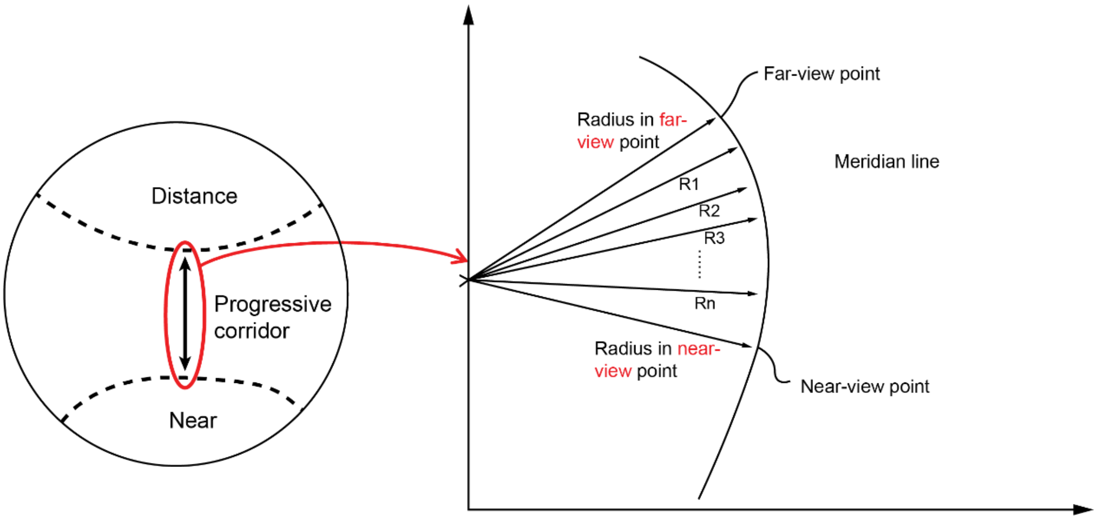

Figure 4.3 The process of parameters management in design process of the case study varifocal lens.

The computational modeling and analysis for lens surface generation are implemented once the customer submits their prescription. The algorithm behind the platform includes the necessary computations to generate the lens surface and produce the intend-ed outputs. Specifically, the portal uses Winthrop's [77] model functions to create the PAL freeform surface of the varifocal lens. The lens surface is defined by an eighth-order polynomial power law, as expressed in function (4.3) and further detailed in function (4.4) (4.5).

$$\frac{1}{r(u)} = \frac{1}{rD} + \left(\frac{1}{rR} - \frac{1}{rD}\right) \times \sum_{i=1}^{8} c_i (u+L)^i \tag{4.3}$$

Where constant coefficients are shown below:

$$c_1 = c_2 = c_3 = c_4 = 0, \tag{4.4}$$

$$c_5 = 56/h^5$$

$$c_6 = -140/h^6 \tag{4.5}$$

$$c_7 = 120/h^7$$

$$c_8 = -35/h^8$$

It should be mentioned that rD is considered as distant power where as rR is the near power for the lens and is related to Refractive index, SPH and ADD value as shown in equations (4.6) and (4.7).

$$rR = \frac{(n-1) \times 1000}{SPH + ADD} \tag{4.6}$$

$$rD = \frac{(n-1) \times 1000}{SPH} \tag{4.7}$$

The function $u(x, y)$ essentially gives each point on the surface where its level curve crosses the x-axis. After performing detailed mathematical calculations and analysis on this relationship in Winthrop method[77] by Wei et al. in 2020[71], equations (4.7) to (4.8) is considered to calculate $u(x, y)$ as followed:

$$u(x, y) = \frac{h}{2} - L + g - (sgn\, p) \times \left(g^2 - \frac{h^2}{4}\right)^{\frac{1}{2}} \tag{4.8}$$

$$g = \left(\frac{1}{2}\right) * \left(p + \frac{y^2 + \frac{h^2}{4}}{p}\right) \tag{4.9}$$

$$p = x - \frac{h}{2} + L \tag{4.10}$$

The progressive Varifocal Lens's surface, denoted as $f(x, y)$, is defined by a specific set of mathematical equations. These equations determine the precise shape and properties of the surface which are given as functions (4.11) to (4.14) [118]. Various design of the surface is generated by different mathematical functions that defines the meridional power law, represented as $r(u)$. By changing this function, different embodiments of the surface can be created [38], [39], [118].

$$z(x, y) = b(u) - \{r(u)^2 - [x - a(u)^2] \; - y^2\}^{\frac{1}{2}} \tag{4.11}$$

$$a(u) = u - r(u) * sin\theta(u) \tag{4.12}$$

$$b(u) = r(u) * cos\theta(u) + \int_0^u tan\theta(u) du \tag{4.13}$$

$$sin\theta = \int_{0}^{u} \frac{du}{r(u)} \tag{4.14}$$

After defining the bipolar progressive surface z (x, y) through a list of mathematical equation codes written in R-Script language, the next step involves featuring the given results throughout the Shiny online portal to the user in the form of plots and diagrams.

4.4. Ray tracing simulation assisted by multiphysics modelling and analysis

Varifocal lenses, commonly marketed as "All-Purpose" solutions, aim to provide a balanced visual experience for both distance and near vision. While this approach may seem convenient, it inherently limits the diversity and customization of viewing zones available to users. In contrast, progressive lenses produced using Freeform surfacing technology offer greater adaptability, allowing for more personalized lens configurations. However, selecting lenses based solely on the customization of viewing zones also has its limitations. This method often depends on access to detailed evaluations of each lens's optical performance, which may not be consistently available or straightforward to obtain. The lack of comprehensive and easily accessible performance data can hinder both eye care professionals and consumers from making fully informed decisions. As a result, identifying the optimal lens design for individual visual requirements becomes a challenging process, particularly when aiming for a truly tailored visual solution.

The advent of Freeform technology in lens manufacturing has revolutionized the field by enabling the creation of customized progressive lenses tailored to specific visual requirements. This technology allows for more flexibility in designing viewing zones, offering a more personalized and effective vision solution than traditional varifocal lenses, which are limited in their configuration options. As a result, Freeform technology has the potential to address the diverse visual needs and preferences of individuals more precisely. To validate the performance of these designed lenses, it is essential to conduct a thorough analysis. In this regard, the Ray Tracing method, facilitated by COMSOL Multiphysics, was employed to assess the optical behavior of the previously designed lens surface through the Shiny portal.

The ray tracing simulation was developed using COMSOL Multiphysics software, following a structured workflow illustrated in Fig.4.4. The simulation process consists of four main steps. The first step involves importing the designed lens surface into the simulation environment. This is achieved by uploading the surface data point cloud, which provides the foundation for reconstructing the lens's geometry. Once the surface data is imported, the second step focuses on building a 3D model of the desired lens. This model should accurately represent the lens's physical characteristics, including its shape, material properties, and thickness, ensuring that it reflects the real-world behavior of the lens.

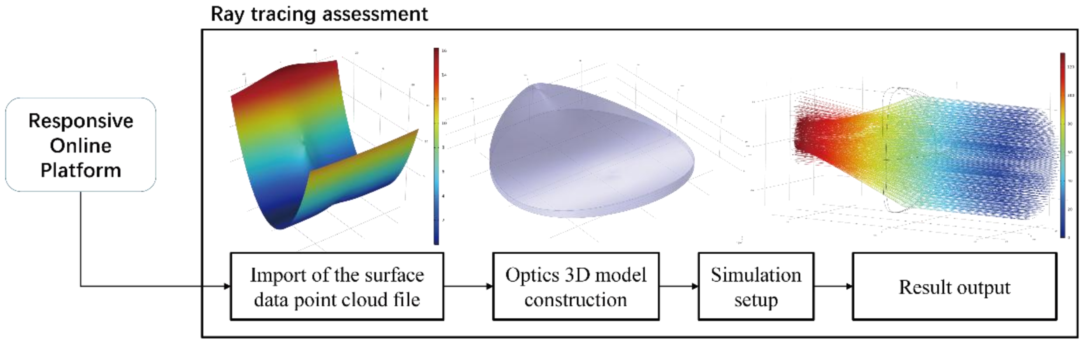

Figure 4.4 Process of ray tracing simulation setup and result output with COMSOL Multiphysics.

After the 3D model is successfully constructed, the third step involves configuring the simulation environment. This includes defining the positions for ray generation and specifying the termination areas where the rays will be captured. These parameters are critical for simulating realistic optical conditions and obtaining meaningful results. The final step is the execution of the ray tracing simulation itself. Once the simulation environment is set up, the rays are traced through the lens, providing insights into the lens's optical performance, including focal points, aberrations, and light distribution patterns.

The result output from the simulation helps in validating the designed lens's optical quality, offering a detailed understanding of how the lens performs in practice. This approach provides valuable data that can inform further refinement of the lens design and contribute to the development of more advanced and personalized optical solutions.

4.4.1 Import of the surface data point cloud file

The surface data point cloud file is generated by the web-based portal based on the customer’s prescription. Multiple formats for data input can be selected, including file uploads, local tables, or Excel files. For ease of data collection and manipulation, the data has been standardized in Excel format. Once the data points are imported into the simulation model, the software utilizes this information to create a mesh for the point cloud. This mesh serves as the foundation for subsequent steps in the simulation process, including 3D model construction and ray tracing analysis. The accuracy of the point cloud data is critical for ensuring the precision of the lens model and, ultimately, the reliability of the ray tracing simulation results.

The algorithm behind the data imported into the simulation model uses a linear interpolation method to generate the defined surface based on the point cloud, with the aim of minimizing precision loss during the conversion process. Linear interpolation helps the model evaluate the behavior of the function both between the discrete points defined by the table or file, and in areas outside the domain covered by the provided data. The linear interpolation method employs linear polynomials to estimate the function values between the known data points, ensuring a smooth transition across the surface. This approach is particularly effective when dealing with data point clouds, as it allows for accurate surface modeling while maintaining computational efficiency. By minimizing potential precision loss, the interpolation method ensures that the reconstructed surface closely aligns with the original design parameters

4.4.2 Simulation Setup

After the surface data points have been imported and the defined freeform optics surface has been successfully generated, the next step is to configure the simulation parameters. Table 4.3 lists all the parameters used in the simulation model, including their expressions, descriptions, and the current values applied. These parameters are crucial for accurately defining the optical characteristics of the model, ensuring that the simulation reflects the intended performance of the freeform surface. The careful selection and application of these parameters allow for a precise simulation environment, ultimately leading to more reliable and meaningful results.

Table 4.3 Expression of each parameter that is calculated for the simulation setup.

Name	Expression	Value	Description
$\boldsymbol{CT}$	$ET + \dfrac{(D \times h^2)}{(2000 \times n)}$	1.1265	Calculated center thickness
$\boldsymbol{D}$	4	4	Diopter of the optics
$\boldsymbol{ET}$	$1.5[mm]$	0.0015	Estimated edge thickness
$\boldsymbol{h}$	$30[cm]$	$30[cm]$	Lens blank radius
$\boldsymbol{lambda}$	$550[nm]$	$550[nm]$	Standard radiation wavelength
$\boldsymbol{n}$	1.6	1.6	Refractive index
$\boldsymbol{N_{ring}}$	36	36	Standard number of rings
$\boldsymbol{P_{nom}}$	$58.941[mm]$	$0.058941[m]$	Standard entrance pupil diameter
$\boldsymbol{\theta_x}$	$0[deg]$	$0\ rad$	Standard X direction angle
$\boldsymbol{\theta_y}$	$0[deg]$	$0\ rad$	Standard Y direction angle
$\boldsymbol{v_x}$	$tan(\boldsymbol{\theta_x})$	0	Ray direction vector, X component
$\boldsymbol{v_y}$	$tan(\boldsymbol{\theta_y})$	0	Ray direction vector, Y component
$\boldsymbol{v_z}$	1	1	Ray direction vector, Z component

The parameters listed in Table 4.3 summarize the key parameters used in the simulation model. Each parameter is carefully selected to reflect realistic conditions and ensure that the model accurately represents the intended lens design. Some critical parameters in the table are organized bellow which highly influence the practical optical performance of the optics:

- Center Thickness (CT) and Edge Thickness (ET) define the lens geometry, directly affecting light propagation and optical performance.
- Diopter (D) determines the lens's refractive power, influencing its ability to focus light and correct vision.
- Lens Radius (h) impacts the curvature of the lens surface, affecting the field of view and power distribution.
- Wavelength (λ), set at 550 nm, represents standard visible light, allowing for typical optical performance assessments.

Together, these parameters ensure that the ray tracing simulation can accurately replicate real-world lens behavior. By optimizing these values, the model is capable of providing a detailed analysis of the lens's optical performance, including its focal length, aberrations, and image clarity.

Fig.4.5 illustrates the setup principle of the ray tracing simulation based on ISO 8980-1 standards for ophthalmic optics. This standard outlines a physical inspection system for quality testing of machined varifocal optics, serving as a reference for conducting digital optics inspections. Object 1 is a light source set to a brightness exceeding 400 lumens, while Object 2 is a diaphragm, which controls the direction and position of light from the source to the subject optics (Object 3). Object 5 represents a matte black background on which the inspection results are observed. Following this principle, our ray tracing inspection setup was implemented in a virtual environment, with the position and direction of the light source defined accordingly, without the need for a matte background cover.

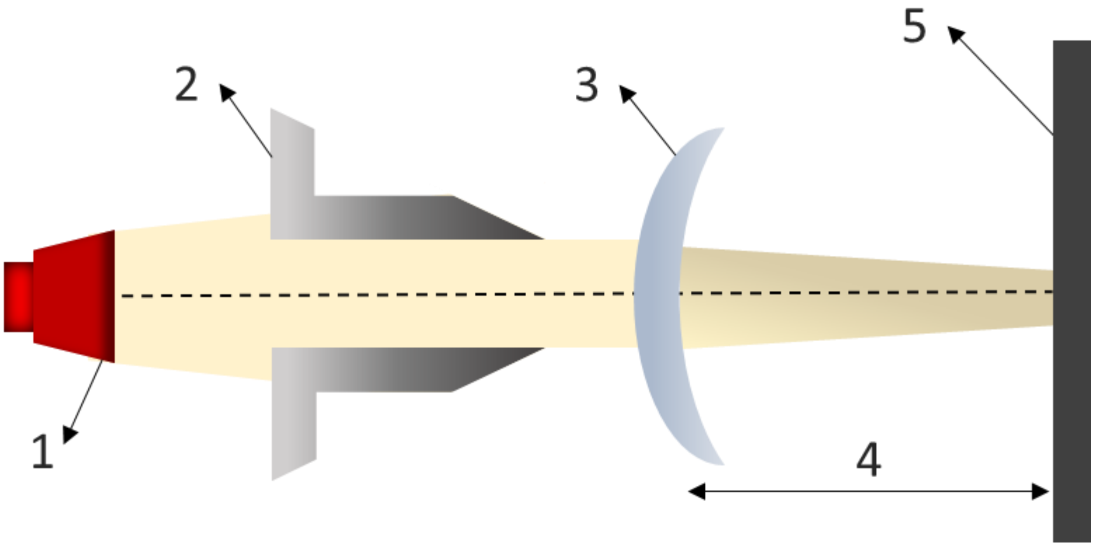

Figure 4.5 Recommended system for visually inspecting a lens for defects: (1) light source; (2) light beam diaphragm; (3) designed freeform surface optics; (4) back focus length of the optics; and (5) black background for imaging.

4.4.3 Three-Dimensional Optics Model Construction and Its Material Selection

Once the simulation setup was complete, a 3D optics model was constructed based on imported surface data. This model includes all the essential elements of a well-machined optical lens. As shown in Fig.4.6, a spherical meniscus lens model was created, where *d* represents the lens diameter, *R1* is the radius of the convex surface, and *R2* is the radius of the concave surface. The red line between the convex and concave surfaces indicates the designed surface, with the distance between each point on the defined surface and its corresponding point on the convex surface representing the lens thickness.

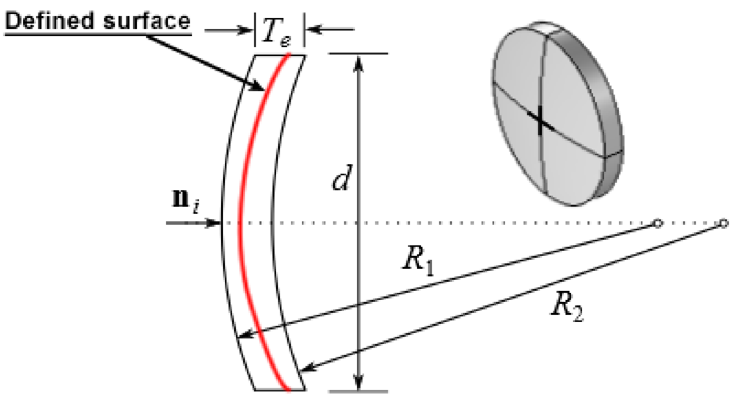

Figure 4.6 Spherical lens with a convex face and a defined surface combined as the concave face.

Material selection is a crucial step in the simulation process, following the construction of the

3D optics model. As discussed earlier, the refractive index is the primary property that differentiates various materials used in optics, significantly affecting the distribution of the designed surface and the resulting lens thickness. Fig.4.7 shows the refractive index plot of an optical material commonly used in progressive additional lenses—polycarbonate $(C_{16}H_{14}O_3)_n$. The x-axis represents the wavelength of light interacting with the material, while the y-axis indicates the corresponding refractive index value. This material is widely selected by the optical industry due to its favorable properties for lens manufacturing.

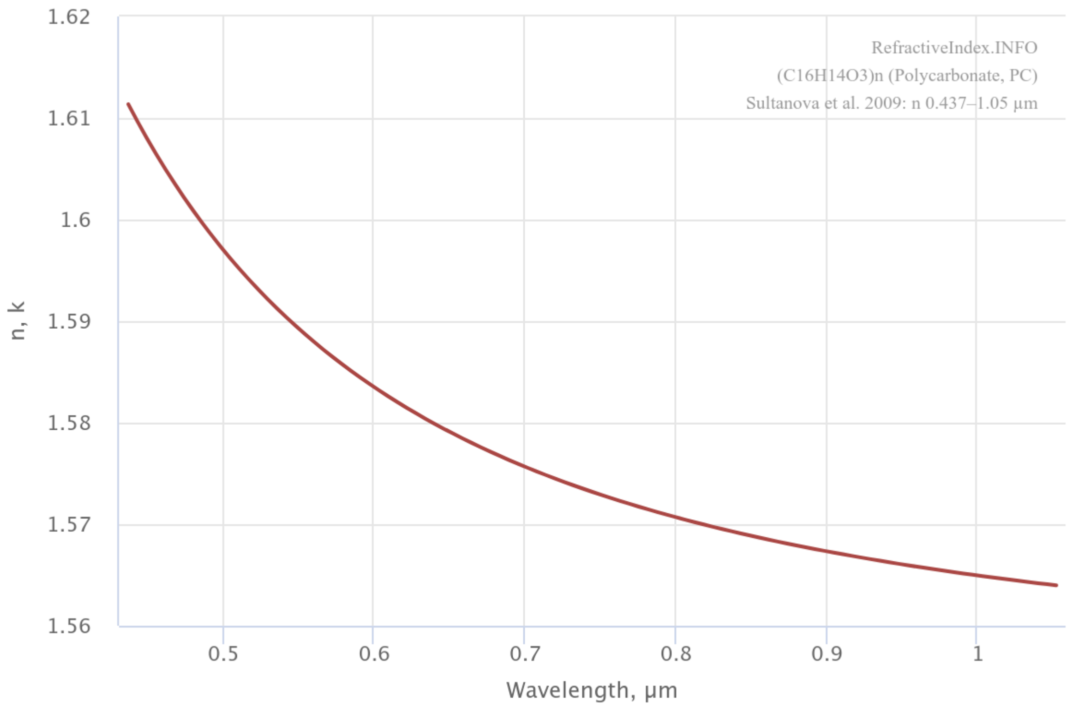

Figure 4.7 Refractive index of $(C_{16}H_{14}O_3)_n$(Polycarbonate, PC)[119].

4.4.4 API connection

To conduct the simulation through the portal, it was necessary to connect the plat-form to the simulation software. This was accomplished using the COMSOL API. The COMSOL Multiphysics 6.0 API is a software interface that includes all the algorithms and data structures needed to define and manipulate COMSOL models. Every time a model is created in COMSOL Desktop®, it is essentially interacting with the COMSOL API in the background. This connection allows for seamless integration between the simulation platform and the software, enabling the automatic transfer and execution of complex models.

4.5 Case study: experimental setup and key parameters

To strengthen the connection between theoretical analysis and practical validation to the function of the portal, a case study of freeform surface varifocal optics constructed according to the above principles in accordance with this paper's invention, and suitable for general use, will be presented in this subsection. The following experiment demonstrates how the web-based platform could be applied to a varifocal lens prescription from a lens manufacture company, as the highly responsive portal for freeform surface evaluation either shows up the surface topography result or its optical performance. The case can be directly loaded into the web-based platform by visiting ‘https://liusha.shinyapps.io/3DPortal/’ (Accessed on 17 August 2024), with the manual input of the provided prescription.

The experiments were performed on a UPL250 ultraprecision machine, renowned for its nano-level accuracy, high precision, and superior dynamic performance, which minimizes the dynamic effects of both the machine tool and cutting tool during machining. Given the high-volume fraction of reinforced particles and their substantial abrasive properties, polycrystalline diamond tools have demonstrated superior performance compared to other tool types and are therefore widely used in SPDT machining. The experimental setup employed two polycrystalline diamond tools, each with a cutting-edge radius of 0.35 mm and an included angle of 60 degrees.

To demonstrate the responsiveness of the web-based platform in evaluating the optical performance of the varifocal lens, in this section, we present several simulation results to demonstrate the functional performance of the designed surface. The computational domain has been set as $\Omega = [-30, 30]^2$, containing the circular domain with the length unit mm according to the practice of varifocal lens manufacture.

The varifocal freeform optics surface defined by the power law of Equation (4.11) will now be evaluated for a lens with a reading addition of 2.00 diopter. The optical constants of the defined lens are assumed for a polycarbonate (PC) material with a refractive index of 1.5640. And the value of the vertical distance between the distance point to the reference point h is 37.71 mm and the distance between the distance point to the origin point O is 10.65 mm. For the customer’s optical prescription, Table 4.4 shows the customer optics parameter selection for ultraprecision machining on the lens milling-turning machine. The most vital parameters for optics design in this prescription has been highlighted in the table, sphere power (SPH), cylinder power (CYL), axis, and addition power (ADD).

Table 4.4 Detailed lens prescription for ultraprecision machining on the lens milling-turning machine.

SPH	CYL	AXIS	ADD
12.048	-0.50	0.0	2.0

4.6 Results and discussion

Fig.4.8 shows the results of a computer evaluation of the equations using the specified parameter values. Fig.8(a) presents the contours of constant mean surface power distribution, while Fig.8(b) shows the contour of Z point cloud distribution. Additionally, (c)(d) provide a 3D view of the distribution of surface mean power and Z point cloud values. Analyzing these figures reveals that the power and astigmatism characteristics of the lens are smooth and gradually varying, indicating a well-designed optical surface.

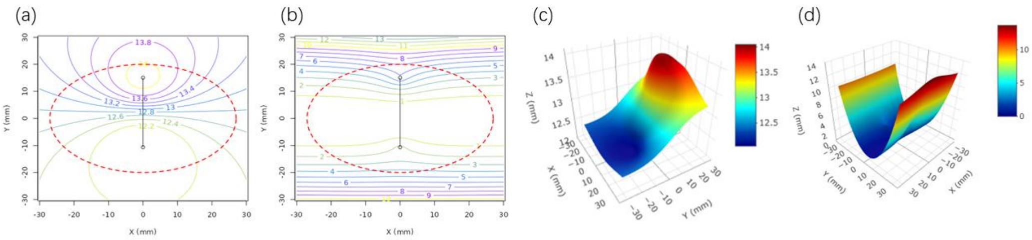

Figure 4.8 The result plots from the portal evaluation using the provided parameter values: a) contour plot of constant mean surface power; b) contour plot of the calculated Z value distribution; c) 3D visualization of the surface mean power distribution; and d) 3D visualization of the calculated Z value point cloud distribution.

From Fig.4.8(a), it can be observed that the resulting optical surface has an equivalent spherical power of 12.2 diopter in the near vision area, closely matching the customer's specified spherical power. The difference from the theoretical near vision power of 12.04819 diopter is less than 0.08 diopter. In the upper part of Fig.4.8(a), an elliptical region with an equivalent spherical power of 14 diopter corresponds to the far vision zone. The mean optical power difference between the near and far vision areas is 1.8d, which aligns with the provided additional parameter (ADD). Fig.4.8(b) shows the contour plot of the calculated Z value distribution, representing the resulting surface point cloud. This plot provides an intuitive visualization of the surface characteristics, allowing users to better understand the geometry of the optical surface.

As previously illustrated, the optical performance test was conducted using ray tracing simulations with the assistance of COMSOL Multiphysics. Fig.4.9(a) and Fig.4.10(b) show the resulting plot of the freeform surface, which was generated by importing the platform's designed surface data points. From these figures, it is evident that the imported surface has been constructed as a 30 × 30 × 20 3D freeform surface, with a peak-to-valley distance of 16 mm. With the observation in Fig.4.9(b), the progressive corridor has been accurately constructed, and the characteristics of the surface in the plot align perfectly with the surface depicted in Fig.4.8(d), the 3D visualization on the web platform.

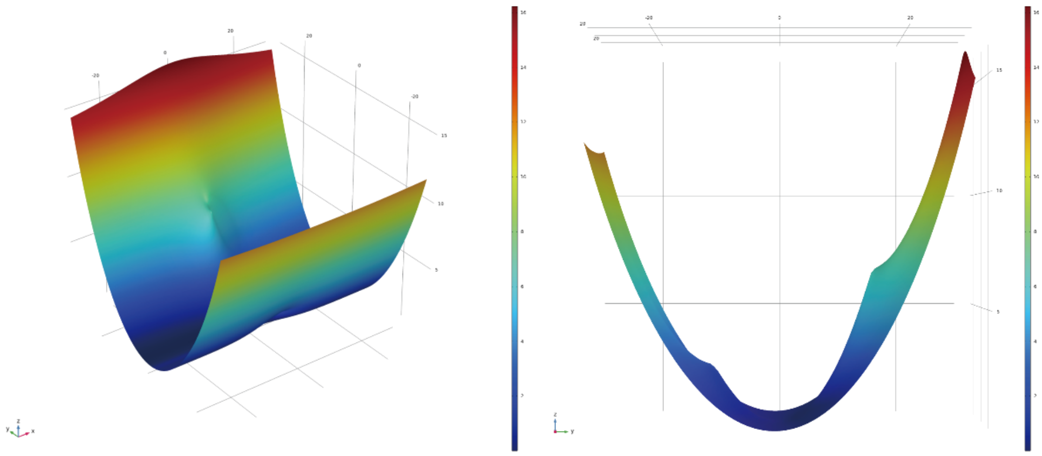

Figure 4.9 Three-dimensional freeform designed surface in COMSOL Multiphysics by importing data points from Shiny portal. a) the resulting plot of the designed surface; b) the plot with the observation of the ZOY direction of the same surface which provides a better view of the progressive corridor.

After successfully importing the surface, the 3D optics model was constructed accordingly. The convex surface of the optics model features a spherical lens surface with zero spherical power and custom cylinder power, while the concave surface incorporates the imported surface with the full customer's specified spherical power. The material selected for the lens is polycarbonate $(C_{16}H_{14}O_3)_n$, as introduced earlier, with a refractive index of n = 1.5848 and an Abbe number of $V_d = 27.86$.

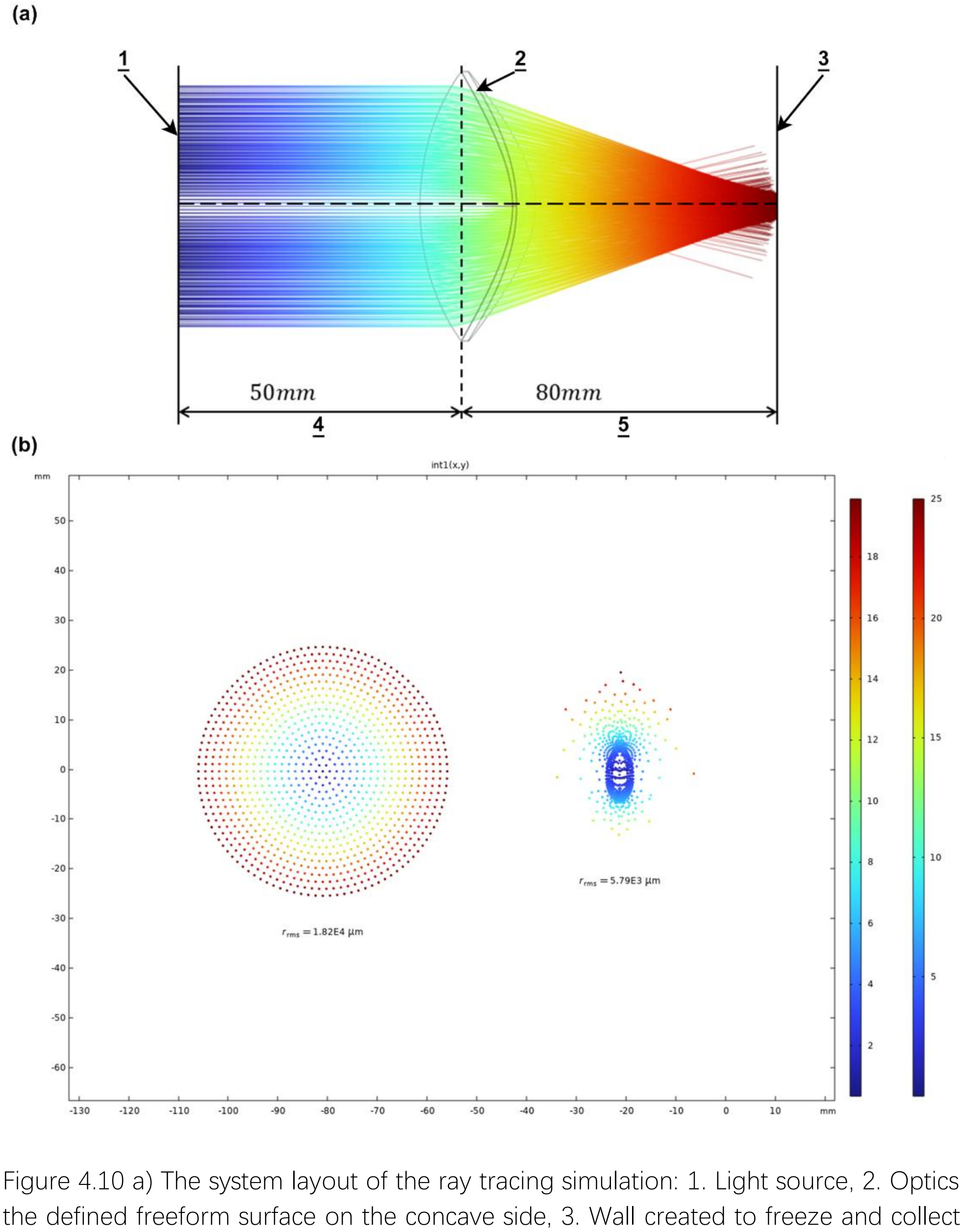

Figure 4.10 a) The system layout of the ray tracing simulation: 1. Light source, 2. Optics model with the defined freeform surface on the concave side, 3. Wall created to freeze and collect the rays, 4. Distance between the light source and the optics model, 5. Distance between the optics model and the image plane; b) The 2D spot diagram illustrating the ray distribution before and after passing through the optics model.

Fig.4.10(a) illustrates the final simulation layout and the resulting optical performance of the subject optics model. The simulation system design closely references the recommended optical performance inspection system from ISO standard 8980-1. On the left side of the plot is the light source, followed by the optics model with the freeform surface applied to its concave side.

A freeze wall has been created to collect rays passing through the optics, allowing for adjustable distances between the model and the collection wall. In this simulation, the distance between the light source and the optics is set to 50 mm, while the distance from the optics to the resulting wall is 80 mm.

Fig.4.10(b) presents the 2D spot diagram illustrating the ray distribution before and after passing through the optics model. The diagram on the left shows the ray distribution at the point of creation, while the diagram on the right shows the distribution on the freeze wall. The optical performance has improved significantly, reducing the RMS radius of the rays from 1.82×10^4 to 5.79×10^3. Additionally, the rays are concentrated into two focal points: one at a y-value of 0 mm and another at a y-value of -10 mm.

4.7 Concluding remarks

In this chapter, a web-based e-portal for freeform surfaced lens design and manufacturing is presented; while its development has the ideology of considering the highest responsiveness and agility in the personalized design and manufacturing of the lenses, the quality and customer satisfaction are well assured in the 'earlier digital' stage in a virtual manner. This innovative e-portal is presented by further considering the effects of the freeform surface design, its material selection, quality lost during the data point cloud file transfer from design to manufacturing, 2D and 3D visualization and inspection of the designed surface topography, real-time resulting surface data output, and the simulation of the lens optical performance assessment. The underlying implications of the web-based e-portal and its experimental evaluation and validation are also applicable to further develop the scientific understanding on freeform surfaced lens design, modeling, and analysis, and continuous improvement in deterministic manufacturing via a well-connected digital virtual environment. The distinctive conclusion for this research work can be drawn from the following aspects:

- A theoretical analysis and development of a web-based portal for freeform surface optics design and modeling were conducted. The primary objective was to enhance responsiveness and agility in personalized freeform surface manufacturing.
- A holistic discussion of an integrated approach to freeform surface manufacturing was presented, combining freeform surface design, surface modeling, topography characteristic analysis, and optical performance simulation.
- A portal-driven method for the freeform surface optics industry was identified through multiscale mathematical analysis, experimental evaluation, and validation of the ultraprecision machining process. This method integrates surface design, modeling, analysis, assessment, and manufacturing. By incorporating detailed material selection and 2D/3D surface model representations, the simulation outcomes demonstrate the portal's capability to design surfaces based on customer prescriptions, predict optical performance, and provide a reliable reference for optimizing freeform surface optics during the design and modeling process.

Chapter 5

Dynamic cutting forces modelling and analysis

5.1 Introduction

In SPDT precision manufacturing process, cutting force significantly reflects the cutting phenomenon including size effect, minimum chip thickness effect, chip formation, cutting temperature and tool wear etc. Thus, cutting force in ultraprecision machining process is observed of great importance to analyze the cutting mechanics, machinability and its further optimization. On the other hand, especially during the machining process of freeform surfaces optics which contain constant changes of cutting angle and DoC (Depth of Cut), the scaled-down cutting parameters enlarge the errors generated by the designed facial-form of freeform surface, cutting tools and micro cutting process variables, significantly affect the machining performance including form accuracy, surface texture, surface roughness and tool life and eventually induced the optical functionality error and defect the surface. These errors normally generated due to the size effect, tool and workpiece deflection, dynamic runout, tool wear, cutting friction, cutting angle difference, DoC changes and chatter vibration. Considering these errors, dynamic cutting force is considered as the major factor in target the error and do optimization in SPDT machining process. Thus, in order to target the error before the machining process, an improved dynamic cutting force model is critical to illustrate the tool-workpiece interaction and accurately predict the cutting force on the high precision level.

The cutting force modelling and its application in interpreting the machining process has been extensively researched and developed based on theoretical assumptions and experimental observations. In ultra-precision cutting, SPDT stands out as the primary method for achieving surface roughness at the nanometer level [120]. In SPDT machining process, the cutting tool material consists of a single-crystal diamond with a small diameter cutting edge. This nanoscale cutting edge facilitates the production of smooth surfaces with minimal damage to the top surface [8]. Apart from traditional slow tool servo cutting technology, fast tool servo cutting is employed to achieve high accuracy on complex non-spherical surfaces and microstructures [121]. Furthermore, due to the rapid development and widespread application of freeform surfaces, optimizing freeform surface toolpath generation has become increasingly vital in the state-of-the-art ultra-precision machining field [2], [122]. In the SPDT process, research has been conducted to explore the capabilities in different materials [123], [124] and shapes [125]. In addition, some integrated research explores such as Macro-micro dual -drive technology, contributing to the advancement of both ultra-precision systems and macro–micro dual-drive technology [126].

The cutting force holds paramount significance in the single-point diamond turning machining process as it reflects the direct interaction between the cutter and the workpiece. Leveraging the wealth of information derived from the toolpath data, which is intricately linked to the designed freeform sur-face, cutting force modelling emerges as a highly promising approach for ensuring the quality control of the designed sur-face. Over the past decade, extensive research has been con-ducted on cutting force in single-point diamond turning machining processes. This research encompasses areas such as cutting force prediction, analysis of cutter kinematic motion, including cutting force tracking and prediction[127], cutting force control for improved surface results, and the investigation of the relationship between chip loads and cutting force fluctuations [128], etc. The anticipation of required cutting forces in advance serves as the foundational element for linking resulting surface quality to the cutting process."

In the SPDT machining process, the fabrication of freeform surfaces presents a notable challenge due to the continuous changes in surface curvature. These dynamic alterations correspondingly lead to variations in cutting angles during the machining process. The inherent changes in curvature directly influence both the cutting angles and the depth of cutting of the cutter, consequently affecting the cutting forces throughout the machining operation. Through an analysis of the toolpath file and the prediction of variations across the entire cutting loop, it becomes possible to examine the positional relationships among each cutter location point. This analysis aids in identifying problematic or challenging areas on the designed surface. From an industrial perspective, the utilization of toolpath analysis serves a dual purpose. Firstly, it provides the means to retrospectively trace the cutting process, enabling the identification of factors that may have contributed to the production of faulty parts. Secondly, this retrospective analysis serves as a valuable tool for preventing similar challenges in subsequent production cycles, contributing to enhanced efficiency and product quality.

In this chapter, theoretical analysis on the cutting force and its modelling are presented in the ultraprecision diamond turning of freeform surfaces, particularly considering constant variations of cutting forces along the freeform surface curvature and the increasingly stringent requirement on high precision optical surface finishing. The cutting forces modelling is based on integration of Akins model with the influence of shear angles varying constantly on the freeform surface conduction. Based on the toolpath data of the cutting process at the freeform surface, the depth of cut of the surface, curvature variations, and shear angle variations throughout the process are meticulously analyzed. Subsequently, a cutting force model is developed to discern the nuances of the cutting motion by analyzing the cutting toolpath, and then consequently enabling the prediction of cutting forces variation during orthogonal cutting motion with a round-edged diamond cutting tool. Finally, an integrated approach for examining the correlation between cutting forces and the analysis of surface texture and texture aspect ratio should be developed and further investigated, particularly on the functionality of a freeform surface and its generation in ultraprecision machining.

5.2 Toolpath generation

In the STS ultra-precision machining process, toolpath is one of the most critical factors in freeform surface optics manufacturing, as it defines the relative position between the workpiece and cutter, directly influencing the resulting surface topography. Given this, G-code has been selected as topography data in the development of dynamic cutting force models.

Figure 5.1 illustrates the STS diamond turning machining process and machine configurations. The cutting tool is mounted on either the X-axis or Z-axis, while an air-bearing spindle chuck holds the workpiece on the C-axis.

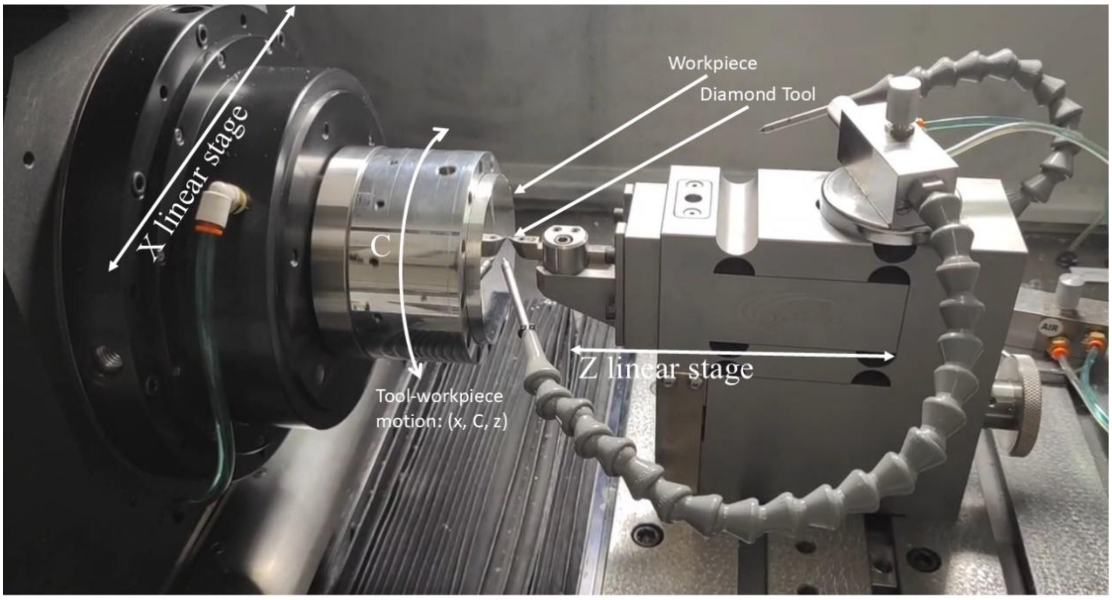

Figure 5.1 Schematic of the three-axis STS diamond turning machining process with a freeform surface workpiece on machining

As depicted in Fig.1(a), the three-dimensional trajectory of the machine tool in STS mode has been evenly discretized into N cutter location points (CLPs). The trajectory can be conceptualized as the Archimedes spiral pattern motion of the cutter within the $O-X\theta Z$ cylindrical coordinate system. In this system, the XOY plane is aligned parallel to the spindle surface. On this plane, the cutter's movement follows a linear motion with uniform speed along the X-axis direction (either from the centre to the edge or vice versa). This motion is coordinated with the rotational movement of the spindle in the C-axis. As a result, an Archimedean spiral pattern is generated, with a predetermined distance between each point and a specified feed rate. These parameters significantly influence the number of points in each circle and the number of circles the cutter needs to traverse, which, in turn, has a substantial impact on the resulting quality and processing time of the machine. The specific values of these parameters are generally dependent on the tool radius.

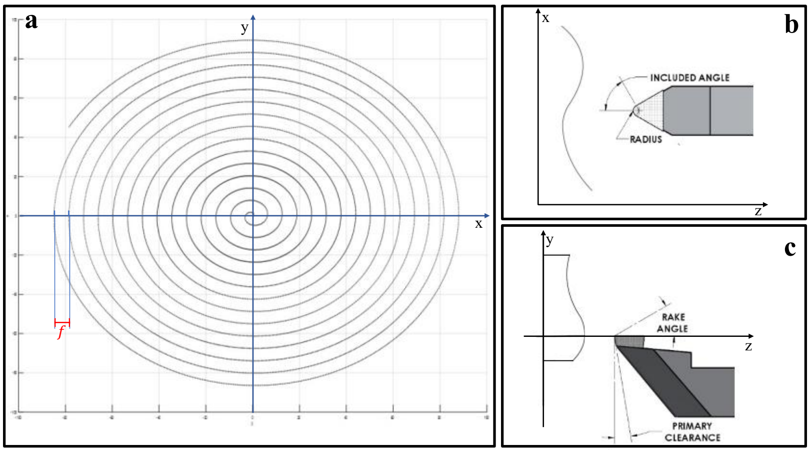

Figure 5.2 Schematic of cutting kinematics of diamond turning machining. a) the toolpath of the surface in the XOY plane; b) the tooltips and surface relationship at the top view; and c) the lateral

view of the cutting process.

The YOZ plane runs parallel to the plane defined by the cutting edge of the tool, while the XOZ plane illustrates the correlation between the tool radius and the movement along the x-direction. Both planes collectively portray the motion of the cutter along the Z-axis direction. Understanding and optimizing these trajectories are crucial for achieving precise and efficient machining, considering the interplay between tool geometry and the chosen toolpath strategy.

5.3 Cutting forces modelling

With the help of Atkins' model, the overall main cutting force can be obtained as follows:

$$F_c V = (\tau_y \gamma)(t_0 w V) + [F_c \sec(\beta - \alpha) \sin\beta] \frac{V \sin\phi}{\cos(\phi - \alpha)} + RwV \tag{5.1}$$

where V is the cutting velocity, F_c is the horizontal component of the cutting force, τ_y is the (rigid-plastic) shear yield stress, γ is the shear strain along the shear plane, given by $\gamma = cot\varphi + \tan(\varphi - \alpha) = cos\alpha/\cos(\varphi - \alpha)sin\varphi$; t0 is the uncut chip thickness, w is the width of the orthogonal cut, φ is the orientation of the shear plane and R is the specific work of surface formation (fracture toughness). The constant parameters using for calculation have been listed in the Table 5.1.

Table 5.1 Constant parameters using in the calculation

Parameters	Definition	value
Vr	(r/s) Spindle rotation speed	3000
τ_y	(MPa) Shear yield stress	55.2
μ	The coefficient of friction	0.583
r	(mm) Tool radius	0.35
D	(mm) Objective diameter	78
α	(mm) Tool rake angle	0

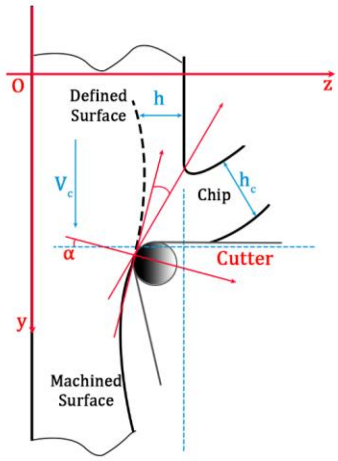

Figure 5.3 Schematic of the cutting force model in ZOY plane processing freeform surface by ultraprecision machine.

Akins' model provides a critical key to calculate the cutting force in the energy translation progress during the cutting process. While during the nano-level freeform surface machining process which have the characteristic that constant variation of the surface curvature, the curvature of the surface varied in the whole cutting period. It is critical to investigate the correlation between the variation of surface curvature and corresponding cutting force, the idea of the cutting force calculation with varied curvature referenced by Zhiwei's investigation of cutting force in Fast/Slow tool servo machining process[129].

The developed dynamic cutting force model was built under MATLAB, and the geometry data of the defined freeform surface used for the model is the toolpath generated by the CNC machine software (NanoCAM3) with the consideration of the most represented data to illustrate the situation under the machining progress. Besides the surface geometry, the extracted toolpath data basically contains most of the information of the machining process, such as tool radius, rake angle and included angle, orientation of cut, federate, processing type, etc. moreover, based on the G-code which interpret the location data of each point, the practical curvature of the surface at each point, current DoC, can also been calculated.

Based on this conception, a dynamic cutting force model has been developed. As it illustrates in the Fig.5.3, in the YOZ plane during the cutting period, the cutter is positioned perpendicular to the surface during the whole machining process, and the rake angle of the cutter is zero. The practical rake angle α still exist and varies consequently by the curvature of the current point changes. Besides, ϕ in the figure indicates the angle between between the current shear plane and the vector of the cutting direction $\vec{\delta}$. The depth of cut h also changes in response to curvature variation. The cutting forces acting on the cutting tool are mainly dependent on two factors, which is the practical shear angle according to the practical curvature and the consequently DoC leaded by the changes of the shear angle. The practical shear direction in the XOZ plane can be calculated according to following formula:

$$\phi = \frac{\pi}{4} - \frac{\beta - \alpha}{2} \tag{5.2}$$

In this scenario, where β represents the friction angle along the rake face, and α is the tool rake angle.

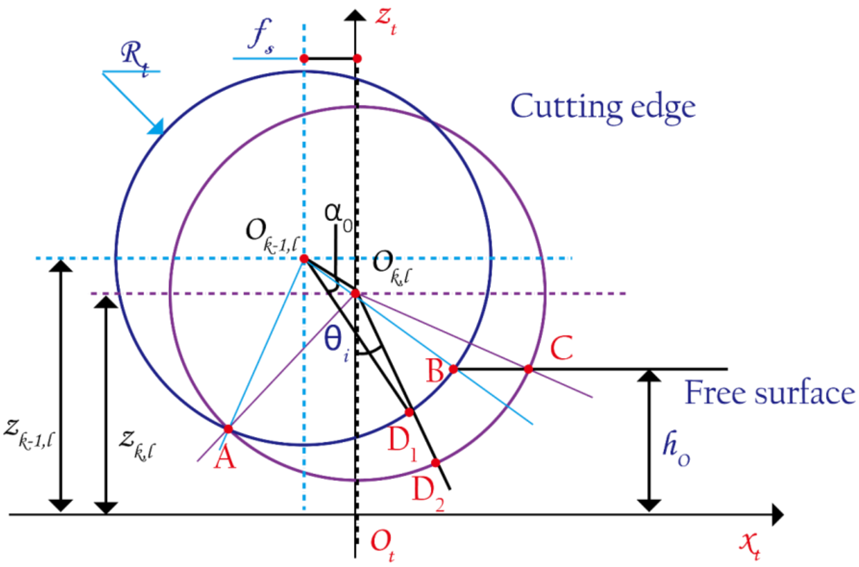

Figure 5.4 Schematic of the instantaneous material removal in STS UPM.

A schematic of tool engagement in the XOZ plane is illustrated in Fig.5.4 to aid in calculating the DoC, with the cutter assumed to be positioned at the i-th CLP. Here, the uncut surface of the workpiece is assumed to be planar. The local coordinate system oxz is defined on the rake face of the cutter to analyse the relationship between two consecutive CLPs and calculate the practical DoC and corresponding cutting force. In the figure, the half-circle represents the edge of the cutter, illustrating the cutting process as the oz-axis moves from CLP_{i-1} to CLP_i The vectors $o_{i-1,l}D_1$ indicate the direction of the shear plane at each respective position as the cutter progresses. The ABC marks specific points along the cutter edge, with point A representing the intersection of the cutter edge as it transitions from $o_{i-1,l}$ to $o_{i,l}$. Points B and C indicate the intersections between the cutter edge and the uncut surface.

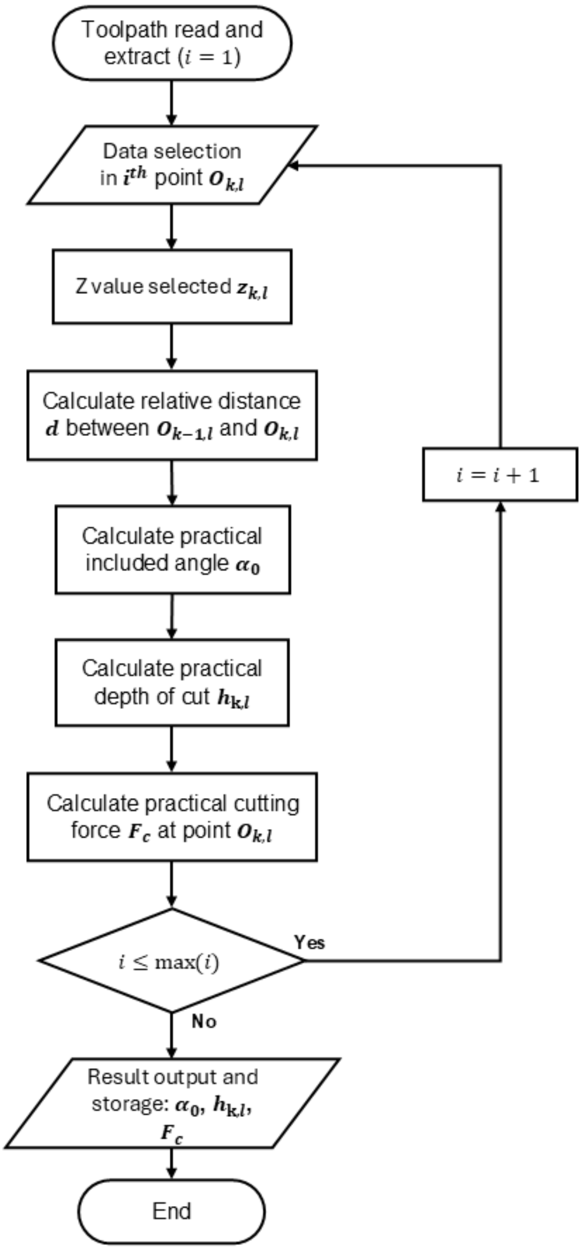

Figure 5.5 Algorithm flow of the cutting force model.

Accordingly, Fig.5.5 presents the algorithm behind the model. The discrete cutting location will be evaluated and calculated from $i = 1$ to $i = n$ sequence, n equals to the number of CLPs. After the value $z_{k-1,l}$ and $z_{k,l}$ along the z-axis at i^{th} cutting location point and $(i-1)^{th}$ CLP has been collected, the relative distance d between these two location points can be calculated using the following function.

$$d = \sqrt{f^2 + \left(z_{k-1,l} - z_{k,l}\right)^2} \tag{5.3}$$

where f represents the federate along the X-axis of the cutting process. Moreover, the included angle α_0 between the direction of the two selected points to the shear plane $o_{i-1,l}D_1$ can be expressed by

$$\alpha_0 = \arctan\left(\frac{z_{k-1,l} - z_{k,l}}{f}\right) \tag{5.4}$$

The coordinates of the intersection point A (Xa, Za) between the cutter edge at the previous (i-1)-th point and the current i-th point can be calculated by

$$\begin{cases} x_a = -\frac{1}{2}f - \sqrt{r^2 - \left(\frac{d}{2}\right)^2}\sin(\alpha_0) \\ z_a = \frac{1}{2}(z1 + z2) - \sqrt{r^2 - \left(\frac{d}{2}\right)^2}\cos(\alpha_0) \end{cases} \tag{5.5}$$

The coordinates of the intersection points B (Xb, Zb) and C (Xc, Zc), corresponding to the cutter edge at the preceding (i-1)-th point and the current i-th point, with the uncut surface, can be calculated by

$$\begin{cases} x_b = \sqrt{r^2 - (z1 - h_0)^2} - f \\ z_b = z_c = h_0 \end{cases} \tag{5.6}$$

Where h_0 is the height of the uncut surface in the toolpath data. And the relative angle between the i-th point to point A, B, and C respectively can be obtained as

$$\begin{cases} \theta_a = \arcsin\left(\frac{x_a}{r}\right) \\ \theta_b = \arctan\left(\frac{x_b}{z2 - h_0}\right) \\ \theta_c = \arcsin\left(\frac{x_c}{r}\right) \end{cases} \tag{5.7}$$

Accordingly, the practical DoC can be calculated by using the equations (7) below.

$$\begin{cases} DoC = \frac{1-\cos(\alpha_0+\theta_i+\alpha_1)}{\cos(\alpha_0+\theta_i)}, \text{where } \theta_a \le \theta_i < \theta_b \\ DoC = r\cos(\alpha_0) - \frac{z2-h0}{\cos(\theta_i)}\cos(\alpha_0), \text{where } \theta_b \le \theta_i < \theta_c \end{cases} \tag{5.8}$$

With the calculated shear angle ϕ and DoC t_0, the overall main cutting force at the CLP_i can be obtained by using Atkins model, as the equation of the model has been introduced in equation (3.14) but further written as:

$$\frac{F_c}{w_u} = \left(\frac{\tau_y \gamma}{Q}\right) t_u + \frac{R}{Q} \tag{5.9}$$

5.4 Experimental evaluation and validation

5.4.1 Experiment setup

In the prior section, an enhanced theoretical model of dynamic cutting force in the context of freeform surface SPDT ultraprecision machining was introduced. This model incorporates a detailed analysis that extends to the cutting tool's dynamic movement, the real depth of cut DoC, and the intricate path traced by the tool tip. Here, we delve into an in-depth evaluation and thorough validation of this innovative dynamic cutting force model. To achieve this, meticulously crafted cutting experiments are executed, each designed to test varying cutting parameters. These trials not only scrutinize the accuracy and robustness of the model but also reveal nuanced interactions between tool dynamics and machining precision. The results gathered from these controlled experiments substantiate the effectiveness and predictive capability of the model, providing a comprehensive understanding of its performance under different machining conditions.

The experiments were performed on a UPL250 ultraprecision machine, renowned for its nano-level accuracy, high precision, and superior dynamic performance, which minimizes the dynamic effects of both the machine tool and cutting tool during machining. Given the high-volume fraction of reinforced particles and their substantial abrasive properties, polycrystalline diamond tools have demonstrated superior performance compared to other tool types and are therefore widely used in SPDT machining. The experimental setup employed two polycrystalline diamond tools, each with a cutting-edge nose radius of 0.35 mm and an included angle of 60 degrees, as depicted in Figure 5.7.

5.4.2 Experiment procedures

As it interpreted in the 5.3 section, the main machining parameters that influencing cutting force are spindle rotation speed, federate, and the tool wear set: tool radius and tool rake angle. In addition, the material selection of the subject surface also as a critical factor due to it links to the shear yield stress and the coefficient of friction. The parameters for machining process and coefficients of the material selection used for the experiment are shown in Table 5.1. In the SPDT machining process, cutting tool perform Archimedean spiral motion according to the defined surface shape. Figure 5.5(a) illustrates the cutting motion within the machining process, emphasizing the mirror surface machining procedure utilizing a carrier disk. As shown in Figure 5.8(b), the carrier disk has a diameter of 290 mm and can accommodate up to six mirrors simultaneously. The mirrors are symmetrically distributed, with two positioned at the top and bottom and one on each side. The cutter operates on all six mirrors within the container, seamlessly alternating between kinematic movement and advancing to the next surface. The machined surface roughness, Peak-valley distance, surface texture aspect ratio, surface profile and topographical feature are measured and adopted by using the ZYGO New View 5000 white light interferometer with excellent precision and accuracy.

As explained in Section 5.3, the main machining parameters influencing cutting force are spindle rotation speed, feed rate, and tool wear characteristics, including tool radius and rake angle. Additionally, material selection plays a critical role, as it directly affects shear yield stress and the coefficient of friction. The parameters for the machining process and the material properties used in the experiment are listed in Table 5.1. In the SPDT machining process, the cutting tool follows an Archimedean spiral motion based on the defined surface shape. Fig.5.6(a) illustrates the cutting motion within the machining process, highlighting the mirror surface machining procedure using a carrier disk. As shown in Fig.5.6(b), the carrier disk has a diameter of 290 mm and can hold up to six mirrors simultaneously. The mirrors are symmetrically arranged, with two positioned at the top and bottom and one on each side. The cutter operates on all six mirrors within the container, alternating seamlessly between kinematic movements and advancing to the next surface. The machined surface roughness, peak-to-valley distance, surface texture aspect ratio, surface profile, and topographical features are measured with high precision and accuracy using the ZYGO New View 5000 white light interferometer.

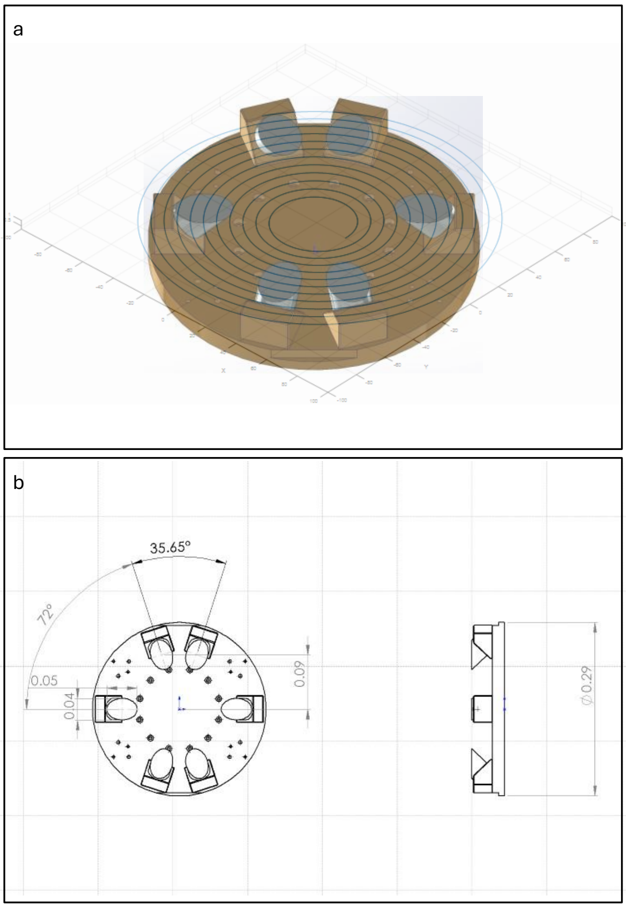

Figure 5.6 a) Cutting motion in the process and mirror surface machining procedure with a carrier

disk. b) Parameters and spread of the workpieces on the carrier disc.

5.4.3 Result and discussion

A series of dynamic cutting force simulations of the SPDT ultraprecision machining are carried out according to the machining parameter provided above. Fig.5.7 shows the predicted instantaneous dynamic cutting force in a complete cutting circle. The dynamic cutting force by utilizing a diamond cutting tool with the radius of 0.35mm, 0^{o} rake angle, federate of 0.01 μm, splindle rotation speed 3000 r/s, the material selection is PMMA with shear yield stress $\tau_y = 55.2$ and coefficient of friction of the material $\mu = 0.583$. The predicted cutting force curves effectively represent the cutting process as the tool follows its toolpath trajectory, including the periods when the tool moves across the gaps between each mirror. These curves capture the entire cutting process, encompassing the elastic recovery zone, ploughing zone, and shearing zone. By observing the cutting force curve over the entire period, two main characteristics can be observed. Firstly, there is a period of high-frequency oscillation in the cutting force between $1200\ ms/s$ to $1320\ ms/s$. Second, a high uniformity and smooth arc are present between these high-frequency oscillations. These variations in force strongly reflect the behavior of the cutting tool as it follows the designed trajectory, with two distinct movements: material removal and movement across the gaps between mirrors.

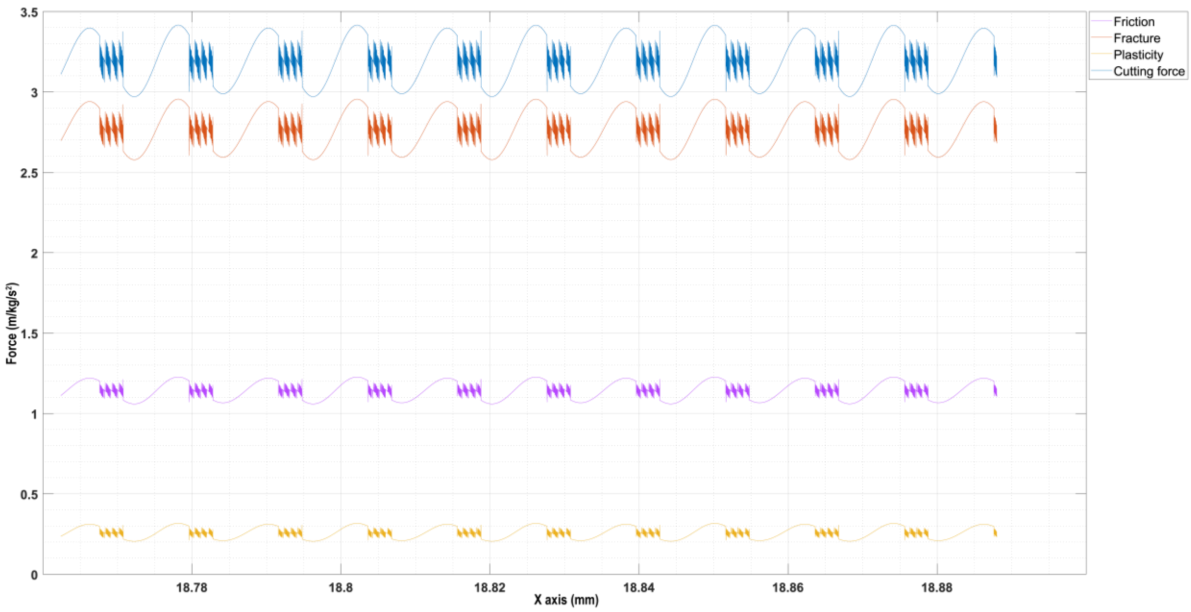

Figure 5.7 Predicted cutting force with its three working forms (Plasticity, Fracture, and Friction) during the machining an off-axis parabolic mirror by SPDT ultraprecision machining process.

To provide a more detailed insight into the characteristics of cutting force changes during the cutting process, a specific segment was selected where the cutter's position along the X-axis ranged from 18.8635 cm to 18.8665 cm, focusing on material removal from the surface. Fig. 5.8 shows the predicted practical cutting force with its three divided work form (Plasticity, Fracture, and Friction) during the machining process according to the introduced equation (3.14). A clear periodic pattern is observed during this motion, with the estimated minimum cutting force occurring when the cutter is positioned at 18.8642 cm along the X-axis. At this point, the cutting force is recorded as 0.0120778 N.

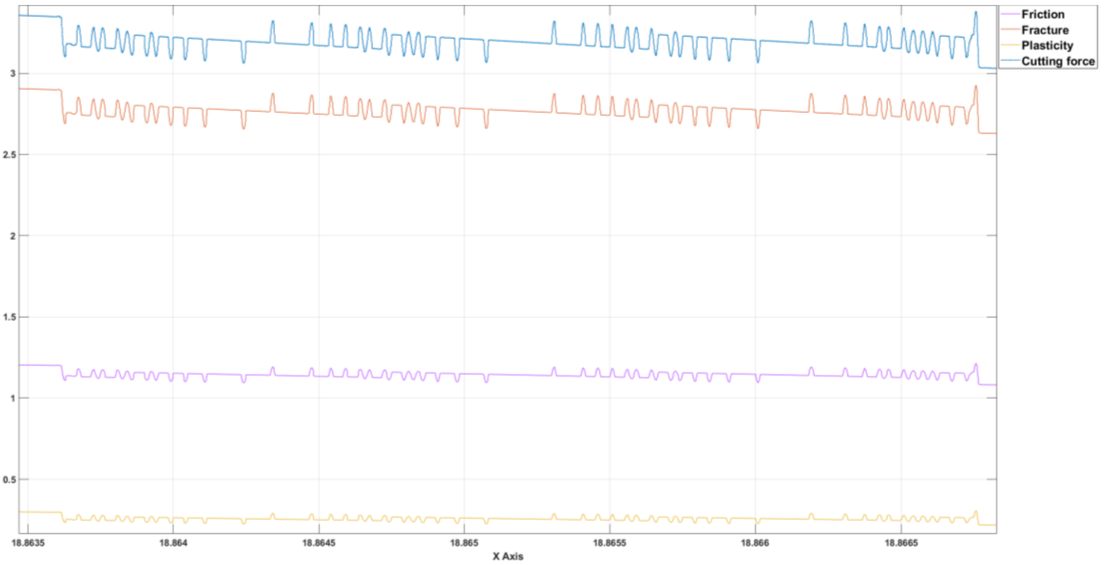

Figure 5.8 Detailed cutting force distribution in the model result with its three mechanisms.

The simulation results demonstrate distinct phase differences among the three mechanistic contributions during the machining process. Fracture mechanics emerges as the dominant energy-consuming mechanism, governed primarily by the material properties of the workpiece and the toolpath trajectory. Friction mechanics, identified as the secondary contributor, arises from interfacial tribological interactions between the tool rake face and chip material. This mechanism exhibits strong dependence on shear angle, depth of cut, and tool rake face geometry. Finally, plastic deformation mechanics constitutes the tertiary energy dissipation pathway, with its magnitude modulated by material constitutive behavior, cutting depth, and tool velocity.

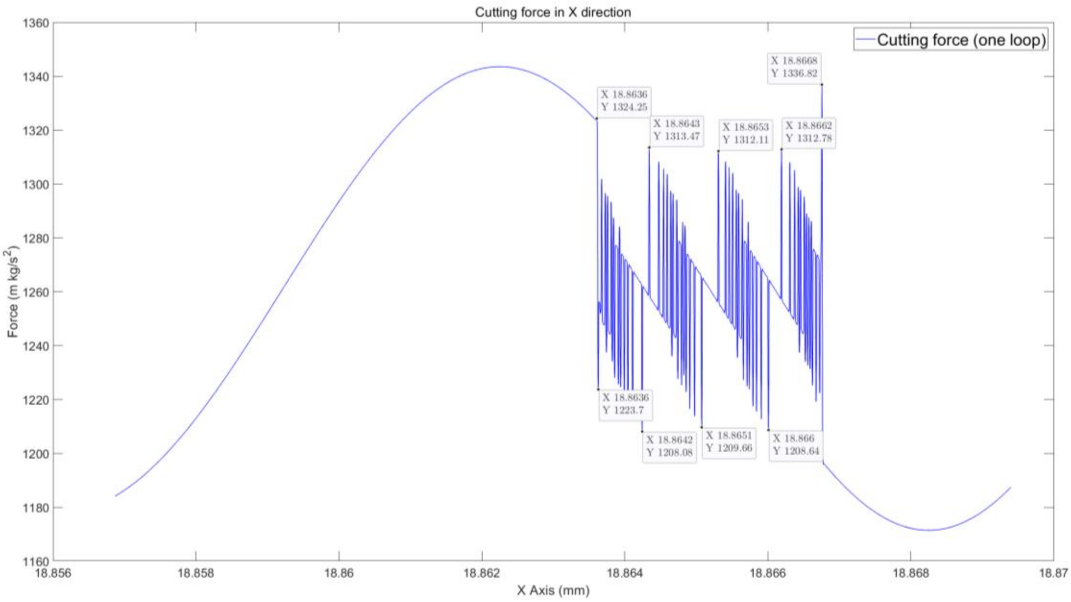

Figure 5.9 Cutting force in one loop: X axis from 18.856 to 18.868 cm.

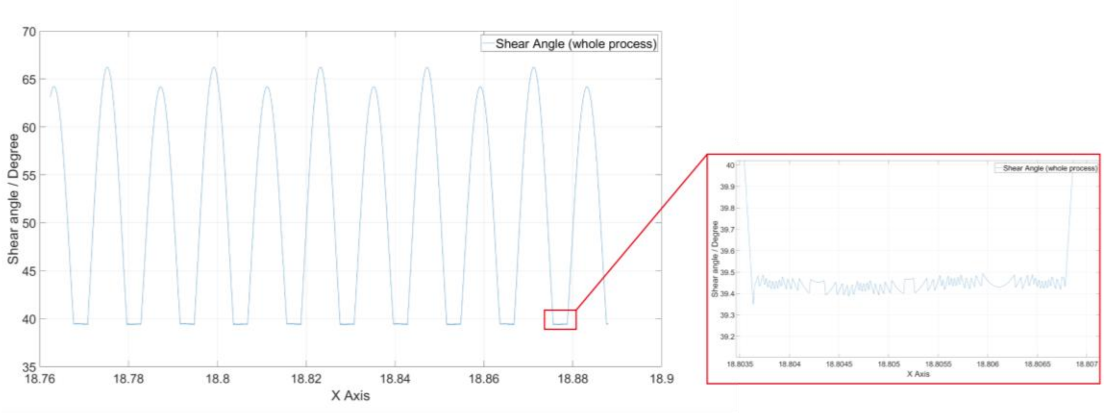

Figure 5.10 Variation of the predicted shear angle during the machining process.

Fig. 5.9 and Fig.5.10 present the variation in shear angle alongside the corresponding cutting force changes. It can be observed that as the practical shear angle decreases, the cutting force initially increases but eventually declines. As the cutter moves into the material removal area, the shear angle changes become more frequent, though still subtle. Notably, the cutting force follows a similar trend. These findings confirm that the developed model effectively tracks the cutter's location based on toolpath data and process parameters associated with material removal in the diamond turning machining process.

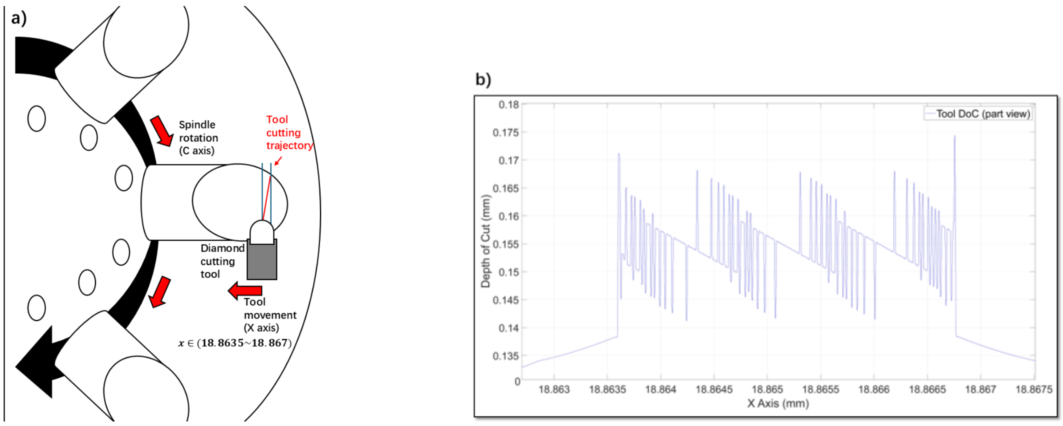

Figure 5.11 a) Schematic of the OAP mirror ultraprecision machining process; b) The resulting plot for tool tips depth of cut in one pass during the machining process.

Fig.5.11(a) illustrates the schematic of the manufacturing process for the OAP mirror. As introduced in the previous Chapter, six OAP mirrors are mounted on the carrier disc, rotating together following the C axis. Meanwhile, the diamond cutting tool performs linear motion along the X axis. Moreover, the cutting tool moves linearly along the Z axis to produce the designed freeform surface. Fig.5.11(b) illustrates the variation in actual depth of cut during a single machining cycle, which demonstrates the material removal volume per tool pass. Based on the previously established mathematical formulation in Equation 5.8, the tool tip position data are first calculated, then by combining the preset parameters of initial tool height to machining. The actual depth of cut is derived from this computational framework.

5.5 Further evaluation and validation of the model

Following the calculation and output of the developed model, a validation process was subsequently conducted to assess the accuracy of the model and identify any potential limitations that may inform future improvements. To evaluate the reliability of the model, a validation method based on the work of Subbiah and Melkote in 2007 [149] is employed to further develop and evaluate the improved Atkins cutting force model, i.e. the proposed dynamic cutting force model applicable to ultraprecision cutting of freeform surfaces. The experimental results presented in their study were used as benchmark data for further comparison and verification of the predictive performance of the proposed dynamic cutting force model [149].

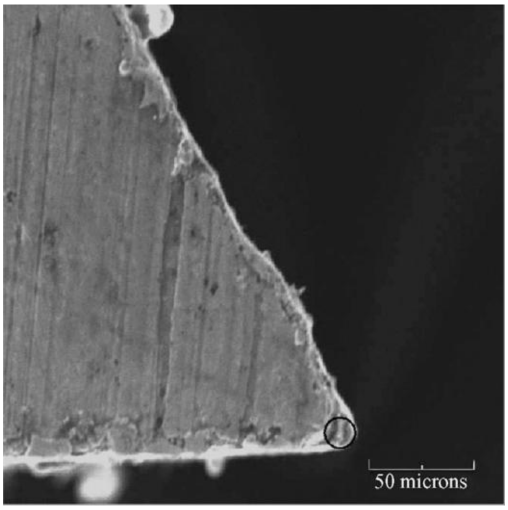

Figure 5.12 The tool cutting edge radius measured using an SEM.

Table 5.2 Experimental conditions [149].

Workpiece	OFHC copper (38.1 mm diameter tube)
Tool	HSS M2 grade
Rake angle	30°
Cutting speed	1.2 m/min (10 rpm spindle speed)
Depth of cut (t_0)	75-200 µm
Cut width	1.1 mm
Edge radius	-7µm

The experiment was conducted on an ultraprecision lathe using an M2-grade high-speed steel (HSS) cutting tool. As illustrated in Fig. 5.12, the tool is featured a clearance angle of 5° and the cutting-edge radius measured at approximately 7 µm. The workpiece material selected for the study was oxygen-free high-conductivity copper (OFHC), with a nominal composition of 99.99% Cu, 0.001% Pb, 0.0001% Zn, and 0.0003% P. The dimensions of the workpiece are an outer diameter of 38.1 mm and a thickness of 1.1 mm.

Cutting forces during the experiment were measured using a quartz three-component Kistler dynamometer (Type 9257B). A summary of the experimental conditions is provided in Table 5.2. In addition to force measurements, chip thickness was recorded at three separate points along the length of the chip using a micrometer with a least count of 2.5 µm. Each set of experiments was repeated three times across a range of depth of cut (DoC) values from 15 µm to 70 µm as listed in Table 5.3 to ensure consistency and repeatability.

Table 5.3 Predicted forces (Fc', Ft') from dynamic cutting force model, measured forces (Fc, Ft) from experimental results and the corresponding uncut chip thickness (t_c)

t_0 (µm)	Fc (N)	Fc' (N)	Ft (N)	Ft' (N)	t_c (mm)
15	21.06	21.1712	13.06	11.7695	0.043
25	24.99	27.1355	14.33	14.5853	0.057
35	30.13	31.9439	16.01	16.6345	0.066
50	37.8	37.3232	16.87	18.1412	0.086
60	41.63	40.4492	16.58	18.8425	0.099
70	48.04	43.7911	18.26	19.9106	0.119

Following the analysis of the above experiment results, all collected data were input into the dynamic cutting force model for validation. A comparison was then conducted between the predicted cutting force values generated by the model and the corresponding experimental measurement data. The results of this comparison are illustrated in Fig.5.13 with the measurement cutting forces from the study (Fc) of Subbiah and Melkote and the corresponding predicted cutting forces from the model (Fc') presented. It can be found that the model accurately simulates the overall trend of the cutting force with minimal error, and demonstrates its capability in cutting force prediction. Similarly, Fig.5.14 presents a comparison between the predicted thrust force (Ft') and the experimentally measured values (Ft). The results illustrate their strong correlation, which further confirms the validity and reliability of the dynamic cutting force model developed.

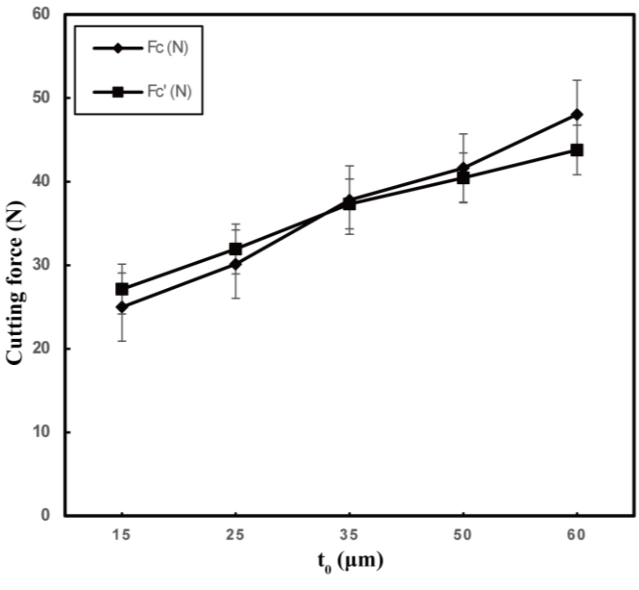

Figure 5.13 Comparison between the measured (Fc) and predicted (Fc') cutting force variation against the corresponding DoC (t_0).

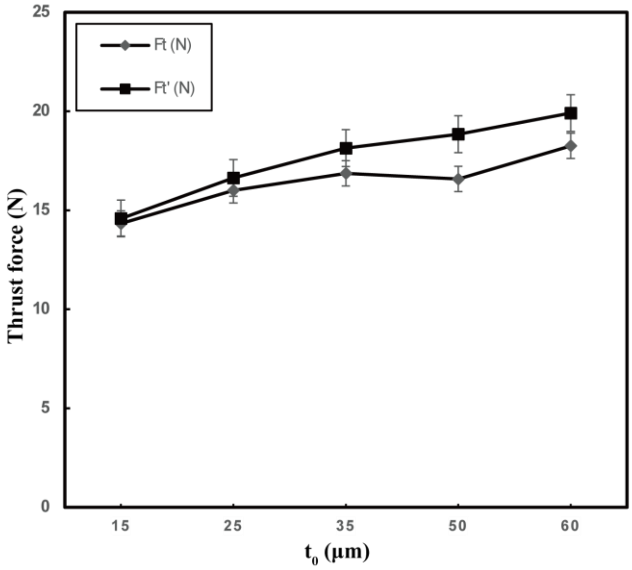

Figure 5.14 Comparison between the measured (Fc) and predicted (Fc') thrust force variation with corresponding DoC (t_0).

The shear angle values calculated using the dynamic cutting force model were also evaluated by comparing the results with the experimentally derived values based on chip thickness (t_c) measurements, as well as those predicted by Atkins model. The comparative results are presented in Fig.5.15. In the presented model, the shear angle is computed using Merchant's model (Equation 5.2). The results show that the model's predictions are closely aligned with the measured shear angles, while Atkins model demonstrates a better capability to capture the overall trend in shear angle variation. This suggests that although Merchant's model provides reasonably accurate shear angle values, Atkins model may offer superior predictive capability in terms of trend representation.

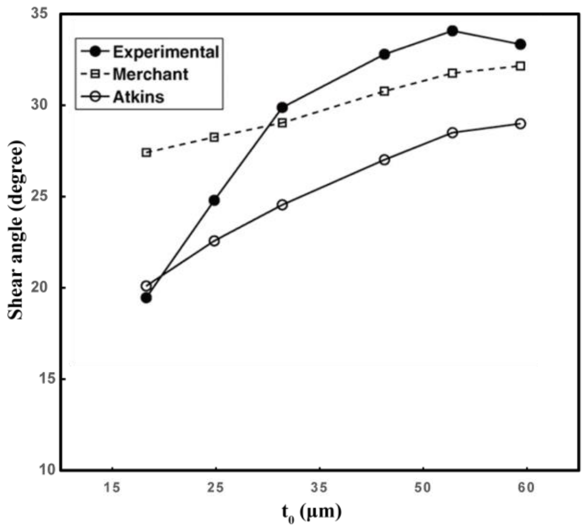

Figure 5.15 Comparison between the shear angle variation with corresponding DoC – experimental, Merchant model (our model method) and Atkins model.

In this research work, the dynamic cutting force model developed was further evaluated and validated through orthogonal cutting experiments on oxygen-free high conductivity copper (OFHC) as published [149]. The experimental cutting trials were conducted at low cutting speeds to minimize strain-rate and temperature effects. The results demonstrate that the model performs well in comparison with experimental data including cutting forces, shear angle, and coefficient of friction. Comparative analysis between the predicted and measured values of both cutting and thrust forces illustrates that the model effectively captures the overall trend of cutting force variation throughout the cutting process, while also provides reliable quantitative predictions. These findings support the model's applicability for ultraprecision machining of freeform surfaces under similar cutting conditions.

5.6 Conclusions

This chapter presents the characterization ultraprecision machining process on various aspects. Theoretical analysis, simulations and experiments are carried out to investigate the cutting force variation during the tooling process. The research achievements are concluded substantially as below.

In light with the cutting force model proposed by Atkins, and in response to the increasing demands of freeform surface manufacturing, a dynamic cutting force model has been developed. This model considers the influence of cutting angles and the corresponding depth of DoC, utilizing machine toolpath data. To ensure the model accurately simulates the chip formation mechanisms, the data used is derived from the machine toolpath rather than a CAD model. By calculating the practical shear angle, the relative distances between each cutter location point, and the practical DoC, the cutting force at each toolpath point can be calculated by incorporating these parameters.

Chapter 6

Assessment of FSO surface texture characteristics using 3D surface parameters and the virtual optics model

6.1 Introduction

The diamond turning process is often referred to as deterministic machining due to its high precision and accuracy, capable of producing surface roughness at the nanometric level. However, surface roughness alone may not fully characterize a surface in all aspects, particularly in certain specialized scenarios, such as machining optical components. For example, in some production cases, surface roughness is within acceptable limits, issues with the optical performance of the surface may still arise. A notable defect is the appearance of rainbow-like colors on the surface, which is often undesirable for free-space optical components. These defects can result from various factors during machining, including tool wear, temperature fluctuations, and vibrations within the machining system. While the surface roughness might remain within acceptable ranges, these factors can compromise the surface texture quality, ultimately affecting optical performance. Therefore, it is essential to implement a comprehensive, integrated approach for assessing the surface quality of freeform optical components.

This chapter investigates the intrinsic relationship between the surface texture aspect ratio of freeform optical components and their functional performance. To explore this relationship, interferometric techniques are employed to observe the interference fringes generated on the surfaces of selected freeform optical components. By analyzing these interference fringes and patterns, it becomes possible to quantify the surface texture aspect ratio and correlate it with functional performance metrics. The findings of this study provide valuable insights for optimizing the design and manufacturing processes of freeform optics, enabling the development of enhanced freeform surfaces with improved functional performance for various applications. Moreover, a comprehensive and integrated approach for assessing the quality of FSO surfaces by constructing a virtual optics model has been proposed in this chapter.

6.2 Surface topography characteristics of the freeform surface generated by UPM

According to the introduction in the previous chapter of UPM, the primary characteristic of the SPDT UPM process is that it does not require any additional post-machining processes, such as polishing. The surface produced by the diamond turning process closely replicates the designed form and achieves nano-level, high-quality surface roughness. As a result, the surface topography resulting from the material removal process in UPM is influenced by factors such as the toolpath, material swelling and recovery, tool/workpiece vibration, and material defects, including cracks, fractures, and other imperfections. Observing these characteristics using nano-level optical surface measurement technologies, such as white light interferometry, is highly beneficial for identifying potential defects that may occur during the material removal process. While polishing can improve surface roughness and significantly enhance production efficiency, this step is typically integrated into the FSO production lines in the optics industry.

6.2.1 Experiments design and setup

In the case of approach introduced in the optics industry with efficiency consideration, a fly-cutting machining process is first employed to remove the majority of the material and create a general shape of the surface. The workpiece is then transferred to a fast-tool machining process for high-precision shaping to achieve the designed surface. Finally, the optical component undergoes polishing to further reduce surface roughness. Fig.6.1(a) and 6.1(b) show the ultraprecision machining equipment and polishing machine respectively and Fig.6.1(c) shows the Zygo NewView 8000 white light interferometer used to observe the surface topography. This method greatly improves production efficiency while maintaining acceptable optical surface quality. However, there is still have challenges remained in this production process. Such as the deviation in the resulting surface shape. Although state-of-the-art research into freeform surface polishing has introduced high-precision polishing processes that follow the designed curvature of the surface, along with compensation algorithms for polishing toolpath generation, some inevitable deviations in surface shape still occur. These deviations can compromise the optical performance of the surface.

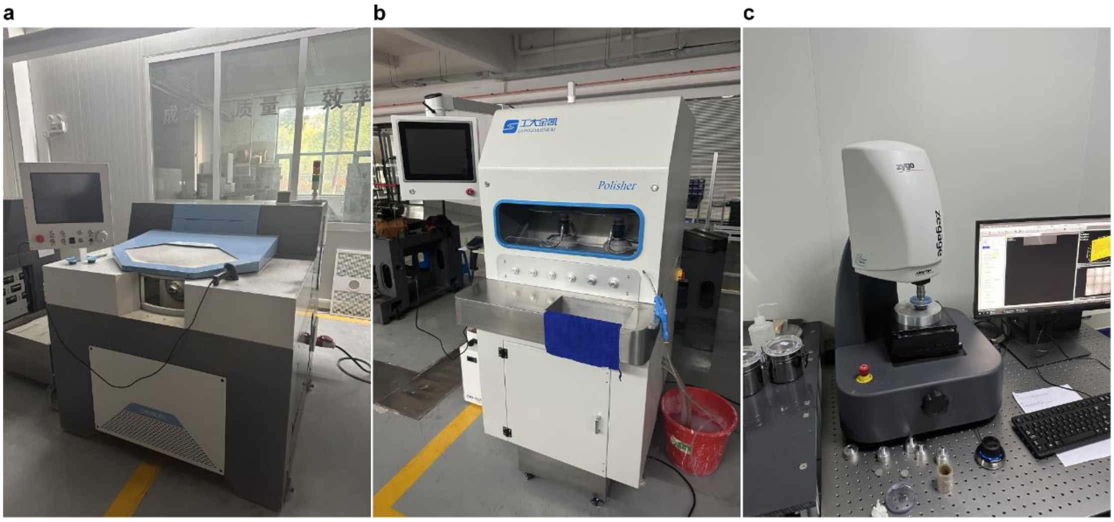

Figure 6.1 Machines been used to investigate the surface topography of freeform surface produced by machining process and polishing process. a) freeform surface turning milling compound machine tool; b) semi-automatic polishing machine; c) Zygo NewView 8000 white light interferometer.

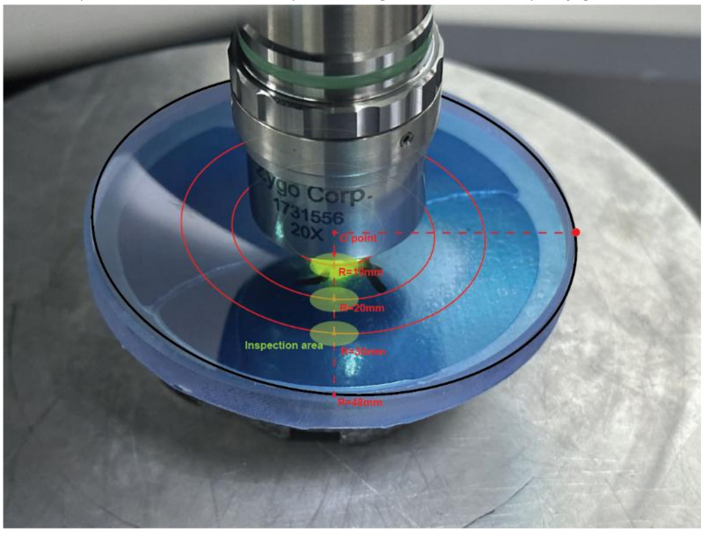

Figure 6.2 Schematic of the observation.

In the industrial manufacturing of FSO, most surface topography characteristics are removed during the polishing process, making it challenging in research aspect to analyze the machining process based on surface topography. Fig.6.2 illustrates the observed surface topography characteristics using a Zygo NewView 8000 white light interferometer equipped with a high-speed camera and a 20× Mirau objective lens. The inspection compares the surface topography of the workpiece after machining and after polishing. The experiment was conducted on a varifocal lens designed with a 400B spherical power in the distance area and an additional 100B power. The lens was initially machined using the SPDT process on the machine shown in **Fig. 6.1(a)**. Surface topography observations were performed on pre-selected areas using the white light interferometer. The lens was then sent for polishing, and observations were repeated on the same surface areas post-polishing. The schematic of the observation setup is shown in **Fig. 6.2**. The lens has a radius of 48 mm, and the material of the lens blank is PMMA. Inspection areas were selected along the toolpath, observing locations spaced at 10 mm intervals.

Table 6.1 Resulting data by using white light interferometer observing surface produced by machining and polishing respectively.

LOCATION SELECTS	TOPOGRAPHY PARAMETER	AFTER MACHINING PROCESS	AFTER POLISHING PROCESS
O POINT	Sphere Radius	209.957	170.146
	Sq (nm)	91.494	27.393
	S_{tr}	0.82	0.85
	PV (μm)	10.569	11.059
R = 10 MM	Sphere Radius	205.421	260.691
	Sq (nm)	258.787	367.353
	S_{tr}	0.41	0.78
	PV (μm)	49.309	65.41
R = 20 MM	Sphere Radius	213.117	254.663
	Sq (nm)	274.978	248.165
	S_{tr}	0.48	0.52
	PV (μm)	32.565	52.968
R = 30 MM	Sphere Radius	171.258	255.831
	Sq (nm)	312.522	286.961
	S_{tr}	0.51	0.91
	PV (μm)	44.541	74.04
R = 40 MM	Sphere Radius	179.785	374.334
	Sq (nm)	305.898	314.434
	S_{tr}	0.62	0.94
	PV (μm)	58.953	110.403

6.2.2 Results, analysis and discussion

Fig.6.3 presents the trend line graph which propose a batter view of the characteristics of freeform surface after machining and polishing, followed by Fig.6.3(a), there is a significant deviation of the sphere radius when surface produce after polishing, due to the polishing process is set to start from out to center of the surface, so it can be observed that with the observation location to the outside of the surface, the deviation of the sphere radius has been get larger. Fig.6.3(b) illustrates the comparison of Str value when surface produced by different process, by the graph it can be observed that the Str value of surface after polishing constant larger than Str value of surface after machining, which indicate that the surface after polishing process is more isotropic due to the machining toolpath has been erased. Fig.6.3(c) presents the surface roughness comparison, which the roughness is getting less after the optics been polished. Last but not least is the Peak-valley distance proposed by Fig.6.3(d), which leads to a higher value of polishing, it can be noticed that the trend of the distance have high imitation with the trend of sphere radius.

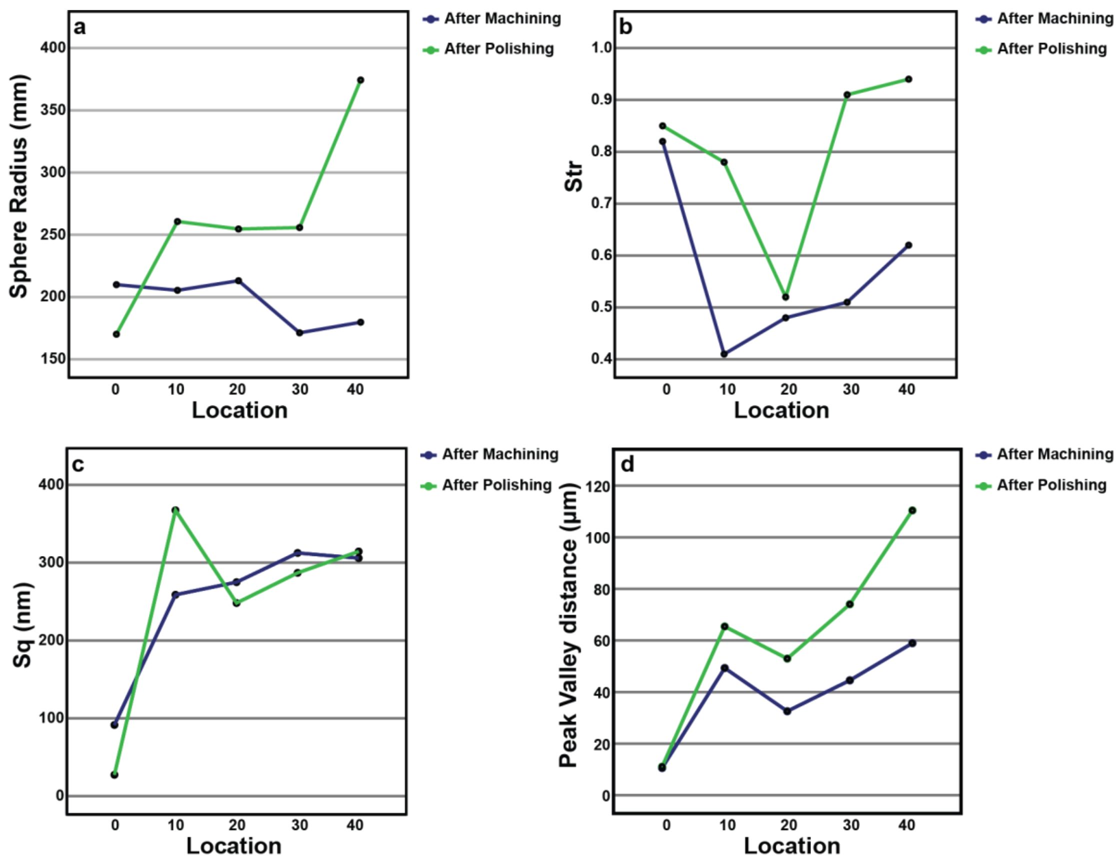

Figure 6.3 Trend line graph illustrates a continuous trend of values for the process after machining and after polishing respectively. a) comparison of sphere radius value; b) comparison of surface texture aspect ratio; c) comparison of root-mean-square roughness; d) comparison of Peak Valley distance.

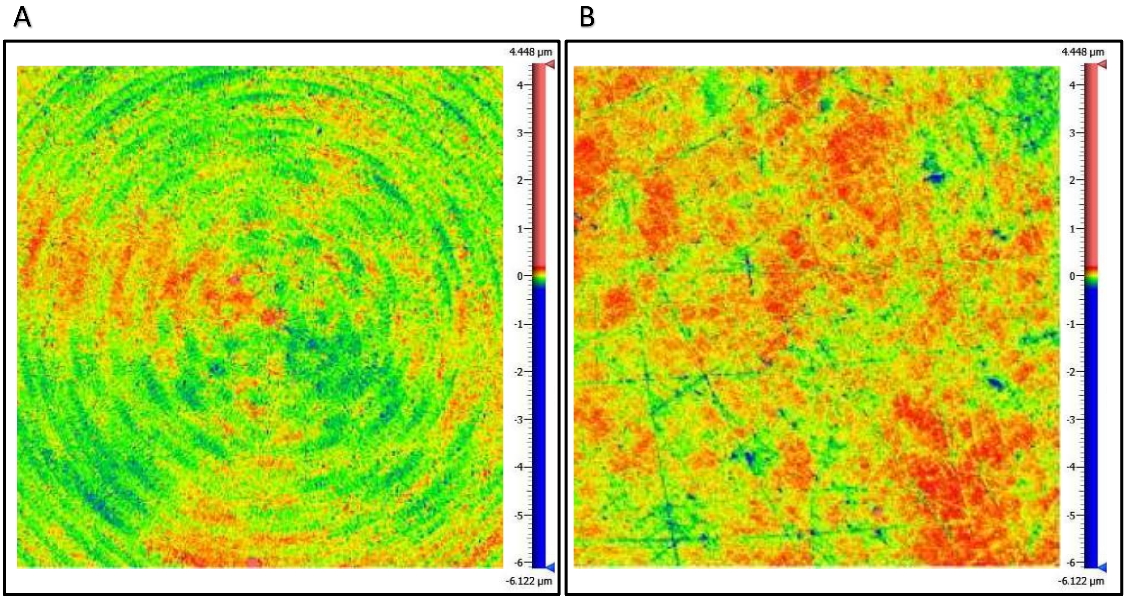

Figure 6.4 Measurement result comparison of the optical surface with the material PMMA before and after polishing. a) Surface topography measured after machining; b) Surface topography measured after polishing.

The experiment based on a discussion of the influence of poshing process to a freeform surface produce by SPDT diamond turning machine, and by the result data and the trend line proposed, it can be observed that the polishing process can highly influence the surface topography characteristic and surface sphere radius. Moreover, polishing process can erase majority of the toolpath of the SPDT process remained. Fig.6.4 presents the screenshot of the surface topography by white light interferometer when observing the O point of the lens, Fig.6.4(a) presents a 3D surface measurement result of the center point of a freeform optical surface after machining, Fig.6.4(B) presents the result of the surface topography at the same position after polishing process. Fig.6.4 gives a more intuitive view of the differences between the surface produced by polishing and machining.

Followed by the conclusion of the experiment, it can be observed that the characteristic of the surface topography is closely relative to the machined toolpath remained on the surface. Therefore, we proposed a theory that the texture of the surface in diamond turning machining process may highly reflect the toolpath on the surface, which makes it contains more meaning than the surface produced by the traditional method.

6.3 Correlation analysis of 3D surface parameters and optics functional performance

A FSO surface topography produced by UPM contribute by machined toolpath, swelling and recovery of the material, and tool vibration induced wavy, material pile-up, etc [82]. The correlation analysis is developed to investigate the correlation between FSO optical performance and its corresponding surface topography characteristics, particular for surface texture, surface roughness, and peak-valley distance of the surface. The result of the analysis is essential for developing the virtual model construction. As it exhibits on Fig.6.3, to find a representative surface to analysis, a selection criterion should firstly in used. The object surface should be firstly identified as a diamond-turning machined freeform surface with high quality of surface roughness. Subsequently, the selected surface is required to exhibit optical error phenomena, such as the presence of rainbow-colored strips. Moreover, the selected object surface should encompass comprehensive information regarding the cutting process for in-depth analysis, which including the designed profile data, machine cutting toolpath data, and the detailed information about the machine process.

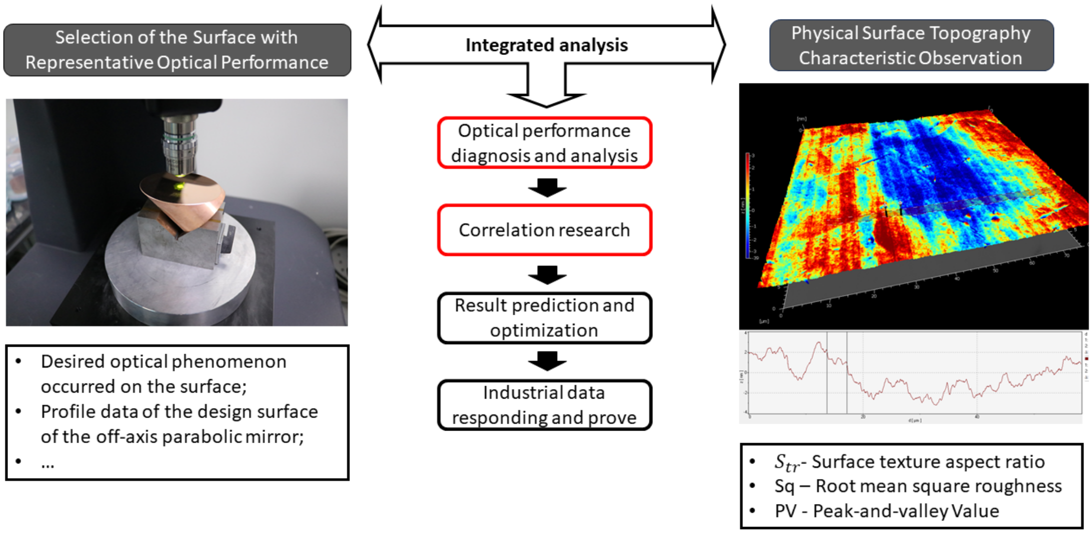

Figure 6.5 Flowchart for illustrate the integrated analysis approach for ultraprecision machined freeform optic surface.

By comparing the topography of the error phenomena regions to one without optical errors (with same design profile data, machining toolpath, and under the same machining conditions), a correlation analysis is conducted. The primary objective of this analysis is to analysis the intricate relationship between nano-level variations in surface topography and their consequential impact on the optical performance of the surface. The result of correlation analysis could furtherly develop the understanding of the connection between the variations in cutting force, followed by changes in freeform surface curvature, and the resulting alterations in optical performance. And finally, the result of this research can be utilized to predict and assess the functional performance of a freeform by analysis cutting force variation in machining process.

6.3.1 Experiment setup and procedures

The proposed hypothesis for this experiment is that a correlation exists between nano-level surface topography characteristics and the optical performance of FSO. To evaluate and validate this hypothesis, a series of machining trials were conducted on the MOORE Nanotech 250 UPL ultra-precision SPDT machine. The schematic of the diamond tool inserts used in the experiment is shown in Fig. 6.6, which includes detailed parameters. As depicted in Fig. 6.6, the tool wear set consists of a natural diamond turning tool with a tool radius of 0.332 mm (N-R0.330 mm), measured using a Scanning Electron Microscope. The tool has a 60° included angle, a 0° rake angle, and a 15° primary clearance. The machining process type used is STS with a feed rate of 0.2777 μm on the X-axis, the same process used to produce the off-axis parabolic mirror discussed in Chapter 5, where the mirror was mounted on a carrier disc with a diameter of Ø240 mm for efficiency considerations. Similarly, the correlation experiment was conducted on a freeform surface mirror with a diameter of Ø50 mm, and the material selected was TU2 copper.

Tool Code	N-R0.330m LECo 100-C4-60 i1
Diamond	Natural ND01 or ND02
Rake Angle (°)	0° (in 0° pocket toolholder)
Radius (mm)	0.330mm ±0.035mm
Waviness (μm)	<0.250μm over 100° of arc
Cutting Arc (°)	100°
Included Angle (°)	60°
Front Clearance (°)	15° Conical (in 0° pocket toolholder)
Shank Clearance (°)	25° on Insert
Shank (WxHxL – mm)	I1, 55° Insert – Tungsten (DCGW)
Nominal Cutting Height	3.300mm Maximum

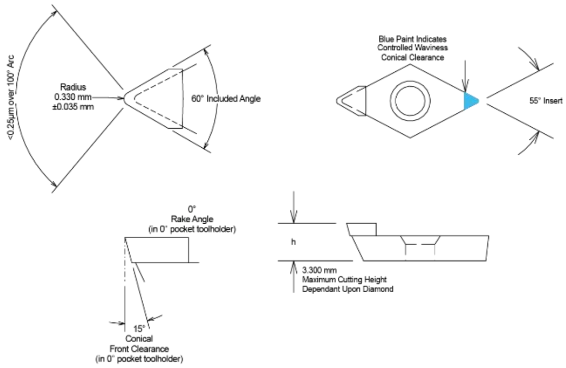

Figure 6.6 Cutting tool conditions.

Fig.6.7(a) illustrates the design and alignment method for an off-axis parabolic mirror. The ultraprecision machining of the mirror was carried out at the ultraprecision machining workshop of the industrial collaborator, GDJK Ltd. Fig.6.7(b) shows the CAD surface features and toolpath simulation for a single off-axis parabolic mirror surface. Additionally, Fig.6.7(c) illustrates the CAD surface and toolpath simulation for machining multiple mirrors simultaneously on the carrier disk.

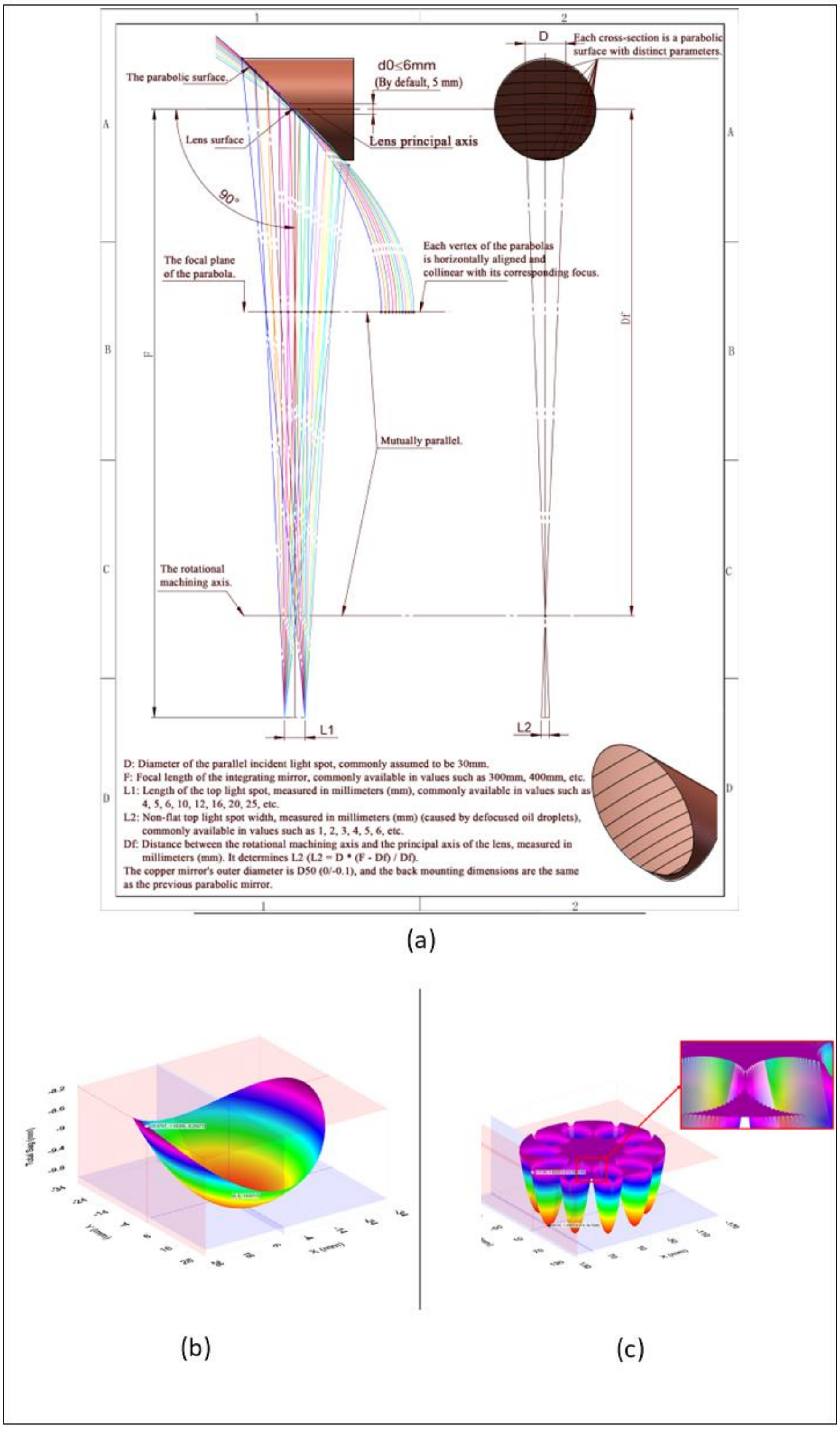

Figure 6.7 The tested off-axis parabolic mirror toolpath simulation and its surface designed center position. a) Method of design and alignment of an off-axis parabolic mirror; b) Single off-axis parabolic mirror surface; c) Toolpath with multiple mirrors machined on the carrier disk.

6.3.2 Observation and data collection

After the machining process, a Zygo NV8000 interferometer was used to observe and analyze the freeform surface topography. The goal was to analyze the correlation between the machining toolpath trajectory and the optical performance of the optics. The location of the detected points was selected with this in mind. Considering the tool motion during the machining process, the toolpath trajectory is expected to be relatively horizontal along the surface rather than circular. Therefore, the surface observation was focused on detecting points along the toolpath direction. This approach provides a more comprehensive view and understanding of the surface texture. Fig. 6.8 shows the selected surface and the method used for observation. The figure reveals distinct interference fringes in the upper portion of the tested surface, while no visible flaws are observed in the lower part. To ensure consistent point selection for further analysis, the horizontal centerline was used as a reference. The midpoint of the centerline was marked as the "O" point (representing zero), with each subsequent point marked at 6 mm intervals for observation. Points located below the O point were marked as negative, while points above were marked as positive. Additionally, 13 more points were selected vertically based on these reference points. Following this methodology, a series of observation experiments were carried out at the detected points along the toolpath trajectory.

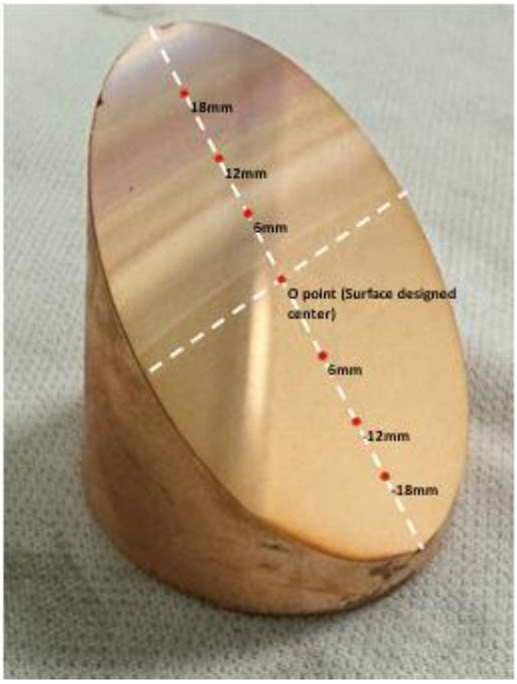

Figure 6.8 Schematic of selection of the inspection points on the surface.

6.3.3 Experiment data output and comparison analysis.

According to the observation experiment, the surface topography data has been collected and organized which are shown in table 6.2. The range of the value of surface texture aspect ratio is 0.01~0.37 which is closer to 0, indicating the surface texture expresses anisotropy.

Table 6.2 3D surface parameters observed in different distance inspection point.

Distance (mm)	Str	PV (μm)	RMS (μm)

-18	0.32	0.958	0.073
-18	0.28	0.425	0.043
-18	0.27	0.27	0.033
-18	0.27	0.321	0.03
-18	0.27	0.381	0.032
-18	0.27	0.367	0.032
-18	0.37	0.52	0.071
-12	0.18	0.169	0.025
-12	0.18	0.172	0.023
-12	0.18	0.185	0.024
-12	0.18	0.214	0.025
-12	0.19	0.221	0.027
-12	0.19	0.266	0.031
-12	0.39	0.39	0.063
-6	0.09	0.148	0.015
-6	0.09	0.102	0.013
-6	0.09	0.093	0.012
-6	0.09	0.095	0.012
-6	0.67	22.388	0.073
-6	0.09	0.14	0.014
-6	0.78	0.472	0.05
6	0.04	1.669	0.099
6	0.01	0.795	0.075
6	0.01	1.093	0.074
6	0.02	1.275	0.086
6	0.06	2.14	0.116
6	0.09	2.213	0.153
6	0.01	1.146	0.11
12	0.06	2.252	0.219
12	0.01	2.033	0.153
12	0.01	2.061	0.145
12	0.04	1.997	0.197
12	0.07	2.391	0.228
12	0.09	2.521	0.251
12	0.01	2.243	0.176
18	0.1	7.701	0.202
18	0.02	2.941	0.193
18	0.03	2.513	0.199
18	0.02	2.588	0.206
18	0.01	2.533	0.214
18	0.01	2.946	0.221
18	0.01	2.66	0.215

Fig.6.9 proposed a more comprehensive view of the comparison between each parameter. Fig.6.9(a) presents a comparison of the mean values of Str, PV value, and RMS value at different distances. It is evident that the areas located at distances 6.00mm, 12.00mm, and 18.00mm (upper position of the observed surface) exhibit significantly higher PV values and lower Str values. On the other hand, there is no substantial difference in the RMS values across the entire surface. Fig.6.9(b) provides a more detailed analysis of the relationship between the PV value and RMS value. From the plot, it can be observed that while there is no noticeable variation in the RMS value changes, there exists a positive correlation between the RMS value and PV value, which implies that higher PV values in the upper portion correspond to higher RMS values, indicating increased roughness at the upper position.

Figures 6(c), and 6(d) illustrate the correlation between Str and PV, as well as Str and RMS. The analysis reveals a notable negative correlation between Str and PV value, and similarly between Str and RMS value. The blue histogram denotes the distribution of Mean Str values, while the red line illustrates the variation in Mean RMS and PV values, respectively. The graphical representations indicate that the surface located at the designed center exhibits the smoothest surface roughness and the lowest PV value. Moreover, the Str values for the upper part of the surface, at distances of 6mm, 12mm, and 18mm, consistently maintain a value of 0.1. In contrast, the Str values in the lower part of the surface vary between 0.3 and 0.8.

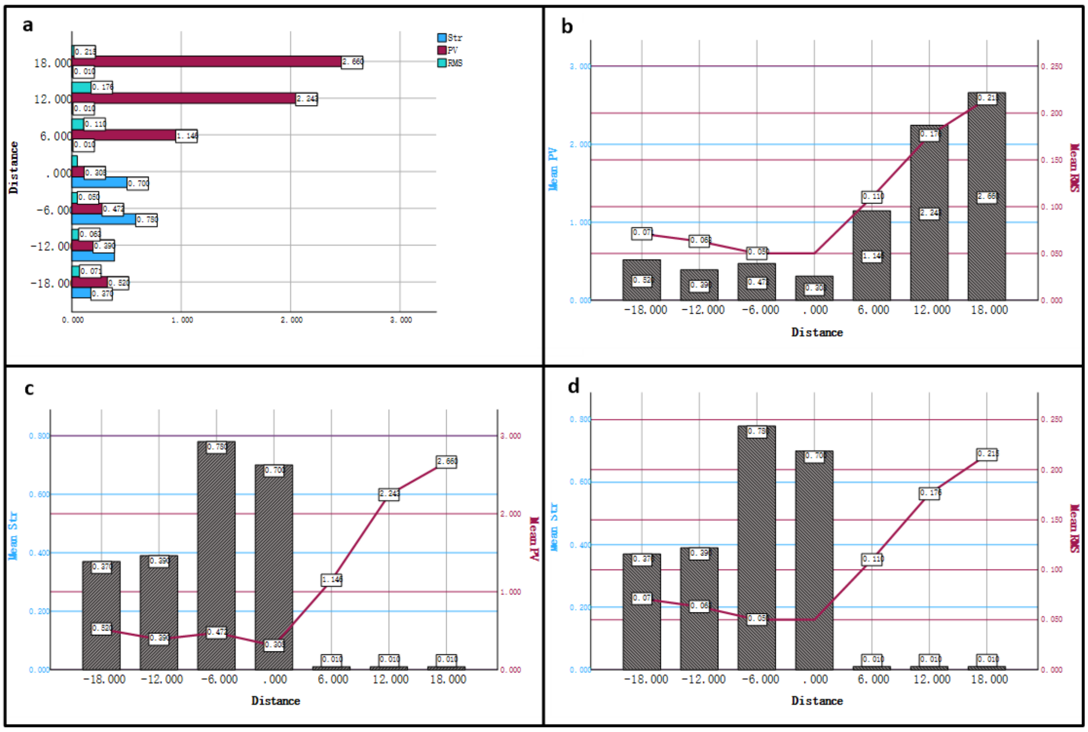

Figure 6.9 a) The result of correlated mean value of Str, PV, and RMS within different distance area; b) Correlation analysis between mean PV and mean RMS value; c) Mean Str vs Mean PV value correlation analysis plot; d) Correlation analysis between mean RMS and mean Str value.

6.3.4 Correlation analysis of FSO topography characteristics with its corresponding optical performance

To investigate the correlations between freeform surface topography characteristics and the selection of inspection area, standard Pearson correlation analysis approach has been employed that results in a numerical value for how well alterations in expression levels of two parameters correlates. This type of analysis will generate a wide variety of correlations between different parameters, but the 3D parameters to the distance value, therefore, the calculation including the correlation between each parameter. Fig.6.10 visualized the correlation result as a heatmap, which provide an intuitive view of the result.

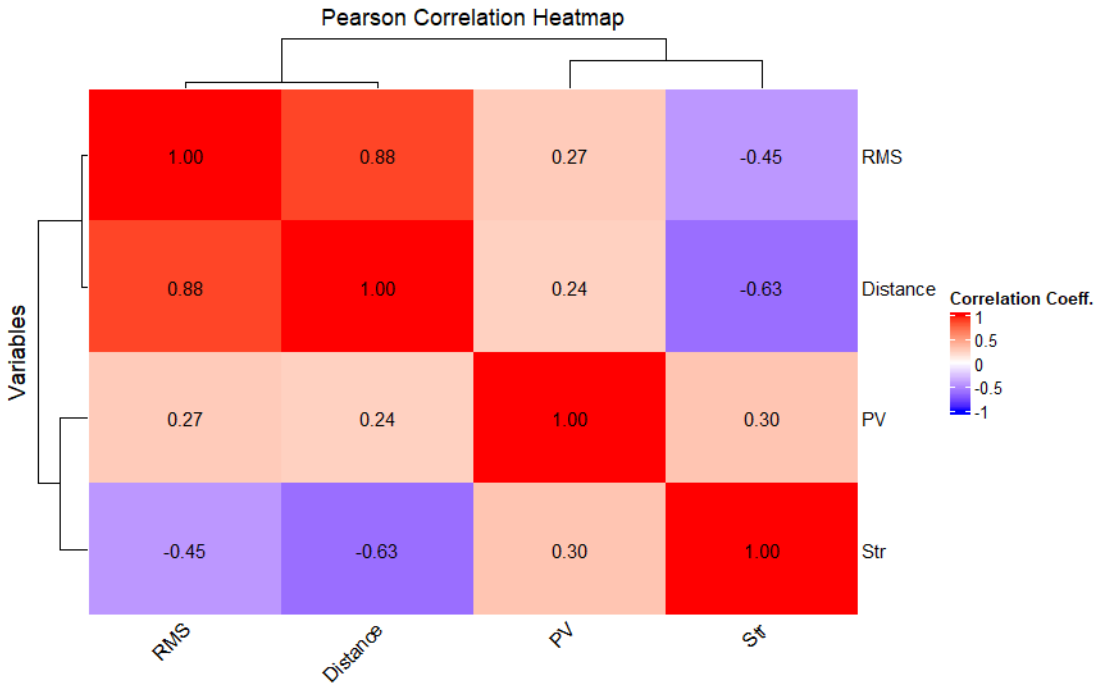

Figure 6.10 Pearson correlation heatmap.

Table 6.3 Table of correlation analysis between each 3D surface parameter.

		Str	PV	RMS	Distance
Str	Pearson Correlation	1	0.301	-0.445**	-0.627**
	Sig. (2-tailed)		0.053	0.003	0.000
	N	42	42	42	42
PV	Pearson Correlation	0.301	1	0.270	0.241
	Sig. (2-tailed)	0.053		0.083	0.124
	N	42	42	42	42
RMS	Pearson Correlation	-0.445**	0.270	1	0.877**
	Sig. (2-tailed)	0.003	0.083		0.000
	N	42	42	42	42
Distance	Pearson Correlation	-0.627**	0.241	0.877**	1
	Sig. (2-tailed)	0.000	0.124	0.000	
	N	42	42	42	42

**. Correlation is significant at the 0.01 level (2-tailed).

Table 6.3 provide a detail result data with Pearson correlation ratio, significant ratio, and the sum of the sample, which the distance value as dependent variable. Followed by the table, it can be observed that the Distance value has a strong positive correlation with surface roughness (RMS, 0.877), moderate negative correlation with surface texture aspect ratio (Str, -0.627) and a weak positive correlation with peak-valley distance (PV, 0.241). Meanwhile, the correlation between each topography parameters has also been analysed. Str value contains relatively high negative correlation with RMS (-0.445), and a weak positive correlation with PV (0.301). And the parameters of peak-valley distance contain weak positive correlation with both Str (0.301) and RMS (0.270).

Due to the distance value is decided by the level of rainbow phenomenon, and has a negative relationship, means that the lower value of the distance indicates that more invisibility of the phenomenon. Which leads to the prove of the hypothesis of the experiment: 1, The relation between nano-level surface topography characteristic and the optical performance is correlate but independent. 2, There is a relatively high positive correlation between surface texture aspect ratio to the corresponding optical performance, and a strong negative correlation between surface roughness and the optical performance.

6.4 Conclusions

This chapter presents the characterisation of FSO optical performance influenced by nano-level surface topography characteristics in UPM perspective. Theoretical analysis, experiments, and correlation analysis are carried out to investigate the correlation between FSO surface topography characteristics and its corresponding optical performance. The research achievements are concluded substantially as below.

To investigate the nano-level surface topography machined by UPM and its corresponding optical performance, there is two steps in this investigation which leads to two experiments. The first is to investigate the feature of nano-level surface topography in UPM and its comparison with the tradition process sequence in industrial perspective. Therefore, the first experiment with the purpose of investigating the differences of surface topography produced by SPDT machine and polishing process has been proposed. According to the theoretical results and experimental result, it can be observed that SPDT machined surface topography characteristic by the evidence of the machining process such as remaining machined toolpath, tool mark, and crack during material removal process, etc. And the surface produced by polishing will contains relatively better surface roughness but also induced inevitable deviation in surface curvature, and the machining evidence such machined toolpath, tool marks will no longer exist. The first experiment proved the surface produced by SPDT process will leave the machined toolpath on the surface. Based on this theory, the second experiment has been proposed, which aims to develop the scientific understanding of the correlation between nano-level surface topography and its corresponding optical performance, and furthermore the new approach for retrace back UPM process by the characteristics of surface texture rather than only rely on surface roughness. The detailed conclusions can be drawn as follows:

1. Compare with traditional precision machining techniques, the SPDT UPM can produce a surface with high precision, perfect surface roughness with no need in any further requirements of further process such as polishing. Which leads to the conclusion that the nano-level topography characteristics of UPM contains machined toolpath on the surface which been characterised by 3D surface parameters.

2. In traditional precision machining process, polishing process is inevitable process due to its ability to reduce the roughness of the surface and improve the flatness of the surface. But in the case of FSO manufacturing, the FSO components endured the potential trouble with the deviation of curvature of the surface which may leads to further defect with its optical performance.

3. In the scenario of FSO produced by UPM, the result of correlation analysis indicates that the nano-level surface topography characteristic presents correlation with default of FSO optical performance. In which the surface roughness presents strong negative correlation and surface texture presents relative high correlation and PV value contains weak correlation.

Chapter 7

Conclusions and recommendations for future work

7.1 Conclusions

In this doctoral research, NURBS-based design modelling and analysis for freeform surface optics while considering design for manufacturing, analysis of the optics performance, cutting mechanics and cutting forces modelling in correlation with surface texture generation, characterization of freeform surface topography through multiscale multiphysics modelling and analysis, all in the context of the integrated approach. A scientific understanding of the UPM process for FSO is started from the NURBS based modelling and analysis of the optics surface, design for ultraprecision manufacturing through toolpath generation analysis, ray tracing simulation on optical performance, dynamic cutting force modelling, correlation analysis of surface topography characteristics including surface roughness, peak-valley distance, and surface texture aspect ratio with the default assessment of the FSO, in line with integral design, manufacturing, and functional assessment. The distinct conclusions for this research work can thus be drawn up as follows:

(1) An integrated approach to NURBS-based design modeling and analysis of FSO is presented combined with to a web-based portal development, which is also demonstrated through a case study on varifocal lens design and manufacturing. This approach highlights the full integration of freeform surface modeling and analysis, optics design, the assessment and deterministic manufacturing, and provides an in-depth understanding of the UPM process for FSO. The NURBS-based method emphasizes high precision in surface design and the integration of surface design, modelling and analysis, and the ultraprecision machining processes. Furthermore, the use of NURBS representation ensures precision assurance and consistency in the modelling definition, minimizing potential precision loss during data transfer across different stages of the process.

(2) The ray tracing assessment method for the FSO is established through the combined effort of multiscale multiphysics modelling and analysis, experimental evaluation, and validation in UPM. By incorporating material selection and the detailed NURBS modelling representation, simulations are developed to demonstrate the ability to compute and predict the optical performance prior to the deterministic ultraprecision machining. This renders a reliable baseline for optimal design and modelling processes for FSO.

(3) Dynamic cutting forces modelling in freeform surface ultraprecision machining is developed based on improved Atkins model while considering key parameters of the cutting toolpath, instantaneous chip thickness, depth of cut, spindle speed, material selection, and feed rate, etc. Improved Atkins model focuses on the cutting shear process into three components of shear yield stress, plastic strain, and fracture energy, while the cutting against a dynamic changing freeform surface rather than the flat surface. This modelling development incorporates practical considerations by addressing the constant variations of the surface curvatures and thus the actual depth of cut and shear angle in the cutting process, which enhances the modelling accuracy and applicability for ultraprecision machining of freeform surfaces in particular.

(4) Experimental evaluation and validation are carried out on the dynamic cutting force modelling as developed. The experimental case study is executed on ultraprecision machining of off-axis parabolic mirrors. With comprehensive analysis from design modelling to toolpath generation and ultraprecision machining, both experimental analysis and simulations are further undertaken on cutting forces modelling and their effects on the machined surface characteristics.

(5) The experiment is conducted as part of a case study on the industrial production line of freeform varifocal lenses, but focused on the investigation of the differences in freeform surface topography and characterization after the diamond turning process and the subsequent polishing process respectively. The analysis aims to evaluate the hypothesis that the topography of a freeform lens produced by diamond turning is defined by its form (e.g., curvature radius) and texture parameters (e.g., toolpath traces) rather than solely by the surface roughness. The results of this analysis provide strong evidence to support the proposed correlation analysis between the topography of ultra-precision machined freeform optics and their optical performance.

(6) The investigation into the correlation between nanometric level surface texture aspects and the corresponding optical performance provides an innovative approach to assessment of freeform surface optics. The experimental analysis is conducted using Zygo 3D surface profiler on an off-axis parabolic mirror exhibiting a rainbow phenomenon on its surface. The analysis reveals a strong correlation between the observed rainbow phenomenon and the surface texture aspect ratio S_{tr}.

(7) The conception of the virtual lens is described, which incorporates comprehensive information including the lens surface modeling and analysis, toolpath simulations for machining the surface, ray tracing analysis, cutting force prediction, and surface topography generation and characterization. By adopting the NURBS based representation approach, a unified method is employed across all analyses and simulations, ensuring high precision data transformation consistently and thus the manufacturing accuracy of the optics. The virtual optics is designed to fully represent the resultant surface quality of optics in all performance aspects. The outcomes of the virtual model can be used to optimize the design and modeling of optical components, to enhance the alignment between the optical design and manufacturing processes, and to further improve toolpath generation through cutting forces compensation.

7.2 Contributions to knowledge

The major contributions span out from this doctoral research are highlighted below, including:

(1) A web-based e-portal is developed for integrating surface modelling and analysis, surface design, and ray tracing assessment. The e-portal bridges the gaps between ophthalmic optics design and ultraprecision manufacturing against the mass customization requirement in digital era, and further significantly improve the design agility and manufacturing responsiveness.

(2) Innovative dynamic cutting force modelling is developed by considering the constant variations in freeform surface curvatures. The model also incorporates multiple factors such as material selection, tool geometry, and the process variables. This enhanced modelling can predict cutting force variations in ultraprecision machining of freeform surfaced optics.

(3) Theoretical analysis is conducted to establish the relationship between freeform surface texture aspect and the optical performance of optics. This analysis provides evidence that the surface texture of the ultraprecision diamond turned surface is highly characterized by the residual toolpath.

(4) The holistic experimental study is carried out to explore the conception and construction of virtual models in the ultra-precision machining process of freeform surface optics. The findings contribute to the optimization of the machining process and provide a scientific understanding of the intrinsic relationships among the optics design and analysis, virtual assessment and ultraprecision manufacturing, particularly in the high precision computational environment.

7.3 Recommendations for future work

The recommendations for future work can be summarized in the following aspects:

(1) Further Development of the e-Portal Application

In this doctoral study, the development and application of the e-portal were preliminarily focused on the varifocal lens manufacturing. However, the fundamental logic of the e-portal development is applicable to the entire FSO manufacturing field. Conducting multiple case studies across different FSO applications would be beneficial for further enhancing the e-portal functionality and adaptability, which will be one of key recommendations for future research and development.

(2) Enhancement of the Dynamic Cutting Forces Model in Cutting Freeform Surfaces

The current dynamic cutting force modelling still requires further refinement particularly through a variety of industrial FSO components, while it does not yet incorporate multiscale factors such as materials variation and dynamics effects of a fast tool servo system. Additionally, future research should focus on using simulation results and boundary conditions better to construct a virtual surface with simulated residual texture, and addressing the challenges of accurately representing surface characteristics.

(3) Further Industrial validation of the Virtual Model

The proposed method of constructing a virtual model to represent and predict the resulting optical surface requires further industrial experimental evaluation and validation. This includes comparative analyses between the virtual model and the actual UPM-machined surface, focusing on surface texture and topography characteristics, optical performance, and the dynamic cutting forces in-process observed.

References

[1] K. Manjunath, S. Tewary, N. Khatri, and K. Cheng, ‘Monitoring and Predicting the Surface Generation and Surface Roughness in Ultraprecision Machining: A Critical Review’, *Machines*, vol. 9, no. 12, Art. no. 12, Dec. 2021, doi: 10.3390/machines9120369.

[2] D. Huo and K. Cheng, ‘Micro Cutting Mechanics’, in *Micro-Cutting*, John Wiley & Sons, Ltd, 2013, pp. 19–44. doi: 10.1002/9781118536605.ch2.

[3] J. P. Schaefer, ‘Advanced metal mirror processing for tactical ISR systems’, in *Airborne Intelligence, Surveillance, Reconnaissance (ISR) Systems and Applications X*, SPIE, May 2013, pp. 18–27. doi: 10.1117/12.2015496.

[4] Zhou, Tianfeng, et al. "Aspheric lens processing of chalcogenide glass via combined PGM-SPDT process." The International Journal of Advanced Manufacturing Technology 120.9 (2022): 5855-5864. Accessed: Jan. 16, 2025. [Online]. Available: https://link.springer.com/article/10.1007/s00170-022-09112-4

[5] J. Dahlmanns, A. Völl, R. Wester, J. Stollenwerk, P. Loosen, and C. Holly, ‘Simulation and design of a Fresnelized freeform optic for a head-up display’, 2021, doi: 10.1117/12.2600221.

[6] Cai, Hongbin, et al. "Study on optical freeform surface manufacturing of progressive addition lens based on fast tool servo." IOP Conference Series: Earth and Environmental Science. Vol. 69. No. 1. IOP Publishing, 2017. Accessed: Jan. 16, 2025. [Online]. Available: https://iopscience.iop.org/article/10.1088/1755-1315/69/1/012130/meta

[7] Khaghani, Ali, and Kai Cheng. "Investigation of a dynamics-oriented engineering approach to ultraprecision machining of freeform surfaces and its implementation perspectives." Nanotechnology and Precision Engineering 4.4 (2021). Accessed: Jan. 16, 2025. [Online]. Available: https://pubs.aip.org/tu/npe/article/4/4/043002/626870

[8] Yip, Wai Sze, et al. "The state-of-art review of ultra-precision machining using text mining: Identification of main themes and recommendations for the future direction." *Wiley Interdisciplinary Reviews: Data Mining and Knowledge Discovery* 14.1 (2024): e1517. Accessed: Dec. 10, 2024. [Online]. Available: https://wires.onlinelibrary.wiley.com/doi/full/10.1002/widm.1517

[9] Y. Wei, P. Zhai, X. Chen, and L. He, ‘Study on Design and Diamond Turning of Optical Freeform Surface for Progressive Addition Lenses’, *Math. Probl. Eng.*, vol. 2020, no. 1, p. 2850606, 2020, doi: 10.1155/2020/2850606.

[10] C. Bösel and H. Gross, ‘Compact freeform illumination system design for pattern generation with extended light sources.’, *Appl. Opt.*, vol. 58 10, pp. 2713–2724, 2019, doi: 10.1364/AO.58.002713.

[11] C. Canavesi, W. J. Cassarly, and J. P. Rolland, ‘Target flux estimation by calculating intersections between neighboring conic reflector patches’, *Opt. Lett.*, vol. 38, no. 23, p. 5012, Dec. 2013, doi: 10.1364/OL.38.005012.

[12] H. Ries and J. Muschaweck, ‘Tailored freeform optical surfaces’, *JOSA A*, vol. 19, no. 3,

pp. 590–595, Mar. 2002, doi: 10.1364/JOSAA.19.000590.

[13] J. Chaves, *Introduction to Nonimaging Optics*. Boca Raton: CRC Press, 2008. doi: 10.1201/9781420054323.

[14] M. Mirhosseini *et al.*, ‘High-dimensional quantum cryptography with twisted light’, *New J. Phys.*, vol. 17, no. 3, p. 033033, Mar. 2015, doi: 10.1088/1367-2630/17/3/033033.

[15] M. Chrisp, L. Petrilli, M. Echter, and A. Smith, ‘Freeform surveillance telescope demonstration’, in *MSS Parallel Conference, MSS by BRTRC Federal Solutions under contract (Ed)*, 2019, pp. 2769–2775.

[16] J. Reimers, A. Bauer, K. P. Thompson, and J. P. Rolland, ‘Freeform spectrometer enabling increased compactness’, *Light Sci. Appl.*, vol. 6, no. 7, pp. e17026–e17026, Jul. 2017, doi: 10.1038/lsa.2017.26.

[17] R. Geyl, E. Ruch, R. Bourgois, R. Mercier-Ythier, H. Leplan, and F. Riguet, ‘Freeform optics design, fabrication and testing technologies for Space applications’, Jul. 2019, p. 24. doi: 10.1117/12.2535944.

[18] E. M. Schiesser, A. Bauer, and J. P. Rolland, ‘Effect of freeform surfaces on the volume and performance of unobscured three mirror imagers in comparison with off-axis rotationally symmetric polynomials’, *Opt. Express*, vol. 27, no. 15, p. 21750, Jul. 2019, doi: 10.1364/OE.27.021750.

[19] S. Cui *et al.*, ‘Silicone optical elements for cost-effective freeform solar concentration’, *Opt. Express*, vol. 27, no. 8, pp. A572–A580, Apr. 2019, doi: 10.1364/OE.27.00A572.

[20] L. Wei, Y. Li, J. Jing, L. Feng, and J. Zhou, ‘Design and fabrication of a compact off-axis see-through head-mounted display using a freeform surface’, *Opt. Express*, vol. 26, no. 7, pp. 8550–8565, Apr. 2018, doi: 10.1364/OE.26.008550.

[21] Liu, Yan, Yanqiu Li, and Zhen Cao. ‘Design method of off-axis extreme ultraviolet lithographic objective system with a direct tilt process.’ *Optical Engineering* 54.7 (2015): 075102-075102. Accessed: Dec. 11, 2024. [Online]. Available: https://colab.ws/articles/10.1117%2F1.OE.54.7.075102

[22] C. Yoon, A. Bauer, D. Xu, C. Dorrer, and J. P. Rolland, ‘Absolute linear-in-k spectrometer designs enabled by freeform optics’, *Opt. Express*, vol. 27, no. 24, pp. 34593–34602, Nov. 2019, doi: 10.1364/OE.27.034593.

[23] X. Jiang and P. J. Scott, *Advanced metrology: freeform surfaces*. London: Elsevier Academic Press, 2020.

[24] K. Garrard, T. Bruegge, J. Hoffman, T. Dow, and A. Sohn, ‘Design tools for freeform optics’, presented at the Optics & Photonics 2005, P. Z. Mouroulis, W. J. Smith, and R. B. Johnson, Eds., San Diego, California, USA, Aug. 2005, p. 58740A. doi: 10.1117/12.617680.

[25] K. P. Thompson and J. P. Rolland, ‘Freeform Optical Surfaces: A Revolution in Imaging Optical Design’, *Opt. Photonics News*, vol. 23, no. 6, pp. 30–35, Jun. 2012, doi: 10.1364/OPN.23.6.000030.

[26] J. Ye, L. Chen, X. Li, Q. Yuan, and Z. Gao, 'Review of optical freeform surface representation technique and its application', *Opt. Eng.*, vol. 56, p. 1, Nov. 2017, doi: 10.1117/1.OE.56.11.110901.

[27] F. Z. Fang, X. D. Zhang, A. Weckenmann, G. X. Zhang, and C. Evans, 'Manufacturing and measurement of freeform optics', *CIRP Ann.*, vol. 62, no. 2, pp. 823–846, 2013, doi: 10.1016/j.cirp.2013.05.003.

[28] K. J. Stout and L. Blunt, *Three-dimensional surface topography*, 2nd ed. London: Penton Press, 2000.

[29] P. Yoder and D. Vukobratovich, *Opto-Mechanical Systems Design, Two Volume Set*, 4th ed. Boca Raton: CRC Press, 2018. doi: 10.1201/9781315217635.

[30] K. J. Kasunic, *Optomechanical Systems Engineering*. John Wiley & Sons, 2015.

[31] C. Henri, 'Anamorphotic lens system and method of making the same', US1962892A, Jun. 12, 1934 Accessed: Dec. 01, 2024. [Online]. Available: https://patents.google.com/patent/US1962892A/en

[32] K. P. Thompson and J. P. Rolland, 'Freeform Optical Surfaces: A Revolution in Imaging Optical Design', *Opt. Photonics News*, vol. 23, no. 6, pp. 30–35, Jun. 2012, doi: 10.1364/OPN.23.6.000030.

[33] B. H. James, 'Lens of variable focal power having surfaces of involute form', US2475275A, Jul. 05, 1949 Accessed: Dec. 01, 2024. [Online]. Available: https://patents.google.com/patent/US2475275A/en

[34] M. Peloux and L. Berthelot, 'Optimization of the optical performance of variable-power and astigmatism Alvarez lenses', *Appl. Opt.*, vol. 53, no. 29, pp. 6670–6681, Oct. 2014, doi: 10.1364/AO.53.006670.

[35] A. Wilson and H. Hua, 'Design and demonstration of a vari-focal optical see-through head-mounted display using freeform Alvarez lenses', *Opt. Express*, vol. 27, no. 11, pp. 15627–15637, May 2019, doi: 10.1364/OE.27.015627.

[36] Yang Tong, Duan Yingzhe, Cheng Dewen, and Wang Yongtian, 'Freeform Imaging Optical System Design: Theories, Development, and Applications', *Acta Opt. Sin.*, vol. 41, no. 1, p. 0108001, 2021, doi: 10.3788/AOS202141.0108001.

[37] R. Augusteyn, 'Growth of the lens: In vitro observations', *Clin. Exp. Optom. J. Aust. Optom. Assoc.*, vol. 91, pp. 226–39, Jun. 2008, doi: 10.1111/j.1444-0938.2008.00255.x.

[38] D. J. Meister and S. W. Fisher, 'Progress in the spectacle correction of presbyopia. Part 2: Modern progressive lens technologies', *Clin. Exp. Optom.*, vol. 91, no. 3, pp. 251–264, May 2008, doi: 10.1111/j.1444-0938.2008.00246.x.

[39] Y. Wei, P. Zhai, X. Chen, and L. He, 'Study on Design and Diamond Turning of Optical Freeform Surface for Progressive Addition Lenses', *Math. Probl. Eng.*, vol. 2020, pp. 1–9, Feb. 2020, doi: 10.1155/2020/2850606.

[40] J. Alonso, J. A. Gómez-Pedrero, and J. A. Quiroga, *Modern Ophthalmic Optics*, 1st ed. Cambridge University Press, 2019. doi: 10.1017/9781316275474.

[41] B. Otero, J. M. Cela, E. Fontdecaba, and S. Eulalia, ‘Different Surface Models for Progressive Lenses and their Effect in Parallelization’, p. 6.

[42] S. Wu, G. Wang, G. Xia, Y. Sun, and M. Hu, ‘Design and resolution analysis of parabolic mirror spectrometer’, in *AOPC 2017: Optical Spectroscopy and Imaging*, SPIE, Oct. 2017, pp. 356–361. doi: 10.1117/12.2285329.

[43] D. Herriott, H. Kogelnik, and R. Kompfner, ‘Off-Axis Paths in Spherical Mirror Interferometers’, *Appl. Opt.*, vol. 3, no. 4, pp. 523–526, Apr. 1964, doi: 10.1364/AO.3.000523.

[44] Roulet, Melanie, et al. ‘Off-axis parabolas super polished under stress: the case of the Roman Space Telescope coronagraphic instrument mirrors.’ *Optics Express* 28.21 (2020): 30555-30569. Accessed: Dec. 11, 2024. [Online]. Available: https://opg.optica.org/oe/fulltext.cfm?uri=oe-28-21-30555&id=440151

[45] Chen, Lu, et al. ‘Construction method through multiple off-axis parabolic surfaces expansion and mixing to design an easy-aligned freeform spectrometer.’ *Optics Express* 27.18 (2019): 25994-26013. Accessed: Dec. 11, 2024. [Online]. Available: https://opg.optica.org/oe/fulltext.cfm?uri=oe-27-18-25994&id=417237

[46] D. Spiga *et al.*, ‘Optical simulations for the laboratory-based expanded and collimated x-ray beam facility BEaTriX’, in *Advances in Laboratory-based X-Ray Sources, Optics, and Applications VII*, SPIE, Oct. 2019, pp. 67–79. doi: 10.1117/12.2530066.

[47] V. I. Yurevich, V. A. Grimm, A. A. Afonyushkin, K. V. Yudin, and S. G. Gorny, ‘Optical design and performance of F-Theta lenses for high-power and high-precision applications’, in *Optical Systems Design 2015: Optical Design and Engineering VI*, SPIE, Sep. 2015, pp. 437–452. doi: 10.1117/12.2190777.

[48] T. Araki, T. Hirai, and T. Kyotani, ‘Development of F-Theta Lens for UV Lasers’. *SEI Tech Rev* 69 (2009): 59-65.

[49] W. Yuan, L.-H. Li, W.-B. Lee, and C.-Y. Chan, ‘Fabrication of Microlens Array and Its Application: A Review’, *Chin. J. Mech. Eng.*, vol. 31, no. 1, p. 16, Feb. 2018, doi: 10.1186/s10033-018-0204-y.

[50] M. Oikawa, K. Iga, T. Sanada, N. Yamamoto, and K. Nishizawa, ‘Array of Distributed-Index Planar Micro-Lenses Prepared from Ion Exchange Technique’, *Jpn. J. Appl. Phys.*, vol. 20, no. 4, p. L296, Apr. 1981, doi: 10.1143/JJAP.20.L296.

[51] N. F. Borrelli, D. L. Morse, R. H. Bellman, and W. L. Morgan, ‘Photolytic technique for producing microlenses in photosensitive glass’, *Appl. Opt.*, vol. 24, no. 16, pp. 2520–2525, Aug. 1985, doi: 10.1364/AO.24.002520.

[52] Z. D. Popovic, R. A. Sprague, and G. A. N. Connell, ‘Technique for monolithic fabrication of microlens arrays’, *Appl. Opt.*, vol. 27, no. 7, pp. 1281–1284, Apr. 1988, doi: 10.1364/AO.27.001281.

[53] M. Kubo and M. Hanabusa, ‘Fabrication of microlenses by laser chemical vapor deposition’, *Appl. Opt.*, vol. 29, no. 18, pp. 2755–2759, Jun. 1990, doi: 10.1364/AO.29.002755.

[54] D. M. Hartmann, O. Kibar, and S. C. Esener, 'Polymer microlens arrays fabricated using the hydrophobic effect', in *Optics in Computing 2000*, SPIE, May 2000, pp. 496–507. doi: 10.1117/12.386869.

[55] Y. Fu and B. K. A. Ngoi, 'Investigation of diffractive-refractive microlens array fabricated by focused ion beam technology', *Opt. Eng.*, vol. 40, no. 4, pp. 511–516, Apr. 2001, doi: 10.1117/1.1355257.

[56] N. S. Ong, Y. H. Koh, and Y. Q. Fu, 'Microlens array produced using hot embossing process', *Microelectron. Eng.*, vol. 60, no. 3, pp. 365–379, Apr. 2002, doi: 10.1016/S0167-9317(01)00695-5.

[57] P. Merz, H. J. Quenzer, H. Bernt, B. Wanger, and M. Zoberbier, 'A novel micromachining technology for structuring borosilicate glass substrates', in *TRANSDUCERS '03. 12th International Conference on Solid-State Sensors, Actuators and Microsystems. Digest of Technical Papers (Cat. No.03TH8664)*, Jun. 2003, pp. 258–261 vol.1. doi: 10.1109/SENSOR.2003.1215302.

[58] X. Zhang, F. Fang, L. Yu, L. Jiang, and Y. Guo, 'Slow slide servo turning of compound eye lens', *Opt. Eng.*, vol. 52, no. 2, p. 023401, Feb. 2013, doi: 10.1117/1.OE.52.2.023401.

[59] F. Z. Fang, X. D. Zhang, and X. T. Hu, 'Cylindrical coordinate machining of optical freeform surfaces', *Opt. Express*, vol. 16, no. 10, pp. 7323–7329, May 2008, doi: 10.1364/OE.16.007323.

[60] X. Liu, X. Zhang, F. Fang, Z. Zeng, H. Gao, and X. Hu, 'Influence of machining errors on form errors of microlens arrays in ultra-precision turning', *Int. J. Mach. Tools Manuf.*, vol. 96, pp. 80–93, Sep. 2015, doi: 10.1016/j.ijmachtools.2015.05.008.

[61] D. P. Yu, G. S. Hong, and Y. S. Wong, 'Profile error compensation in fast tool servo diamond turning of micro-structured surfaces', *Int. J. Mach. Tools Manuf.*, vol. 52, no. 1, pp. 13–23, Jan. 2012, doi: 10.1016/j.ijmachtools.2011.08.010.

[62] D. Floreano *et al.*, 'Miniature curved artificial compound eyes', *Proc. Natl. Acad. Sci.*, vol. 110, no. 23, pp. 9267–9272, Jun. 2013, doi: 10.1073/pnas.1219068110.

[63] M.-K. Park *et al.*, 'Design and Fabrication of Multi-Focusing Microlens Array with Different Numerical Apertures by using Thermal Reflow Method', *J. Opt. Soc. Korea*, vol. 18, no. 1, pp. 71–77, Feb. 2014.

[64] M. Levoy, R. Ng, A. Adams, M. Footer, and M. Horowitz, 'Light field microscopy', in *ACM SIGGRAPH 2006 Papers*, in SIGGRAPH '06. New York, NY, USA: Association for Computing Machinery, Jul. 2006, pp. 924–934. doi: 10.1145/1179352.1141976.

[65] A. Lasemi, D. Xue, and P. Gu, 'Recent development in CNC machining of freeform surfaces: A state-of-the-art review', *Comput.-Aided Des.*, vol. 42, no. 7, pp. 641–654, Jul. 2010, doi: 10.1016/j.cad.2010.04.002.

[66] N. Taniguchi, 'Current Status in, and Future Trends of, Ultraprecision Machining and Ultrafine Materials Processing', *CIRP Ann.*, vol. 32, no. 2, pp. 573–582, Jan. 1983, doi: 10.1016/S0007-8506(07)60185-1.

[67] N. Ikawa *et al.*, ‘Ultraprecision Metal Cutting — The Past, the Present and the Future’, *CIRP Ann.*, vol. 40, no. 2, pp. 587–594, Jan. 1991, doi: 10.1016/S0007-8506(07)61134-2.

[68] J. B. Bryan, ‘Design and construction of an ultraprecision 84 inch diamond turning machine’, *Precis. Eng.*, vol. 1, no. 1, pp. 13–17, Jan. 1979, doi: 10.1016/0141-6359(79)90071-0.

[69] Joe, K. U. R. A. G. A. N. O. ‘Generation of nc tool path for subdivision surface’ Proc. CAD/Graphics' 2001 (2001). Accessed: Dec. 11, 2024. [Online]. Available: https://cir.nii.ac.jp/crid/1571698600102987520

[70] Lee, Wing Bun, Suet To, and Chi Fai Cheung. *超精密自由曲面光学设计. 加工及测量技术*. 机械工业出版社, 2015. Accessed: Dec. 11, 2024.

[71] W. Jiang, W. Bao, Q. Tang, and H. Wang, ‘A variational-difference numerical method for designing progressive-addition lenses’, *Comput.-Aided Des.*, vol. 48, pp. 17–27, Mar. 2014, doi: 10.1016/j.cad.2013.10.011.

[72] Yang Tong, Duan Yingzhe, Cheng Dewen, and Wang Yongtian, ‘Freeform Imaging Optical System Design: Theories, Development, and Applications’, *Acta Opt. Sin.*, vol. 41, no. 1, p. 0108001, 2021, doi: 10.3788/AOS202141.0108001.

[73] O. Aves, ‘Improvements in and relating to multifocal lenses and the like, and the method of grinding same’, 1908

[74] VOLK, DAVID, and JOSEPH W. WEINBERG. ‘The Omnifocal Lens for Presbyopia’ *Archives of Ophthalmology* 68.6 (1962): 776-784. Accessed: Dec. 13, 2024. [Online]. Available: https://jamanetwork.com/journals/jamaophthalmology/article-abstract/627055

[75] D. J. Meister and S. W. Fisher, ‘Progress in the spectacle correction of presbyopia. Part 1: Design and development of progressive lenses’, *Clin. Exp. Optom.*, vol. 91, no. 3, pp. 240–250, May 2008, doi: 10.1111/j.1444-0938.2007.00245.x.

[76] J. T. Winthrop, ‘Progressive addition spectacle lens’, US4861153A, Aug. 29, 1989 Accessed: Dec. 13, 2024. [Online]. Available: https://patents.google.com/patent/US4861153A/en

[77] J. T. Winthrop and S. W. Smith, ‘Application of the Dirichlet Principle to the Design of Progressive-Addition Lenses’, in *Ophthalmic and Visual Optics (1991), paper FB3*, Optica Publishing Group, Feb. 1991, p. FB3. doi: 10.1364/OVO.1991.FB3.

[78] J. Loos, G. Greiner, and H.-P. Seidel, ‘A variational approach to progressive lens design’, *Comput.-Aided Des.*, vol. 30, no. 8, pp. 595–602, Jul. 1998, doi: 10.1016/S0010-4485(97)00102-4.

[79] J. Loos, Ph. Slusallek, and H.-P. Seidel, ‘Using Wavefront Tracing for the Visualization and Optimization of Progressive Lenses’, *Comput. Graph. Forum*, vol. 17, no. 3, pp. 255–265, 1998, doi: 10.1111/1467-8659.00272.

[80] M. Duncan, ‘Bézier Curves I’, in *Applied Geometry for Computer Graphics and CAD*, in

Springer Undergraduate Mathematics Series. , London: Springer London, 2005, pp. 135–160. doi: 10.1007/1-84628-109-1_6.

[81] L. Piegl and W. Tiller, *The NURBS Book*. Springer Science & Business Media, 1996.

[82] S. J. Zhang, S. To, S. J. Wang, and Z. W. Zhu, 'A review of surface roughness generation in ultra-precision machining', *Int. J. Mach. Tools Manuf.*, vol. 91, pp. 76–95, Apr. 2015, doi: 10.1016/j.ijmachtools.2015.02.001.

[83] T. Sata, 'Surface finish in metal cutting', *Ann. CIRP*, vol. 12, no. 4, pp. 190–197, 1964.

[84] S. To, C. F. Cheung, and W. B. Lee, 'Influence of material swelling on surface roughness in diamond turning of single crystals', *Mater. Sci. Technol.*, vol. 17, no. 1, pp. 102–108, Jan. 2001, doi: 10.1179/026708301101509025.

[85] M. C. Kong, W. B. Lee, C. F. Cheung, and S. To, 'A study of materials swelling and recovery in single-point diamond turning of ductile materials', *J. Mater. Process. Technol.*, vol. 180, no. 1, pp. 210–215, Dec. 2006, doi: 10.1016/j.jmatprotec.2006.06.006.

[86] W. B. Lee, S. To, and C. Y. Chan, 'Deformation band formation in metal cutting', *Scr. Mater.*, vol. 40, no. 4, pp. 439–443, Jan. 1999, doi: 10.1016/S1359-6462(98)00440-0.

[87] C. F. Cheung, K. C. Chan, S. To, and W. B. Lee, 'Effect of reinforcement in ultra-precision machining of Al6061/SiC metal matrix composites', *Scr. Mater.*, vol. 47, no. 2, pp. 77–82, Jul. 2002, doi: 10.1016/S1359-6462(02)00097-0.

[88] Simoneau, A., Elbestawi Ng, and M. A. Elbestawi. 'Surface defects during microcutting.' International Journal of Machine Tools and Manufacture 46.12-13 (2006): 1378-1387. Accessed: Dec. 13, 2024. [Online]. Available: https://www.sciencedirect.com/science/article/pii/S0890695505002725

[89] K. Liu and S. N. Melkote, 'Effect of plastic side flow on surface roughness in micro-turning process', *Int. J. Mach. Tools Manuf.*, vol. 46, no. 14, pp. 1778–1785, Nov. 2006, doi: 10.1016/j.ijmachtools.2005.11.014.

[90] S. J. Zhang, S. To, and H. T. Wang, 'A theoretical and experimental investigation into five-DOF dynamic characteristics of an aerostatic bearing spindle in ultra-precision diamond turning', *Int. J. Mach. Tools Manuf.*, vol. 71, pp. 1–10, Aug. 2013, doi: 10.1016/j.ijmachtools.2013.03.001.

[91] G. P. Specifications, 'Surface Texture: Areal—Part 2: Terms, Definitions and Surface Texture Parameters', *Int. Organ. Stand.*, pp. 25178–2, 2012.

[92] T. Whitted and B. Laboratories, 'An Improved Illumination Model for Shaded Display', vol. 23, no. 6, 1980.

[93] J. T. Kajiya, 'Ray tracing parametric patches', in *Proceedings of the 9th annual conference on Computer graphics and interactive techniques*, in SIGGRAPH '82. New York, NY, USA: Association for Computing Machinery, Jul. 1982, pp. 245–254. doi: 10.1145/800064.801287.

[94] Toth, Daniel L. "On ray tracing parametric surfaces." ACM SIGGRAPH Computer Graphics 19.3 (1985): 171-179.

[95] K. I. Joy and M. N. Bhetanabhotla, ‘Ray tracing parametric surface patches utilizing numerical techniques and ray coherence’, *ACM SIGGRAPH Comput. Graph.*, vol. 20, no. 4, pp. 279–285, Aug. 1986, doi: 10.1145/15886.15917.

[96] T. W. Sederberg and T. Nishita, ‘Curve intersection using Bézier clipping’, *Comput.-Aided Des.*, vol. 22, no. 9, pp. 538–549, Nov. 1990, doi: 10.1016/0010-4485(90)90039-F.

[97] W. Barth and W. Stürzlinger, ‘Efficient ray tracing for Bezier and B-spline surfaces’, *Comput. Graph.*, vol. 17, no. 4, pp. 423–430, Jul. 1993, doi: 10.1016/0097-8493(93)90031-4.

[98] A. Fournier and J. Buchanan, ‘Chebyshev Polynomials for Boxing and Intersections of Parametric Curves and Surfaces’, *Comput. Graph. Forum*, vol. 13, no. 3, pp. 127–142, 1994, doi: 10.1111/1467-8659.1330127.

[99] W. Martin, E. Cohen, R. Fish, and P. Shirley, ‘Practical ray tracing of trimmed NURBS surface’, *J. Graph. Tools*, vol. 5, Sep. 2000, doi: 10.1080/10867651.2000.10487519.

[100] K. P. Monroy Vazquez, C. Giardini, and E. Ceretti, ‘Cutting Force Modeling’, DE, 2018. doi: 10.1007/978-3-642-35950-7_6399-4.

[101] H. K. Toenshoff, ‘Cutting, Fundamentals’, in *CIRP Encyclopedia of Production Engineering*, L. Laperrière and G. Reinhart, Eds., Berlin, Heidelberg: Springer, 2014, pp. 345–357. doi: 10.1007/978-3-642-20617-7_6633.

[102] J. Liu, ‘Experimental Study And Modeling Of Mechanical Micro-machining Of Particle Reinforced Heterogeneous Materials’, *Electron. Theses Diss.*, Jan. 2012, [Online]. Available: https://stars.library.ucf.edu/etd/2498

[103] J. P. Davim, ‘Diamond tool performance in machining metal–matrix composites’, *J. Mater. Process. Technol.*, vol. 128, no. 1, pp. 100–105, Oct. 2002, doi: 10.1016/S0924-0136(02)00431-4.

[104] V. F. C. Sousa *et al.*, ‘Cutting Forces Assessment in CNC Machining Processes: A Critical Review’, *Sensors*, vol. 20, no. 16, Art. no. 16, Jan. 2020, doi: 10.3390/s20164536.

[105] A. G. Atkins, ‘Modelling metal cutting using modern ductile fracture mechanics: quantitative explanations for some longstanding problems’, *Int. J. Mech. Sci.*, vol. 45, no. 2, pp. 373–396, Feb. 2003, doi: 10.1016/S0020-7403(03)00040-7.

[106] A. Bauer, ‘Optical design with freeform surfaces, with applications in head-worn display design’, 2016, Accessed: Jan. 21, 2025. [Online]. Available: https://urresearch.rochester.edu/institutionalPublicationPublicView.action?institutionalItemId=31260&versionNumber=1

[107] A. Khaghani and K. Cheng, ‘Investigation on multi-body dynamics based approach to the toolpath generation for ultraprecision machining of freeform surfaces’, *Proc. Inst. Mech. Eng. Part B J. Eng. Manuf.*, vol. 234, no. 3, pp. 571–583, Feb. 2020, doi: 10.1177/0954405419863961.

[108] I. O. Aver’yanova, D. Yu. Bogomolov, and V. V. Poroshin, ‘ISO 25178 standard for three-dimensional parametric assessment of surface texture’, *Russ. Eng. Res.*, vol. 37, no. 6, pp.

513–516, Jun. 2017, doi: 10.3103/S1068798X17060053.

[109] A. Coulier, *Multiscale Modeling in Systems Biology: Methods and Perspectives*, vol. 2051. in Digital Comprehensive Summaries of Uppsala Dissertations from the Faculty of Science and Technology, vol. 2051. Acta Universitatis Upsaliensis, 2021. doi: 10.33063/diva-442412.

[110] J. Toussaint and K. Cheng, 'Web-based CBR (case-based reasoning) as a tool with the application to tooling selection', *Int. J. Adv. Manuf. Technol.*, vol. 29, no. 1, pp. 24–34, May 2006, doi: 10.1007/s00170-004-2501-0.

[111] J. Toussaint and K. Cheng, 'Design agility and manufacturing responsiveness on the Web', *Integr. Manuf. Syst.*, vol. 13, no. 5, pp. 328–339, Aug. 2002, doi: 10.1108/09576060210429784.

[112] M. P. Groover and G. Jayaprakash, *Automation, production systems, and computer-integrated manufacturing*, Fourth;Global; Harlow, Essex, England: Pearson, 2016. [Online]. Available: https://go.exlibris.link/nclTmZ3v

[113] K. Cheng and R. J. Bateman, 'e-Manufacturing: Characteristics, applications and potentials', *Prog. Nat. Sci.*, vol. 18, no. 11, pp. 1323–1328, Nov. 2008, doi: 10.1016/j.pnsc.2008.03.027.

[114] P. Li, K. Cheng, P. Jiang, and K. Katchasuwanmanee, 'Investigation on industrial dataspace for advanced machining workshops: enabling machining operations control with domain knowledge and application case studies', *J. Intell. Manuf.*, Aug. 2020, doi: 10.1007/s10845-020-01646-2.

[115] J. Alonso, J. A. Gómez-Pedrero, and J. A. Quiroga, *Modern Ophthalmic Optics*. Cambridge University Press, 2019.

[116] J. P. Rolland *et al.*, 'Freeform optics for imaging', *Optica*, vol. 8, no. 2, pp. 161–176, Feb. 2021, doi: 10.1364/OPTICA.413762.

[117] W.-Y. Hsu, Y.-L. Liu, Y.-C. Cheng, C.-H. Kuo, C.-C. Chen, and G.-D. Su, 'Design, fabrication, and metrology of ultra-precision optical freeform surface for progressive addition lens with B-spline description', *Int. J. Adv. Manuf. Technol.*, vol. 63, no. 1, pp. 225–233, Nov. 2012, doi: 10.1007/s00170-012-3901-1.

[118] C. F. Cheung, L. B. Kong, L. T. Ho, S. To, B. Wang, and K. T. Lai, 'An integrated approach for design, ultraprecision polishing, and measurement of freeform progressive lenses', in *6th International Symposium on Advanced Optical Manufacturing and Testing Technologies: Advanced Optical Manufacturing Technologies*, SPIE, Oct. 2012, pp. 88–94. doi: 10.1117/12.977832.

[119] N. Sultanova, S. Kasarova, and I. Nikolov, 'Dispersion Properties of Optical Polymers', *Acta Phys. Pol. A*, vol. 116, no. 4, pp. 585–587, Oct. 2009, doi: 10.12693/APhysPolA.116.585.

[120] Yip, Wai Sze, Suet To, and Hongting Zhou. "Current status, challenges and opportunities of sustainable ultra-precision manufacturing." Journal of Intelligent Manufacturing (2022): 1-13. Accessed: Jan. 21, 2025. [Online]. Available:

https://link.springer.com/article/10.1007/s10845-021-01782-3

[121] Gong, Zheng, et al. "A novel long-stroke fast tool servo system with counterbalance and its application to the ultra-precision machining of microstructured surfaces." Mechanical Systems and Signal Processing 173 (2022): 109063. Accessed: Sep. 21, 2024. [Online]. Available: https://www.sciencedirect.com/science/article/pii/S0888327022002357

[122] S. He *et al.*, 'Spiral tool path generation method in a NURBS parameter space for the ultra-precision diamond turning of freeform surfaces', *J. Manuf. Process.*, vol. 60, pp. 340–355, Dec. 2020, doi: 10.1016/j.jmapro.2020.10.073.

[123] Sawangsri, Worapong, and Kai Cheng. "An innovative approach to cutting force modelling in diamond turning and its correlation analysis with tool wear." Proceedings of the Institution of Mechanical Engineers, Part B: Journal of Engineering Manufacture 230.3 (2016): 405-415. Accessed: Jan. 21, 2025. [Online]. Available: https://www.researchgate.net/publication/280218326_An_innovative_approach_to_cutting_force_modelling_in_diamond_turning_and_its_correlation_analysis_with_tool_wear

[124] M. Mukaida and J. Yan, 'Ductile machining of single-crystal silicon for microlens arrays by ultraprecision diamond turning using a slow tool servo', *Int. J. Mach. Tools Manuf.*, vol. 115, pp. 2–14, Apr. 2017, doi: 10.1016/j.ijmachtools.2016.11.004.

[125] S. To, Z. Zhu, and H. Wang, 'Virtual spindle based tool servo diamond turning of discontinuously structured microoptics arrays', *CIRP Ann.*, vol. 65, no. 1, pp. 475–478, Jan. 2016, doi: 10.1016/j.cirp.2016.04.047.

[126] M. Yang *et al.*, 'Recent Development for Ultra-Precision Macro–Micro Dual-Drive System: A Review', *Machines*, vol. 11, no. 1, Art. no. 1, Jan. 2023, doi: 10.3390/machines11010096.

[127] Y.-L. Chen, Y. Cai, K. Tohyama, Y. Shimizu, S. Ito, and W. Gao, 'Auto-tracking single point diamond cutting on non-planar brittle material substrates by a high-rigidity force controlled fast tool servo', *Precis. Eng.*, vol. 49, pp. 253–261, Jul. 2017, doi: 10.1016/j.precisioneng.2017.02.014.

[128] Zhou, Xiaoqin, Rongqi Wang, and Qiang Liu. "Study on suppressing cutting force fluctuations based on c hip loads for turning optical freeform surfaces." The International Journal of Advanced Manufacturing Technology 90 (2017): 2037-2046. Accessed: Jan. 21, 2025. [Online]. Available: https://link.springer.com/article/10.1007/s00170-016-9487-2

[129] Z. Zhu, S. To, W.-L. Zhu, P. Huang, and X. Zhou, 'Cutting forces in fast-/slow tool servo diamond turning of micro-structured surfaces', *Int. J. Mach. Tools Manuf.*, vol. 136, pp. 62–75, Jan. 2019, doi: 10.1016/j.ijmachtools.2018.09.003.

[130] Bäumer, Stefan, ed. Handbook of plastic optics. John Wiley & Sons, 2011.

[131] Vu, Lien T., Chao-Chang A. Chen, and Chia-Wei Yu. "Optical design of soft multifocal contact lens with uniform optical power in center-distance zone with optimized NURBS." *Optics Express* 26.3 (2018): 3544-3556.

[132] Vu, Lien T., Chao-Chang A. Chen, and Patrick Joi-Tsang Shum. "Analysis on multifocal contact lens design based on optical power distribution with NURBS." *Applied Optics* 56.28 (2017): 7990-7997.

[133] Bennett, Edward S. "Contact lens correction of presbyopia." *Clinical and experimental optometry* 91.3 (2008): 265-278.

[134] Vu, Thi-Lien, Chao-Chang Chen, and Yu-Ting Qiu. "Progressive multifocal contact lens and producing method thereof." U.S. Patent No. 10,274,750. 30 Apr. 2019.

[135] Kirkpatrick, Scott, C. Daniel Gelatt Jr, and Mario P. Vecchi. "Optimization by simulated annealing." *science* 220.4598 (1983): 671-680.R

[136] Fuerter, Gerd M. "Spline surfaces as means for optical design." 1985 International Lens Design Conference. Vol. 554. SPIE, 1986.

[137] Hubeli, Andreas, and Markus Gross. "A survey of surface representations for geometric modeling." CS technical report 335 (2000).

[138] Iske, Armin, Ewald Quak, and Michael S. Floater, eds. *Tutorials on multiresolution in geometric modelling: summer school lecture notes*. Springer Science & Business Media, 2002.

[139] Prautzsch, Hartmut, Wolfgang Boehm, and Marco Paluszny. Bézier and B-spline techniques. Springer Science & Business Media, 2002.

[140] Kühnel, W., and B. Hunt. "Differential geometry: curves, surfaces, manifolds. edn." American Mathematical Society (2015).

[141] ÖGE, Tuba ÖZDEMİR. "AN OVERVIEW OF PROGRESSIVE ADDITION LENSES (PALS)." Research & Reviews in Science and Mathematics-II (2021): 1926.

[142] Ott, Peter. "Optic design of head-up displays with freeform surfaces specified by NURBS." Optical Design and Engineering III. Vol. 7100. SPIE, 2008.

[143] She, Alan, et al. "Large area metalenses: design, characterization, and mass manufacturing." *Optics express* 26.2 (2018): 1573-1585.

[144] Nguyen, Anh, and Bac Le. "3D point cloud segmentation: A survey." 2013 6th IEEE conference on robotics, automation and mechatronics (RAM). IEEE, 2013.

[145] Song, An Ping, et al. "MeshGraphNet: An effective 3D polygon mesh recognition With topology reconstruction." IEEE Access 8 (2020): 205181-205189.

[146] Luo, Yiming, Zhenxing Mi, and Wenbing Tao. "Deepdt: Learning geometry from delaunay triangulation for surface reconstruction." Proceedings of the AAAI Conference on Artificial Intelligence. Vol. 35. No. 3. 2021.

[147] Dianat N, Liu S, Cheng K, et al. "Development of the E-Portal for the Design of Freeform Varifocal Lenses Using Shiny/R Programming Combined with Additive Manufacturing". Machines, 2025, 13(4): 298.

[148] Chen D C. "Portable alignment device for an off-axis parabolic mirror optical axis

adjustment". International Journal of Precision Engineering and Manufacturing, 2012, 13: 33-37.

[149] Subbiah S, Melkote S N. "Evaluation of Atkins model of ductile machining including the material separation component". Journal of Materials Processing Technology, 2007, 182(1-3): 398-404.

Appendices

Appendix A: A list of publications arising from this doctoral research

(1) Liu S, Cheng K. Development of a web-based e-portal for freeform surfaced lenses design and manufacturing and its implementation perspectives[J]. Machines, 2024.

(2) Liu S, Cheng K. Investigation on the surface texture aspect ratio of freeform surfaced optics and its correlation with the optical performance[J]. Proc IMechE Part B: Journal of Engineering Manufacture, 2024.

(3) Liu S, Cheng K. Cutting forces in ultraprecision machining freeform optics: Analysis through virtual simulations and experiments[J]. Science Talks, 2024, 12.

(4) Liu S, Cheng K, Zhao L. Development of the personalized manufacturing system framework for freeform vari-focal lenses and its implementation and application perspectives[J]. International Journal of Mechatronics and Manufacturing Systems, 2023, 16(1): 1-21.

(5) Gou N, Liu S, Christopher D, et al. Development of the Digital Twin for the Ultraprecision Diamond Turning System and Its Application Perspectives[M]//Handbook of Digital Twins. CRC Press, 2024, 498-514.

(6) Liu S, Cheng K, Armstrong J. Cutting forces in ultraprecision machining freeform optics: Analysis through virtual simulations and experiments. The proceedings of the euspen 24th International Conference & Exhibition, Dublin, Ireland, June 2024.

(7) Liu S, Cheng K, Dianat N. Development of a Web-Based e-Portal for Freeform Surfaced Lens Design and Manufacturing and Its Implementation Perspectives[J]. Machines, 2025, 13(1): 59.

Appendix B: Shiny programming codes for developing the e-portal for integrated design, manufacturing and virtual assessment of freeform lenses

B1 – Industrial prescription of varifocal lens surface using for e-portal FSO surface design, modelling, manufacturing, assessment and analysis

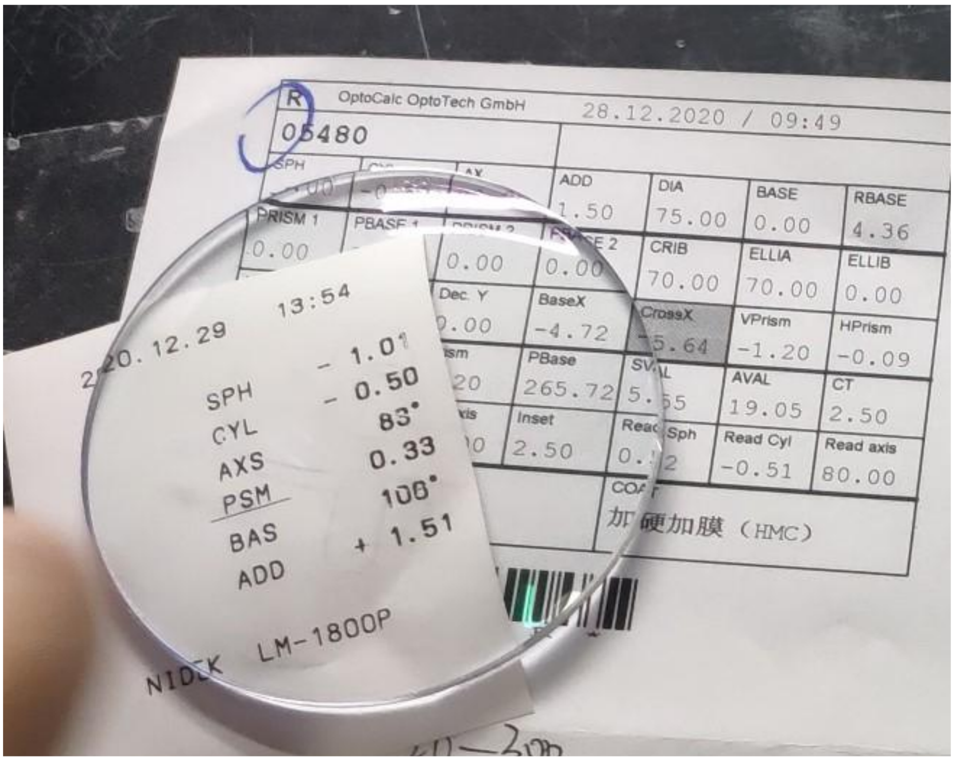

B2 – R-script programming package introduced for e-portal programming

```
library(shiny)

library(shinydashboard)

library(shinyWidgets)

library(readxl)

library(writexl)

library(rsconnect)

library(plotly)

library(pracma)

library(viridis)

library(tidyverse)
```

```r
library(janitor)

library(formattable)

library(golem)

library(esquisse)

# Read the material's data from the Excel file

material_data <- read_excel('material data base.xlsx')
```

B3 – R-script programming code for e-portal UI development

```r
#Define UI

ui <- dashboardPage(title="Freeform Optics Portal",

          dashboardHeader(title= div(

            img(src = "Brunel_University_logo.svg", height = 48, width=97,style = "margin-right: 0px;"),

            ""), titleWidth = 200),


          #Sidebar


          dashboardSidebar(sidebarMenu(

            id = "tabs",

            menuItem("Home", tabName = "welcome", icon = icon("hand")),

            hr(),

            menuItem("Eye Prescription", tabName = "prescription", icon = icon("pencil")),

            hr(),

            menuItem("Topography Assessment", tabName = "surface", icon = icon("hourglass-end")),

            hr(),
```

```
      menuItem("Optical Performance", tabName = "customization", icon = icon("glasses")),

      hr(),

      menuItem("About", tabName = "about", icon = icon("circle-question"))

    ),

    width = 200

    ),


    #change the style and size of title


    dashboardBody(

      tags$head(

        tags$title("Freeform Surface Design"),

        tags$style(

          HTML('

.background-page {

  background-image: url("back8.jpg");

  background-size: cover;

  background-repeat: no-repeat;

  background-attachment: fixed;

  min-height: 100vh;

  position: fixed;

  top: 0;

  left: 0;

  right: 0;
```

```
      bottom: 0;
      z-index: 0;
    }
    .shift-right {
margin-left: 6cm;
    }
        .main-header .logo {
      font-family: "Georgia", Times, "Times New Roman", serif;
      font-weight: bold;
      font-size: 20px;
    }
    .justify-text {
      text-align: justify;
    }
    .skin-blue .main-header .navbar {
      background-color: #444444;
    }
    .skin-blue .main-header .logo {
      background-color: #444444;
    }
    .skin-blue .main-sidebar {
      background-color: #444444;
    }
    .other-pages {
      background-image: url("back12.jpg");
```

```
  position: relative;
  z-index: 1;
  padding: 20px;
}
.btn-primary {
  background-color: #132a63;
  color: #ffffff;
  border-color: #132a63;
  margin-bottom: 15px;
}
.btn-primary:hover {
  background-color: #666666;
  border-color: #666666;
}
.box {
  background-color: #f0f0f0;
  border-radius: 10px;
  box-shadow: 2px 2px 10px rgba(0, 0, 0, 0.1);
}
.numeric-input, .select-input {
  margin-bottom: 15px;
}


.section-title {
```

```
    font-family: "Georgia", serif;
    font-size: 36px;
    font-weight: bold;
    color: #333333;
    text-align: center;
    padding-bottom: 10px;
    border-bottom: 2px solid #cccccc;
    margin-bottom: 20px;
  }

  .sub-section-title {
    font-family: "Arial", sans-serif;
    font-size: 24px;
    font-weight: bold;
    color: #555555;
    margin-top: 30px;
    margin-bottom: 10px;
    text-align: center;
    text-transform: uppercase;
    letter-spacing: 1px;
  }
'),
            tags$head(
             tags$style(HTML("
    .custom-button {
```

```css
  display: inline-block;
  padding: 10px 20px;
  font-size: 16px;
  font-weight: bold; /* Make text bold */
  color: #fff;
  background-color: #007bff; /* Blue background */
  border: none;
  border-radius: 25px; /* Oval shape */
  text-align: center;
  text-decoration: none;
  transition: background-color 0.3s ease;
}
.custom-button:hover {
  background-color: #0056b3; /* Darker blue on hover */
}
.centered-container {
  display: flex;
  flex-direction: column; /* Stack items vertically */
  justify-content: center;
  align-items: center;
  height: 100vh; /* Full height of viewport */
}
.button-container {
  display: flex;
  justify-content: center;
```

```
    width: 100%;
    margin-bottom: 15px;
   }
  "))
          ),



          HTML('.main-header .logo {
   font-family: "Georgia", Times, "Times New Roman", serif;
   font-weight: bold;
   font-size: 20px;}',

            ".justify-text {
  text-align: justify;
}",
            ".skin-blue .main-header .navbar {
  background-color: #000000;
}",
            ".skin-blue .main-header .logo {
  background-color: #000000;
}",
            ".skin-blue .main-sidebar {
    background-color: #000000;
   }",
```

```
                    "
      .other-pages {
        background-image: url('back12.jpg');
        position: relative;
        z-index: 1;
        padding: 20px;
      }"

                  ))),

                tags$head(
                  tags$script(HTML("
$(document).on('shiny:connected', function() {
  $('input[type=\"number\"]').each(function() {
    var input = $(this);
    var value = input.val();
    input.attr('placeholder', value);
    input.val('');
    input.on('focus', function() {
      if(input.val() == '') {
        input.attr('placeholder', '');
      }
    });
    input.on('blur', function() {
      if(input.val() == '') {
```

```
        input.attr('placeholder', value);
      }
    });
  });
});
"))
        ),


        tags$style(
          HTML(
            "

 .custom-panel {
   top: 80px;
   left: 250px;
   width: 600px;
   padding: 20px;
   background-color: rgba(255, 255, 255, 0.8);
   border-radius: 15px;
   box-shadow: 0 4px 8px rgba(0, 0, 0, 0.1);
   z-index: 1000;
 }
 "
          )
```

```
),
# Tab Contents

tabItems(
  # Welcome tab Content
  tabItem(tabName = "welcome",
      div(class = "background-page",
        absolutePanel(
          class = "custom-panel",
          h1("Corresponsive Portal for Freeform surface Design and Assessment",
             class = "section-title"),
          h3("Enter your optics prescription and check your lens surface topography and optical performance."),
          br(),
          br(),
          column(
            width = 12,
            class = "button-container",
            actionButton("go_prescription", "Get Start!", class = "custom-button")
          )
        )
      )),

  #About tab content
  tabItem(
```

```
tabName = "about",
div(
  class = "other-pages",
  fluidRow(
    column(
      width = 12,
      h1(
        "Welcome to visit Department of Mechanical & Aerospace Engineering,
Brunel University London, Uxbridge, UK",
        class = "section-title"
      )
    )
  ),
  fluidRow(
    column(
      width = 8,
      img(
        src = "About.png",
        alt = "University information",
        style = "width: 100%; height: auto;"
      )
    ),
    column(
      width = 4,
      fluidRow(
```

```
infoBox(
  title = tags$div(
    h2("Shangkuan Liu")
  ),
  value = tags$div(
    tags$p("Tel: 44-7384303268"),
    tags$p(
      tags$a(
        href = "mailto:shangkuan.liu@brunel.ac.uk",
        "Email: shangkuan.liu@brunel.ac.uk"
      )
    )
  ),
  icon = icon("user"),
  color = "light-blue",
  width = 12
),
infoBox(
  title = tags$div(
    h2("Professor Kai Cheng")
  ),
  value = tags$div(
    tags$p("Tel: 44-1895-267255"),
    tags$p(
      tags$a(
```

```
              href = "mailto:kai.cheng@brunel.ac.uk",
              "Email: kai.cheng@brunel.ac.uk"
             )
            )
          ),
          icon = icon("user"),
          color = "light-blue",
          width = 12
         )
        )
      )
     )
   )
),

# Prescription tab Content
tabItem(
  tabName = "prescription",
  div(
    class = "other-pages",
    h1("Customer Prescription", class = "section-title"),
    fluidRow(
      column(
        6,
        box(
```

```
title = "Left Eye",
width = NULL,
status = "primary",
solidHeader = TRUE,
collapsible = TRUE,
h4("SPH"),
numericInput("left_sph", label = NULL, value = 12.04819, min = -10, max = 100, step = 1),
h4("CYL"),
numericInput("left_cyl", label = NULL, value = 1, min = -10, max = 100, step = 1),
h4("AXIS"),
numericInput("left_axis", label = NULL, value = 4.01607, min = 1, max = 180, step = 1),
h4("ADD"),
numericInput("left_addition", label = NULL, value = 2, min = 0, max = 100, step = 1),
h4("Additional Parameters"),
h5("Corridor's Length"),
numericInput("left_h", label = NULL, value = 25.71, step = 1),
h5("Far-Zone Distance"),
numericInput("left_L", label = NULL, value = 10.65, step = 1),
selectInput("left_material", "Material Selection", choices = material_data[[1]])
)
),
column(
```

```
6,
box(
  title = "Right Eye",
  width = NULL,
  status = "primary",
  solidHeader = TRUE,
  collapsible = TRUE,
  h4("SPH"),
  numericInput("right_sph", label = NULL, value = 12.04819, min = -10, max = 10, step = 0.25),
  h4("CYL"),
  numericInput("right_cyl", label = NULL, value = 1, min = -10, max = 10, step = 0.25),
  h4("AXIS"),
  numericInput("right_axis", label = NULL, value = 4.01607, min = 1, max = 180, step = 1),
  h4("ADD"),
  numericInput("right_addition", label = NULL, value = 2, min = 0, max = 10, step = 0.25),
  h4("Additional Parameters"),
  h5("Corridor's Length"),
  numericInput("right_h", label = NULL, value = 25.71, step = 0.01),
  h5("Far-Zone Distance"),
  numericInput("right_L", label = NULL, value = 10.65, step = 0.01),
  selectInput("right_material", "Material Selection", choices = material_data[[1]])
)
```

```
      ),
      column(
        12,
        actionButton("submit", "Submit", icon = icon("paper-plane"), class = "btn-
primary"),
        textOutput("completion_message")
      ),
      column(
        12,
        box(
          title = "Material selection reference table",
          width = 12,
          status = "primary",
          solidHeader = TRUE,
          collapsible = TRUE,
          collapsed = TRUE,
          formattableOutput("table")
        )
      )
    )
  )
),

#surface plot tab content
```

```
tabItem(
  tabName = "surface",
  div(
    class = "other-pages",
    h1("2D Contour plot", class = "section-title"),
    fluidRow(
      box(
        title = "Left eye",
        width = 6,
        status = "primary",
        solidHeader = TRUE,
        collapsible = TRUE,
        collapsed = TRUE,
        plotOutput("PLSP", width = "100%", height = "400px"),
        plotOutput("PLRU", width = "100%", height = "400px")
      ),
      box(
        title = "Right eye",
        width = 6,
        status = "primary",
        solidHeader = TRUE,
        collapsible = TRUE,
        collapsed = TRUE,
        plotOutput("PRSP", width = "100%", height = "400px"),
        plotOutput("PRRU", width = "100%", height = "400px")
```

```
  )
),
h1("3D Model of the lens surface", class = "section-title"),
fluidRow(
  box(
    title = "Left Eye",
    width = 6,
    status = "primary",
    solidHeader = TRUE,
    collapsible = TRUE,
    plotlyOutput("plot3d_left")
  ),
  box(
    title = "Right Eye",
    width = 6,
    status = "primary",
    solidHeader = TRUE,
    collapsible = TRUE,
    plotlyOutput("plot3d_right")
  ),
  box(
    title = "Left Eye",
    width = 6,
    status = "primary",
    solidHeader = TRUE,
```

```
        collapsible = TRUE,
        plotlyOutput("plot3d_left_LSP")
      ),
      box(
        title = "Right Eye",
        width = 6,
        status = "primary",
        solidHeader = TRUE,
        collapsible = TRUE,
        plotlyOutput("plot3d_right_LSP")
      )
    )
  )
),

#customization tab content
tabItem(
  tabName = "customization",
  div(
    class = "other-pages",
    h1("Lens Ray tracing Assessment", class = "section-title"),
    fluidRow(
      column(
        12,
        box(
```

```
title = "2D Ray Tracing Result",

width = NULL,

status = "primary",

solidHeader = TRUE,

collapsible = TRUE,

collapsed = TRUE,

img(src = "Ray tracing plot.png", alt = "2D Ray Tracing Result", style =
"width: 100%; height: auto;")

)

),

column(

12,

box(

title = "3D Ray Tracing Result",

width = NULL,

status = "primary",

solidHeader = TRUE,

collapsible = TRUE,

collapsed = TRUE,

img(src = "Ray tracing plot2.png", alt = "2D Ray Tracing Result", style =
"width: 100%; height: auto;")

)

)

)

)

)
```

```
        ),
      )
)
```

B3 – Functional development with equation programming of the portal development

```
#Define Server
server <- function(input, output, session) {
  # Reactive expressions to get the refractive index 'n' based on selected material
  left_n <- reactive({
    material_data[material_data[[1]] == input$left_material, 2]
  })

  right_n <- reactive({
    material_data[material_data[[1]] == input$right_material, 2]
  })

  x <- reactiveVal(NULL)
  y <- reactiveVal(NULL)

  output$table <- renderFormattable({    formattable(material_data, align = c("l",rep("r", ncol(material_data))), list(
    `Indicator Name` = formatter("span", style = ~ style(color = "grey",font.weight = "bold")),
```

```
  area(col = 2:length(material_data)) ~ color_tile("#DeF7E9", "#71CA97")))})

observeEvent(input$go_prescription, {
  updateTabItems(session, "tabs","prescription")
})

observeEvent(input$submit, {

  # getting data from input for h,L,SPH,ADD for left and right

  Ln <- as.numeric(left_n())
  LL <-as.numeric(input$left_L)
  Lh <-as.numeric(input$left_h)
  LSph<-as.numeric(input$left_sph)
  LAdd<-as.numeric(input$left_addition)

  Rn <- as.numeric(right_n())
  RL <-as.numeric(input$right_L)
  Rh <-as.numeric(input$right_h)
  RSph<-as.numeric(input$right_sph)
  RAdd<-as.numeric(input$right_addition)
```

```
#Radius

RightRd <- as.numeric(((((Rn)-1)*1000)/(RSph)))          # right distant power

RightRn <- as.numeric((((Rn-1)*1000)/(RSph+RAdd)))        # right near power



print(paste("RightRd: ", RightRd))

print(paste("RightRn: ", RightRn))



LeftRd <-as.numeric((((Ln-1)*1000)/(LSph)))              # left distant power

LeftRn <-as.numeric((((Ln-1)*1000)/(LSph+LAdd)))         # left near power


# Define input parameters

x <- seq(-30, 30, by = 1)   # Range of x

y <- seq(-30, 30, by = 1)   # Range of y


# Calculate constants C5 to C8 for left eye


LC5 = 56 / (Lh^5)

LC6 = -140 / (Lh^6)

LC7 = 120 / (Lh^7)

LC8 = -35 / (Lh^8)
```

```
# Calculate the functions Lp, Lg, and Lu
calculate_functions <- function(x, y) {
  Lp <- x - (Lh / 2) + LL
  Lg <- (1 / 2) * (Lp + (y^2 + (Lh^2) / 4) / Lp)
  Lu <- (Lh / 2) - LL + Lg - sign(Lp) * sqrt(Lg^2 - (Lh^2) / 4)

  list(Lp = Lp, Lg = Lg, Lu = Lu)
}

#calculate LPL

calculate_LPL <- function(Lu) {
  LPL <- (1 / LeftRd) + ((1 / LeftRn - 1 / LeftRd) *
                         (LC5 * (Lu + LL)^5 +
                           LC6 * (Lu + LL)^6 +
                           LC7 * (Lu + LL)^7 +
                           LC8 * (Lu + LL)^8))
  LPL
}

# Calculate the function LRU

calculate_LRU <- function(LPL) {
  LRU <- 1 / LPL
```

```
  LRU
}

calculate_LSP<- function(LRU){
  Lpower<-((Ln-1)*1000)/LRU
  Lpower #mean surface power
}



# Initialize matrices to store calculation results

Lp_matrix <- matrix(NA, nrow = length(x), ncol = length(y))
Lg_matrix <- matrix(NA, nrow = length(x), ncol = length(y))
Lu_matrix <- matrix(NA, nrow = length(x), ncol = length(y))
LPL_matrix <- matrix(NA, nrow = length(x), ncol = length(y))
LRU_matrix <- matrix(NA, nrow = length(x), ncol = length(y))
LSP_matrix <- matrix(NA, nrow = length(x), ncol = length(y))
sin_theta_left_matrix <- matrix(NA, nrow = length(x), ncol = length(y))
theta_left_matrix <- matrix(NA, nrow = length(x), ncol = length(y))
a_left_matrix <- matrix(NA, nrow = length(x), ncol = length(y))
b_left_matrix <- matrix(NA, nrow = length(x), ncol = length(y))
z_left_matrix <- matrix(NA, nrow = length(x), ncol = length(y))

# Calculate Lp, Lg, Lu, Lsum, LPL, and LRU for all x and y
for (i in seq_along(x)) {
```

```
  for (j in seq_along(y)) {
    functions_result <- calculate_functions(x[i], y[j])

    Lp_matrix[i, j] <- functions_result$Lp
    Lg_matrix[i, j] <- functions_result$Lg
    Lu_matrix[i, j] <- functions_result$Lu

    LPL_value <- calculate_LPL(functions_result$Lu)
    LPL_matrix[i, j] <- LPL_value

    LRU_value <- calculate_LRU(LPL_value)
    LRU_matrix[i, j] <- LRU_value

    LSP_value <- calculate_LSP(LRU_value)
    LSP_matrix[i, j] <- LSP_value
  }
}

# Calculate all Sin_theta, theta, and a
for (m in seq_along(x)) {
  for (n in seq_along(y)) {

    sin_theta_left <- integrate(calculate_LPL,0,Lu_matrix[m,n])
    theta_left <- asin(sin_theta_left$value)
    a_left <- Lu_matrix[m, n]-LRU_matrix[m, n]*sin_theta_left$value
```

```
    sin_theta_left_matrix[m, n] <- sin_theta_left$value
    theta_left_matrix[m,n] <- theta_left
    a_left_matrix[m, n] <- a_left
  }
}

tan_theta_left_matrix <- sin_theta_left_matrix/cos(theta_left_matrix)
b_left_matrix <- LRU_matrix*cos(theta_left_matrix)+Lu_matrix*tan_theta_left_matrix
z_left_matrix <- b_left_matrix - sqrt(LRU_matrix^2-(x-a_left_matrix^2)-y^2)


# Flatten the matrices into vectors
x_vec_left <- rep(x, each = length(y))
y_vec_left <- rep(y, times = length(x))
z_vec_left <- as.vector(z_left_matrix)  # Flatten the z matrix into a vector

# Combine into a data frame
surface_data_left <- data.frame(x = x_vec_left, y = y_vec_left, z = z_vec_left)

#Export to Excel
write_xlsx(surface_data_left, "surface_data_left_excel.xlsx")
# write.csv(surface_data_left, "surface_data_left_csv.csv", row.names = FALSE)
# 3D surface plot for left eye
```

```
output$plot3d_left <- renderPlotly({

  plot_ly(x = x,y = y,z = z_left_matrix,
      type = "surface",
      colorscale = 'Jet') %>%

    layout(
     title=list(
      text="3D Surface Plot - Left Eye",
      font = list(
       family = "Times New Roman",
       size = 20,
       color = "black"
      )
     ),
     scene = list(
      xaxis = list(title = "X (mm)",titlefont = list(size = 12), tickfont = list(size = 12),range = c(-35, 35),showgrid = TRUE,showline = TRUE,zeroline = TRUE),
      yaxis = list(title = "Y (mm)",titlefont = list(size = 12), tickfont = list(size = 12),range = c(-35, 35),showgrid = TRUE,showline = TRUE,zeroline = TRUE),
      zaxis = list(title = "Z (mm)",titlefont = list(size = 12), tickfont = list(size = 12),showgrid = TRUE,showline = TRUE,zeroline = TRUE)
     ),
     margin = list(
      l = 20,  # Left margin
```

```
      r = 20,  # Right margin
      b = 20,  # Bottom margin
      t = 50   # Top margin, extra space for the title
    ))
})



# 3D Surface Plot for Left Eye based on Mean Surface Power

output$plot3d_left_LSP <- renderPlotly({
  plot_ly(x = x,y = y,z = LSP_matrix,
        type = "surface",
        colorscale = 'Jet') %>%

    layout(
     title=list(
      text="Surface Plot based on Mean Surface Power - Left Eye",
      font = list(
        family = "Times New Roman",
        size = 20,
        color = "black"
      )
     ),
     scene = list(
```

```
      xaxis = list(title = "X (mm)",titlefont = list(size = 12), tickfont = list(size = 12),range = c(-35, 35),showgrid = TRUE,showline = TRUE,zeroline = TRUE),

      yaxis = list(title = "Y (mm)",titlefont = list(size = 12), tickfont = list(size = 12),range = c(-35, 35),showgrid = TRUE,showline = TRUE,zeroline = TRUE),

      zaxis = list(title = "Z (mm)",titlefont = list(size = 12), tickfont = list(size = 12),showgrid = TRUE,showline = TRUE,zeroline = TRUE)

    ),

    margin = list(

      l = 20,  # Left margin

      r = 20,  # Right margin

      b = 20,  # Bottom margin

      t = 50   # Top margin, extra space for the title

    ))

 })



 # Calculate constants C5 to C8 for right eye


 RC5 = 56 / (Rh^5)

 RC6 = -140 / (Rh^6)

 RC7 = 120 / (Rh^7)

 RC8 = -35 / (Rh^8)



 # Calculate the functions Lp, Lg, and Lu
```

```
calculate_functions <- function(x, y) {
  Rp <- x - (Rh / 2) + RL
  Rg <- (1 / 2) * (Rp + (y^2 + (Rh^2) / 4) / Rp)
  Ru <- (Rh / 2) - RL + Rg - sign(Rp) * sqrt(Rg^2 - (Rh^2) / 4)

  list(Rp = Rp, Rg = Rg, Ru = Ru)
}

#calculate RPL

calculate_RPL <- function(Ru) {
  RPL <- (1 / RightRd) + ((1 / RightRn - 1 / RightRd) *
                          (RC5 * (Ru + RL)^5 +
                             RC6 * (Ru + RL)^6 +
                             RC7 * (Ru + RL)^7 +
                             RC8 * (Ru + RL)^8))
  RPL
}

# Calculate the function RRU

calculate_RRU <- function(RPL) {
  RRU <- 1 / RPL
  RRU
}
```

```
calculate_RSP<- function(RRU){
  Rpower<-((Rn-1)*1000)/RRU
  Rpower #mean surface power
}


# Initialize matrices to store calculation results

Rp_matrix <- matrix(NA, nrow = length(x), ncol = length(y))
Rg_matrix <- matrix(NA, nrow = length(x), ncol = length(y))
Ru_matrix <- matrix(NA, nrow = length(x), ncol = length(y))
RPL_matrix <- matrix(NA, nrow = length(x), ncol = length(y))
RRU_matrix <- matrix(NA, nrow = length(x), ncol = length(y))
RSP_matrix <- matrix(NA, nrow = length(x), ncol = length(y))
sin_theta_right_matrix <- matrix(NA, nrow = length(x), ncol = length(y))
theta_right_matrix <- matrix(NA, nrow = length(x), ncol = length(y))
a_right_matrix <- matrix(NA, nrow = length(x), ncol = length(y))
b_right_matrix <- matrix(NA, nrow = length(x), ncol = length(y))
z_right_matrix <- matrix(NA, nrow = length(x), ncol = length(y))

# Calculate Rp, Rg, Ru, RPL, and RRU for all x and y

for (i in seq_along(x)) {
  for (j in seq_along(y)) {
```

```
    functions_result <- calculate_functions(x[i], y[j])

    Rp_matrix[i, j] <- functions_result$Rp
    Rg_matrix[i, j] <- functions_result$Rg
    Ru_matrix[i, j] <- functions_result$Ru

    RPL_value <- calculate_RPL(functions_result$Ru)
    RPL_matrix[i, j] <- RPL_value

    RRU_value <- calculate_RRU(RPL_value)
    RRU_matrix[i, j] <- RRU_value

    RSP_value <- calculate_RSP(RRU_value)
    RSP_matrix[i, j] <- RSP_value
  }
}

# Calculate all Sin_theta, theta, and a
for (m in seq_along(x)) {
  for (n in seq_along(y)) {

    sin_theta_right <- integrate(calculate_RPL,0,Ru_matrix[m,n])
    theta_right <- asin(sin_theta_right$value)
    a_right <- Ru_matrix[m, n]-RRU_matrix[m, n]*sin_theta_right$value
```

```
      sin_theta_right_matrix[m, n] <- sin_theta_right$value

      theta_right_matrix[m,n] <- theta_right

      a_right_matrix[m, n] <- a_right

    }

  }


  tan_theta_right_matrix <- sin_theta_right_matrix/cos(theta_right_matrix)

  b_right_matrix                                                              <-
RRU_matrix*cos(theta_right_matrix)+Ru_matrix*tan_theta_right_matrix

  z_right_matrix <- b_right_matrix - sqrt(RRU_matrix^2-(x-a_right_matrix^2)-y^2)



  # 3D surface plot for right eye


  output$plot3d_right <- renderPlotly({


    plot_ly(x = x,y = y,z = z_right_matrix,

        type = "surface",

        colorscale = 'Jet') %>%


      layout(

        title=list(

          text="3D Surface Plot - Right Eye",

          font = list(
```

```
          family = "Times New Roman",
          size = 20,
          color = "black"
        )
      ),
      scene = list(
        xaxis = list(title = "X (mm)",titlefont = list(size = 12), tickfont = list(size = 12),range = c(-35, 35),showgrid = TRUE,showline = TRUE,zeroline = TRUE),
        yaxis = list(title = "Y (mm)",titlefont = list(size = 12), tickfont = list(size = 12),range = c(-35, 35),showgrid = TRUE,showline = TRUE,zeroline = TRUE),
        zaxis = list(title = "Z (mm)",titlefont = list(size = 12), tickfont = list(size = 12),showgrid = TRUE,showline = TRUE,zeroline = TRUE)
      ),
      margin = list(
        l = 20,  # Left margin
        r = 20,  # Right margin
        b = 20,  # Bottom margin
        t = 50   # Top margin, extra space for the title
      ))
  })



  # 3D Surface Plot for Right Eye based on Mean Surface Power


  output$plot3d_right_LSP <- renderPlotly({
```

```
plot_ly(x = x,y = y,z = RSP_matrix,
        type = "surface",
        colorscale = 'Jet') %>%

  layout(
    title=list(
      text="Surface Plot based on Mean Surface Power - Right Eye",
      font = list(
        family = "Times New Roman",
        size = 20,
        color = "black"
      )
    ),
    scene = list(
      xaxis = list(title = "X (mm)",titlefont = list(size = 12), tickfont = list(size = 12),range = c(-35, 35),showgrid = TRUE,showline = TRUE,zeroline = TRUE),
      yaxis = list(title = "Y (mm)",titlefont = list(size = 12), tickfont = list(size = 12),range = c(-35, 35),showgrid = TRUE,showline = TRUE,zeroline = TRUE),
      zaxis = list(title = "Z (mm)",titlefont = list(size = 12), tickfont = list(size = 12),showgrid = TRUE,showline = TRUE,zeroline = TRUE)
    ),
    margin = list(
      l = 20,  # Left margin
      r = 20,  # Right margin
      b = 20,  # Bottom margin
      t = 50   # Top margin, extra space for the title
```

```
    ))
  })

  #2D plots for both left and right
  custom_colors <- colorRampPalette(c("yellow","dodgerblue2", "purple"))(10)

  output$PLRU <- renderPlot({
    x <- seq(-30, 30, by = 1)
    y <- seq(-30, 30, by = 1)
    z_left_matrix_rotated <- t(z_left_matrix)
    image(y, x, z_left_matrix_rotated, col =NA, main = "2D point cloud Contour Plot (mm) - Left Eye", xlab = "X (mm)", ylab = "Y (mm)")
    contour(y, x, z_left_matrix_rotated, add = TRUE, col = custom_colors, labcex = 1)  # Add contour lines for better visualization
    lines(y = c(-LL, -LL + Lh), x = c(0, 0))
    points(y = -LL, x = 0)
    points(y = -LL + Lh, x = 0)
    #Add dashed ellipse
    theta <- seq(0, 2 * pi, length = 100)  # Parametric angle
    a <- 30  # Semi-major axis
    b <- 20  # Semi-minor axis
    x_ellipse <- a * cos(theta)  # X-coordinates of the ellipse
    y_ellipse <- b * sin(theta)  # Y-coordinates of the ellipse
```

```
    lines(0.9*x_ellipse, y_ellipse, col = "red", lty = 2, lwd = 2)  # lty = 2 for dashed line

  }

  )


  output$PLSP<-renderPlot({

    x <- seq(-30, 30, by = 1)

    y <- seq(-30, 30, by = 1)

    LSP_matrix_rotated <- t(LSP_matrix)

    image(y, x, LSP_matrix_rotated, col = NA, main = "Mean Surface Power Contour Plot (D)
- Left Eye", xlab = "X (mm)", ylab = "Y (mm)")

    contour(y, x, LSP_matrix_rotated, add = TRUE, col = custom_colors, labcex = 1)  # Add
contour lines for better visualization

    lines(y = c(-RL, -RL + Rh), x = c(0, 0))

    points(y = -RL, x = 0)

    points(y = -RL + Rh, x = 0)

    #Add dashed ellipse

    theta <- seq(0, 2 * pi, length = 100)  # Parametric angle

    a <- 30  # Semi-major axis

    b <- 20  # Semi-minor axis

    x_ellipse <- a * cos(theta)  # X-coordinates of the ellipse

    y_ellipse <- b * sin(theta)  # Y-coordinates of the ellipse


    lines(0.9*x_ellipse, y_ellipse, col = "red", lty = 2, lwd = 2)  # lty = 2 for dashed line

  })


  output$PRRU <- renderPlot({
```

```
x <- seq(-30, 30, by = 1)

y <- seq(-30, 30, by = 1)

z_right_matrix_rotated <- t(z_right_matrix)

image(y, x, z_right_matrix_rotated, col =NA, main = "2D point cloud Contour Plot (mm) - Right Eye", xlab = "X (mm)", ylab = "Y (mm)")

contour(y, x, z_right_matrix_rotated, add = TRUE, col = custom_colors, labcex = 1)  # Add contour lines for better visualization

lines(y = c(-RL, -RL + Rh), x = c(0, 0))

points(y = -RL, x = 0)

points(y = -RL + Rh, x = 0)

#Add dashed ellipse

theta <- seq(0, 2 * pi, length = 100)  # Parametric angle

a <- 30  # Semi-major axis

b <- 20  # Semi-minor axis

x_ellipse <- a * cos(theta)  # X-coordinates of the ellipse

y_ellipse <- b * sin(theta)  # Y-coordinates of the ellipse


lines(0.9*x_ellipse, y_ellipse, col = "red", lty = 2, lwd = 2)  # lty = 2 for dashed line

})


output$PRSP<-renderPlot({

x <- seq(-30, 30, by = 1)

y <- seq(-30, 30, by = 1)

RSP_matrix_rotated <- t(RSP_matrix)

image(y, x, RSP_matrix_rotated, col = NA, main = "Mean Surface Power Contour Plot (D) - Right Eye", xlab = "X (mm)", ylab = "Y (mm)")
```

```
    contour(y, x, RSP_matrix_rotated, add = TRUE, col = custom_colors, labcex = 1)  # Add
contour lines for better visualization

    lines(y = c(-RL, -RL + Rh), x = c(0, 0))

    points(y = -RL, x = 0)

    points(y = -RL + Rh, x = 0)

    #Add dashed ellipse

    theta <- seq(0, 2 * pi, length = 100)  # Parametric angle

    a <- 30  # Semi-major axis

    b <- 20  # Semi-minor axis

    x_ellipse <- a * cos(theta)  # X-coordinates of the ellipse

    y_ellipse <- b * sin(theta)  # Y-coordinates of the ellipse

    lines(0.9*x_ellipse, y_ellipse, col = "red", lty = 2, lwd = 2)  # lty = 2 for dashed line

   })

   showModal(modalDialog(

    "Calculation completed!",

    easyClose = TRUE,

    footer = NULL

   ))

  })

 }

shinyApp(ui, server)
```

Appendix C: MATLAB programming codes for cutting forces modelling and simulation in ultraprecision diamond turning of freeform surfaces

C1 – Toolpath date generation setup for dynamic cutting force modelling and analysis

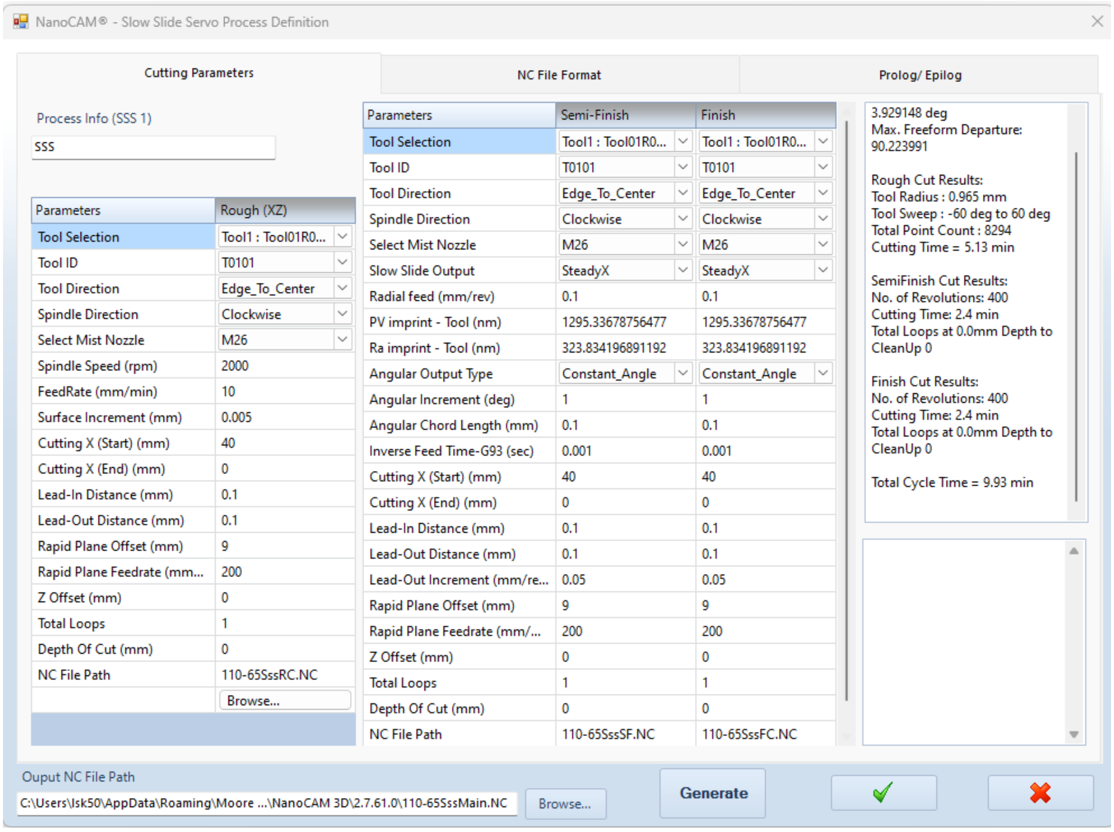

C2 – Generated toolpath G-code file for FSO cutting force simulation and analysis

(NanoCAM Version : 2.7 Build : 61)

(CREATED : Friday 2024/1/26 8:48:45)

(OPERATOR : NanoCAM Operator)

(SCRIPT: SSS Post.mpyx - MODIFIED: 2019/5/15)

(Aperture Type : Circle)

(Outer Aperture : 37.532881 mm)

(Surface Type : StepIges3D)

(FilePath : E:\OneDrive - Brunel University London\Dynamic cutting force\11 离抛文件\D35-F150-X6.stp)

(Tool : Diamond Tool [Tool ID - 1])

(Name : SPD 1)

(Tool Info :)

(Diamond Type : Conical)

(Tool Radius : 0.07 mm)

(Included Angle : 60 deg)

(Rake Angle : 0 deg)

(Horizontal Orientation : 0 deg)

(Vertical Orientation : 0 deg)

(Primary Clearance : 15 deg)

(Spindle and Tool Direction : Clockwise - Edge_To_Center)

(X Start and X End : 18.76644 mm, 0.0 mm)

(LeadIn and LeadOut Distance, Increment : 0.1 mm, 0.1 mm, 0.05 mm / rev)

(SSS Output Type : SteadyX)

(Radial Feed per Revolution : 0.024)

(Angular Chord Length : 0.003 [Constant_Arc])

(Inverse-Time Feed, Block Time : 0.001)

(============== SECTION - COMMANDS ==================)

G94 (FEED RATE IN mm/min & NFTS OFF)

#550 = #550 - #552 (CURRENT CUTTING OFFSET)

G52 Z[#550] (SET COORDINATE SYSTEM OFFSET)

G01 X20.00000000 F200 (PARKING POSITION - X)

Z10.00000000 (PARKING POSITION - Z)

(LEAD IN BLOCKS)

```
G01 C0.0 X18.88800000 F200
Z0.76261466
Y0.0                                    ( SET Y AXIS TO 0 )
M[#507]                                     ( MIST ON )
G01 G93 F0.0010
C0.0091 X18.88799939 Z0.76260937
C0.018201 X18.88799879 Z0.76260960
C0.027301 X18.88799818 Z0.76261491
C0.036401 X18.88799757 Z0.76262486
C0.045502 X18.88799697 Z0.76263902
C0.054602 X18.88799636 Z0.76265695
C0.063702 X18.88799575 Z0.76267821
C0.072803 X18.88799515 Z0.76270238
C0.081903 X18.88799454 Z0.76272900
C0.091003 X18.88799393 Z0.76275766
…
C352.421324 X0.00000000 Z0.09894741
C353.421324 X0.00000000 Z0.09908630
C354.421324 X0.00000000 Z0.09922519
C355.421324 X0.00000000 Z0.09936408
C356.421324 X0.00000000 Z0.09950297
C357.421324 X0.00000000 Z0.09964186
C358.421324 X0.00000000 Z0.09978075
C359.421324 X0.00000000 Z0.09991964
C0.0
```

```
G04 P1            ( DWELL )
M29               ( MIST OFF )
( PARKING POSITION )
G94 G01 Z10.00000000 F200
X20.00000000
( =============== SECTION - FOOTER =================== )
```

C3 – MATLAB programming for cutting force modelling and simulation

```
opts = delimitedTextImportOptions("NumVariables", 3);
%opts.DataLines = [53, 20651324]; % original data
opts.DataLines = [53, 206513]; % selected data for testing
opts.Delimiter = " ";

opts.VariableNames = ["C", "X", "Z"];
opts.VariableTypes = ["string", "string", "string"];

opts.MissingRule = "omitrow";
opts.ExtraColumnsRule = "ignore";
opts.EmptyLineRule = "read";
opts.ConsecutiveDelimitersRule = "join";
opts.LeadingDelimitersRule = "ignore";

% Variation proporities
opts = setvaropts(opts, ["C", "X"], "WhitespaceRule", "preserve");
opts = setvaropts(opts, ["C", "X", "Z"], "EmptyFieldRule", "auto");
```

```
% Imput data
Toolpath = readtable("UntitledSssFC.NC", opts); % UntitledSssFC.NC D35-F150-JC-0.003.nc


%% Clear temp var
clear opts

%% Data Manipulating
% Translate table to array;
tp1 = table2array(Toolpath);

% Delate the error line;
% First round
% Detect
k = find(tp1 == "(");
% Delate
tp1(k, :) = [];

% Second round
% Detect
Ztp = contains(tp1, "Y");
Ztp = string(Ztp);
[m, n] = find(Ztp == 'true');
% Delate
```

```
tp1(m, :) = [];


Ccol = tp1(:,1);
Xcol = tp1(:,2);
Zcol = tp1(:,3);

Csc = split(Ccol, 'C');
Xsc = split(Xcol, 'X');
Zsc = split(Zcol, 'Z');

% Change string data to double;
Cdb = str2double(Csc);
Xdb = str2double(Xsc);
Zdb = str2double(Zsc);
Z = Zdb(:,2);


function h_kl = calculate_h_kl(theta_i, alpha0, alpha1, r, z2, h0, theta_a, theta_b, theta_c)

  if theta_i >= theta_a && theta_i < theta_b
    h_kl = (1 - cos(alpha0 + theta_i + alpha1)) / cos(alpha0 + theta_i);
  elseif theta_i >= theta_b && theta_i < theta_c
    h_kl = (r * cos(alpha0) - (z2 - h0) ./ cos(theta_i) .* cos(alpha0));
  else
```

```
        error('theta_i not in range');
    end
end

f = 0.002;

% Nose radius of the cutter (mm)
r_tool = 0.988;

% Spindle rotation speed (r/s), cutting velocity related
Vr_range = 100;
Vr = 3000 + (rand(size(Z)) - 0.5) * Vr_range;
%Vr = 3000;

% Shear yield stress (Mpa)
tau = 55.2;

% Coefficient of friction
u = 0.583;

% Objective surface diameter (mm)
D = 78;

% Tool rake angle (mm)
a = 0;
```

```
% Tool tips height h0 (mm)
h0 = 0;

% The friction angle;
beta = atan(u);

vectorLength = length(Z);
z1_vector = zeros(1, vectorLength-1);
z2_vector = zeros(1, vectorLength-1);
xa_vector = zeros(1, vectorLength-1);
za_vector = zeros(1, vectorLength-1);
xb_vector = zeros(1, vectorLength-1);
zb_vector = zeros(1, vectorLength-1);
xc_vector = zeros(1, vectorLength-1);
zc_vector = zeros(1, vectorLength-1);
theta_a_vector = zeros(1, vectorLength-1);
theta_b_vector = zeros(1, vectorLength-1);
theta_c_vector = zeros(1, vectorLength-1);
alpha0_vector = zeros(1, vectorLength-1);
alpha1_vector = zeros(1, vectorLength-1);
theta_i_vector = zeros(1, vectorLength-1);
DoC_vector = zeros(1, vectorLength-1);

for i = 1:(vectorLength - 1)
```

```
z1 = Z(i);
z2 = Z(i + 1);

alpha0 = atan((z1-z2)./f);
d = sqrt(f.^2 + (z1 - z2).^2);
xa = -1/2.*f - sqrt(r_tool.^2 - (d./2).^2).*sin(alpha0);
za = 1/2.*(z1 + z2) - sqrt(r_tool.^2 - (d./2).^2).*cos(alpha0);
xb = sqrt(r_tool.^2 - (z1 - h0).^2) - f;
zb = h0;
xc = sqrt(r_tool.^2 - (z2 - h0).^2);
zc = h0;

theta_a = asin(xa./r_tool);
theta_b = atan(xb./(z2-h0));
theta_c = asin(xc./r_tool);

theta_i = pi/4 - beta/2;
alpha1 = asin(d./r_tool.*cos(alpha0+theta_i));
h_kl = calculate_h_kl(theta_i, alpha0, alpha1, r_tool, z2, h0, theta_a, theta_b, theta_c);

z1_vector(i) = z1;
z2_vector(i) = z2;
xa_vector(i) = xa;
za_vector(i) = za;
xb_vector(i) = xb;
```

```
    zb_vector(i) = zb;

    xc_vector(i) = xc;

    zc_vector(i) = zc;

    theta_a_vector(i) = rad2deg(theta_a);

    theta_b_vector(i) = rad2deg(theta_b);

    theta_c_vector(i) = rad2deg(theta_c);

    theta_i_vector(i) = rad2deg(theta_c);

    alpha0_vector(i) = rad2deg(alpha0);

    alpha1_vector(i) = rad2deg(alpha1);

    DoC_vector(i) = h_kl;


end


% ---------------------


t0 = 1;

t = DoC_vector;

% t = 0.003; % (mm) is the uncut chip thickness;


Vr = 3000;

% (r/s) Spindle rotation speed, cutting velocity related


Vc = (pi.* D.* Vr)/6000;

% Cutting speed in rotational cutting motion;
```

```
w = 2.*sqrt(r_tool.^2-(r_tool-t).^2);
% w - width of the orthogonal cut;

beta = atan(u);
% the friction angle;

%phi = 1;
% phi = theta_a_vector;
 phi = pi/4 - beta/2;
% the orientation of the shear plane;

gamma = cot(phi) + tan(phi);
% The shear strain along the shear plane;

R = 869.6263565464086;
% (Mpa/m) The plane stain fracture toughness of aluminum; 27.5Mpa/m=
% 869.6263565464086 Mpa/mm

Q = (1-(sin(beta).*sin(phi)./cos(beta).*cos(phi)));
% ----------------------
fc = ((tau.*w.*gamma)./Q).*t + (R.*w)./Q;

figure
plot(Xdb(1:206459,2), fc, 'DisplayName','fc');
xlabel('X Axis')
```

```
ylabel('Cutting force / N')
ax=gca;
ax.FontSize = 30;
xlim("auto")
ylim("auto")
grid on
legend("Cutting force (whole process)")
lgd = legend;
lgd.FontSize = 30;

figure();
plot(Xdb(30645:51290,2), fc(30645:51290), 'DisplayName','fc');
xlabel('X Axis')
ylabel('Cutting force / N')
ax=gca;
ax.FontSize = 30;
xlim("auto")
ylim("auto")
grid on
legend("Cutting force (Part view)")
lgd = legend;
lgd.FontSize = 30;

figure();
plot(Xdb(1:206459,2), theta_i_vector, 'DisplayName','theta_i');
```

```
xlabel('X Axis')
ylabel('Shear angle / Degree')
ax=gca;
ax.FontSize = 30;
xlim("auto")
ylim("auto")
grid on
legend("Shear Angle (whole process)")
lgd = legend;
lgd.FontSize = 30;
hold on



figure();
plot(Xdb(30645:51290,2), theta_i_vector(30645:51290), 'DisplayName','fc');
xlabel('X Axis')
ylabel('Shear angle / Degree')
ax=gca;
ax.FontSize = 30;
xlim("auto")
ylim("auto")
grid on
legend("Shear Angle (part view)")
lgd = legend;
lgd.FontSize = 30;
```

```
figure();
plot(Xdb(30645:51290,2), DoC_vector(30645:51290), 'DisplayName','DoC_vector');
xlabel('X Axis')
ylabel('DoC')
ax=gca;
ax.FontSize = 30;
xlim("auto")
ylim("auto")
grid on
legend("Depth of Cutting (part view)")
lgd = legend;
lgd.FontSize = 30;
figure();
plot(Xdb(30645:51290,2), DoC_vector(30645:51290), 'DisplayName','Q');
xlabel('X Axis')
ylabel('Q')
ax=gca;
ax.FontSize = 30;
xlim("auto")
ylim("auto")
grid on
legend("Q")
lgd = legend;
lgd.FontSize = 30;
```

Appendix D: COMSOL programming codes for Ray tracing simulation and analysis of freeform surfaced optics

D1 – Global Definitions of ray tracing simulation

GLOBAL SETTINGS

Name	Parabolic mirror ray tracing simulation
Version	COMSOL Multiphysics 6.0 (Build: 318)

USED PRODUCTS

CAD Import Module
COMSOL Multiphysics
Ray Optics Module

COMPUTER INFORMATION

CPU	Intel64 Family 6 Model 183 Stepping 1, 32 cores
Operating system	Windows 10

D2 – Component construction for the simulation

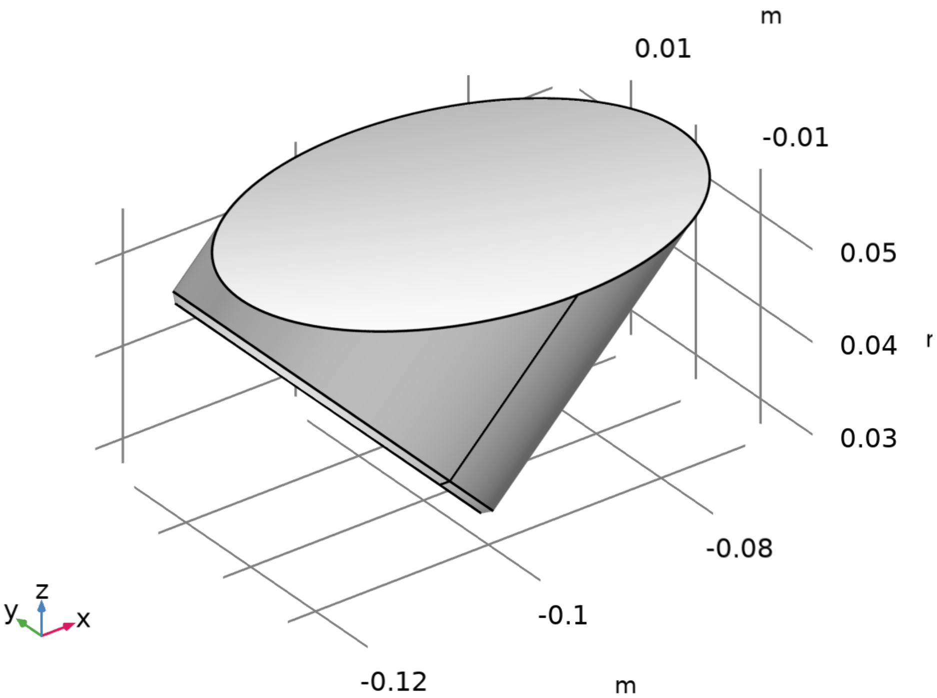

UNITS

Length unit	m
Angular unit	deg

D3 – Material selection: Cu (Copper) (Werner et al. 2009: DFT calculations; n,k 0.01759-2.480 um)

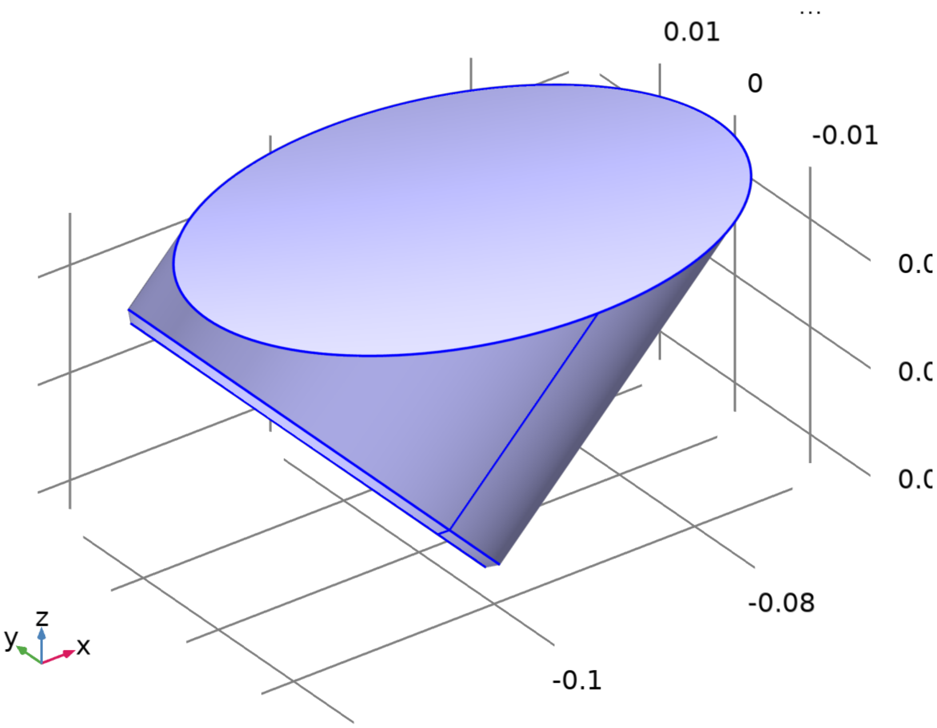

D4 – Geometrical optics model for the simulation

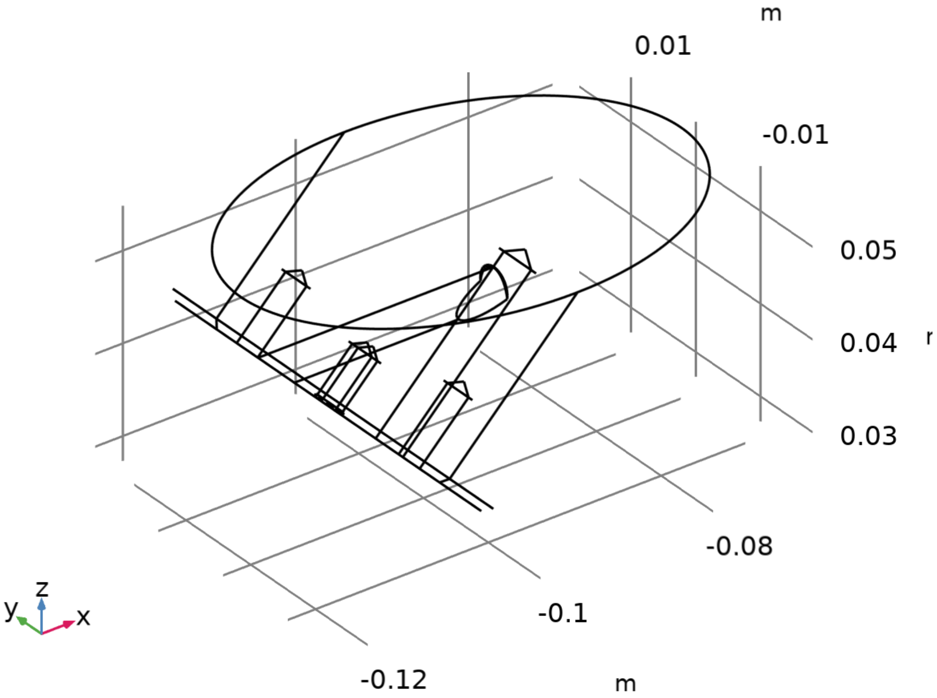

D5 – Mesh reconstruction of the model

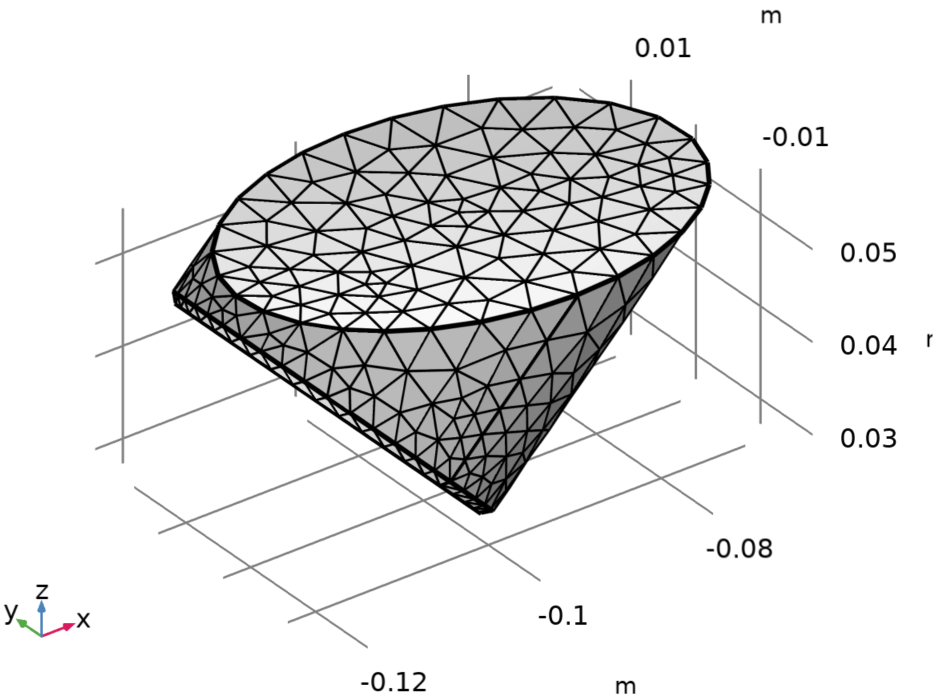

D6 – Simulation setup

Computation information

Computation time	1 s

Ray Tracing information

Description	Value
Include geometric nonlinearity	Off

Description	Value
Output times	{0, 0.01, 0.02, 0.03, 0.04, 0.05, 0.06, 0.07, 0.08, 0.09, 0.1, 0.11, 0.12, 0.13, 0.14, 0.15, 0.16, 0.17, 0.18, 0.19, 0.2, 0.21, 0.22, 0.23, 0.24, 0.25, 0.26, 0.27, 0.28, 0.29, 0.3, 0.31, 0.32, 0.33, 0.34, 0.35000000000000003, 0.36, 0.37, 0.38, 0.39, 0.4, 0.41000000000000003, 0.42, 0.43, 0.44, 0.45, 0.46, 0.47000000000000003, 0.48, 0.49, 0.5, 0.51, 0.52, 0.53, 0.54, 0.55, 0.56, 0.5700000000000001, 0.58, 0.59, 0.6, 0.61, 0.62, 0.63, 0.64, 0.65, 0.66, 0.67, 0.68, 0.6900000000000001, 0.7000000000000001, 0.71, 0.72, 0.73, 0.74, 0.75, 0.76, 0.77, 0.78, 0.79, 0.8, 0.81, 0.8200000000000001, 0.8300000000000001, 0.84, 0.85, 0.86, 0.87, 0.88, 0.89, 0.9, 0.91, 0.92, 0.93, 0.9400000000000001, 0.9500000000000001, 0.96, 0.97, 0.98, 0.99, 1}

Physics interface	Discretization
Geometrical Optics (gop)	physics

Geometry	Mesh
Geometry 1 (geom1)	mesh1

D7 – Results output

Position data of interact point

x	y	Value
0.088176	-2.1593E-5	0.0000
0.066247	-0.0036460	0.0000
0.027704	0.0063076	0.0000
-1.0780E-18	0.015000	0.0000
0.010607	0.010607	0.0000
0.069017	-5.6415E-4	0.0000

0.068176	-2.1593E-5	0.0000
0.057315	0.0037425	0.0000
0.068595	-2.9110E-4	4.9903E-4
0.058168	0.0035894	0.0041960
0.0096418	-0.011491	0.015000

Ray Trajectories result plot

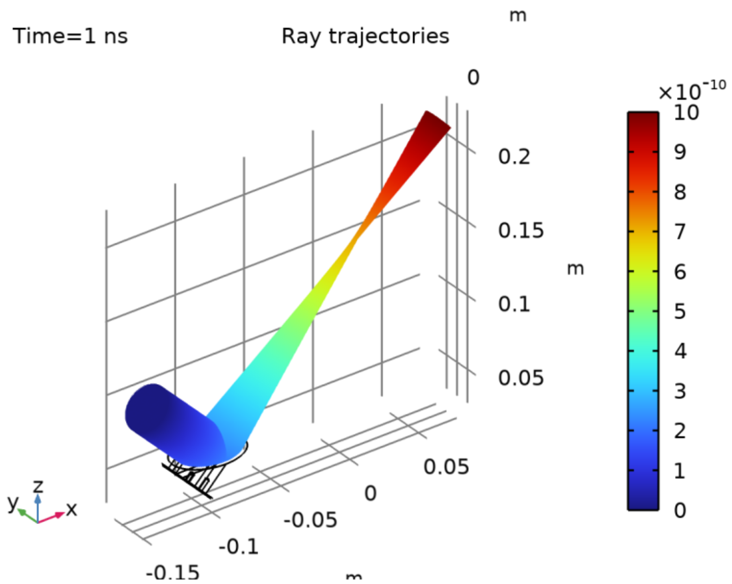

2D spot diagrams